



TECHNICAL REPORT AMR-PS-04-05

# **ANALYTIC MODELING AND EXPERIMENTAL VALIDATION OF INTUMESCENT BEHAVIOR OF CHARRING HEATSHIELD MATERIALS**

**Gerald Wayne Russell**

**Propulsion and Structures Directorate  
Aviation and Missile Research, Development, and Engineering Center**

**January 2004**

*Approved for public release; distribution is unlimited.*

### **DESTRUCTION NOTICE**

**FOR CLASSIFIED DOCUMENTS, FOLLOW THE PROCEDURES IN DoD 5200.22-M, INDUSTRIAL SECURITY MANUAL, SECTION II-19 OR DoD 5200.1-R, INFORMATION SECURITY PROGRAM REGULATION, CHAPTER IX. FOR UNCLASSIFIED, LIMITED DOCUMENTS, DESTROY BY ANY METHOD THAT WILL PREVENT DISCLOSURE OF CONTENTS OR RECONSTRUCTION OF THE DOCUMENT.**

### **DISCLAIMER**

**THE FINDINGS IN THIS REPORT ARE NOT TO BE CONSTRUED AS AN OFFICIAL DEPARTMENT OF THE ARMY POSITION UNLESS SO DESIGNATED BY OTHER AUTHORIZED DOCUMENTS.**

### **TRADE NAMES**

**USE OF TRADE NAMES OR MANUFACTURERS IN THIS REPORT DOES NOT CONSTITUTE AN OFFICIAL ENDORSEMENT OR APPROVAL OF THE USE OF SUCH COMMERCIAL HARDWARE OR SOFTWARE.**

<b>REPORT DOCUMENTATION PAGE</b>			Form Approved OMB No. 074-0188	
Public reporting burden for this collection of information is estimated to average 1 hour per response, including the time for reviewing instructions, searching existing data sources, gathering and maintaining the data needed, and completing and reviewing this collection of information. Send comments regarding this burden estimate or any other aspect of this collection of information, including suggestions for reducing this burden to Washington Headquarters Services, Directorate for Information Operations and Reports, 1215 Jefferson Davis Highway, Suite 1204, Arlington, VA 22202-4302, and to the Office of Management and Budget, Paperwork Reduction Project (0704-0188), Washington, DC 20503				
<b>1. AGENCY USE ONLY</b>		<b>2. REPORT DATE</b> January 2004	<b>3. REPORT TYPE AND DATES COVERED</b> Final	
<b>4. TITLE AND SUBTITLE</b> Analytic Modeling and Experimental Validation of Intumescent Behavior of Charring Heatshield Materials			<b>5. FUNDING NUMBERS</b>	
<b>6. AUTHOR(S)</b> Gerald Wayne Russell				
<b>7. PERFORMING ORGANIZATION NAME(S) AND ADDRESS(ES)</b> Commander, U. S. Army Aviation and Missile Command ATTN: AMSRD-AMR-PS-PI Redstone Arsenal, AL 35898			<b>8. PERFORMING ORGANIZATION REPORT NUMBER</b>  TR-AMR-PS-04-05	
<b>9. SPONSORING / MONITORING AGENCY NAME(S) AND ADDRESS(ES)</b>			<b>10. SPONSORING / MONITORING AGENCY REPORT NUMBER</b>	
<b>11. SUPPLEMENTARY NOTES</b>				
<b>12a. DISTRIBUTION / AVAILABILITY STATEMENT</b> Approved for public release; distribution is unlimited.			<b>12b. DISTRIBUTION CODE</b>  A	
<b>13. ABSTRACT (Maximum 200 Words)</b> Intumescent heatshield materials have been shown to provide significant thermal protection for missile system environments. The design and use of these materials requires the analytic understanding of a considerable level of thermodynamic phenomena occurring on the surface, as well as in-depth. These phenomena can include in-depth thermochemical decomposition, pyrolysis gas generation and mass transfer, thermophysical property change, thermochemical and mechanical ablation, intumescence or conduction path growth, and boundary layer modification due to pyrolysis gas injection or surface reactions. Existing numerical design codes do not specifically address the thermodynamic effects of intumescent behavior.  Continued on Page ii.				
<b>14. SUBJECT TERMS</b> Heatshield, thermodynamic phenomena, intumescent behavior, Charring Material thermal response and Ablation (CMA)			<b>15. NUMBER OF PAGES</b> 145	
			<b>16. PRICE CODE</b>	
<b>17. SECURITY CLASSIFICATION OF REPORT</b> UNCLASSIFIED	<b>18. SECURITY CLASSIFICATION OF THIS PAGE</b> UNCLASSIFIED	<b>19. SECURITY CLASSIFICATION OF ABSTRACT</b> UNCLASSIFIED	<b>20. LIMITATION OF ABSTRACT</b> SAR	

## **ABSTRACT (CONT)**

The purpose of this research was to significantly enhance the current state-of-the-art for modeling thermochemically decomposing heatshield materials through the addition of intumescent behavior effects to the Charring Material Thermal Response and Ablation Program (CMA). Additional efforts were devoted to the design of experiments to specifically quantify the intumescence phenomena. The intumescent material properties were primarily developed utilizing the low-shear thermal testing performed at the Wright-Patterson Laser Hardened Materials Evaluation Laboratory. Transient radiography of in-depth thermochemical decomposition and intumescence, as well as embedded thermocouples, were utilized quantifying properties of the various reacting regions within the material. The resulting intumescence model as applied and validated for a low-shear hypersonic high altitude environment generation at the National Aeronautics and Space Administration (NASA) Marshall Space Flight Center (MSFC) Hot Gas Test. The validated analytic model was then applied to the high shear convective heating environments generated at the Holloman High Speed Test Track at Holloman Air Force Base. This test environment provided an evaluation of the analytic model applicability for high shear environments.

The results of this research clearly show that through the use of a variety of aerothermal test environments, embedded thermocouples, transient radiography, and collection of detailed ablation measurements, the in-depth thermodynamic behavior of intumescent heatshield materials can be accurately modeled and used for any variety of aerodynamic boundary conditions. These results further provide an indication of mechanical shear sensitivity along with justification for future enhancement through development and implementation of erosion effects modeling.

## TABLE OF CONTENTS

	<u>Page</u>
<b>I. INTRODUCTION .....</b>	<b>1</b>
<b>A. Background .....</b>	<b>1</b>
<b>B. Objective .....</b>	<b>2</b>
<b>C. Approach .....</b>	<b>2</b>
<b>D. Expected Results .....</b>	<b>3</b>
<b>II. DISCUSSION OF THEORY .....</b>	<b>4</b>
<b>A. Thermodynamic Phenomena Overview .....</b>	<b>4</b>
<b>B. Theoretical Model of Phenomena.....</b>	<b>7</b>
<b>C. Convective and Radiative Heat Transfer .....</b>	<b>13</b>
<b>III. DISCUSSION OF NUMERICAL MODELS.....</b>	<b>19</b>
<b>A. Numerical Modeling Process .....</b>	<b>19</b>
<b>B. Thermochemical Decomposition Model .....</b>	<b>20</b>
<b>C. Simplified Heat of Ablation Model .....</b>	<b>32</b>
<b>IV. DISCUSSION OF EXPERIMENTS.....</b>	<b>34</b>
<b>A. Overview.....</b>	<b>34</b>
<b>B. Laser Thermal Testing .....</b>	<b>34</b>
<b>C. NASA Hot Gas Test Facility Aerothermal Testing .....</b>	<b>41</b>
<b>D. Aerothermal Sled Testing .....</b>	<b>50</b>
<b>E. Material Description .....</b>	<b>60</b>
<b>V. COMPARISON OF EXPERIMENTAL AND COMPUTATIONAL .....</b>	<b>66</b>
<b>A. Intumescence Model Validation .....</b>	<b>66</b>
<b>B. High Shear Application .....</b>	<b>78</b>
<b>VI. SUMMARY, CONCLUSIONS, AND RECOMMENDATIONS FOR FUTURE RESEARCH .....</b>	<b>82</b>
<b>REFERENCES .....</b>	<b>85</b>
<b>BIBLIOGRAPHY.....</b>	<b>91</b>

## TABLE OF CONTENTS (CONT)

<b>APPENDIX A: DERIVATIONS OF IN-DEPTH ENERGY AND THERMOCHEMICAL DECOMPOSITION NUMERICAL MODEL .....</b>	<b>A-1</b>
<b>APPENDIX B: EXAMPLE CMA INPUT DECK.....</b>	<b>B-1</b>
<b>APPENDIX C: EXAMPLE CMA OUTPUT DECK.....</b>	<b>C-1</b>
<b>APPENDIX D: EXAMPLE SWELL MODEL OUTPUT DECK.....</b>	<b>D-1</b>

## LIST OF ILLUSTRATIONS

	<u>Page</u>
1. Schematic of Models for Thermochemically Decomposing Heatshields .....	2
2. Schematic Description of Thermochemical Decomposition Phenomena .....	4
3. Model Development Process .....	20
4. Surface Boundary Condition Schematic .....	23
5. LHMEL Test Facility .....	35
6. Assembled Sample Configuration .....	36
7. Thermocouple Plug Configuration .....	37
8. Test 1, 22 Btu/ft <sup>2</sup> -sec Laser Heating Thermal Response .....	39
9. Test 2, 66 Btu/ft <sup>2</sup> -sec Laser Heating Thermocouple Response .....	39
10. Post-Test Material Response .....	40
11. Sectioned View of Material Sample Post-Test .....	40
12. NASA Marshall Space Flight Center Hot Gas Aerothermal Test Facility .....	42
13. Test Panel Configuration .....	43
14. HGTF Thermocouple Instrumentation .....	43
15. HGTF Thin Skin Calibration Panel.....	44
16. Mach 6 Test Thermal Boundary Conditions .....	45
17. Mach 8 Test Thermal Boundary Conditions .....	45
18. Cold Wall Shear for Mach 6 and Mach 8 Test Conditions.....	46
19. Calibration of Analytic Model for Mach 6 Test.....	46
20. Calibration of Analytic Model for Mach 8 Test.....	47
21. Thermal Response for Mach 6 Test .....	48
22. Sectioned View of In-depth Decomposition.....	49
23. Sled Test Hardware Configuration.....	52

## LIST OF ILLUSTRATIONS (CONT)

24.	Sled Test Sample Configuration.....	52
25.	Material Orientation .....	53
26.	Sled Vehicle Configuration .....	53
27.	Sled Test Samples .....	53
28.	Sled Velocity and Recovery Temperature History .....	54
29.	Sled Test Cold Wall Heat Transfer Coefficient .....	55
30.	Sled Test Cold Wall Heating Environment.....	55
31.	Sled Test Local Pressure .....	56
32.	Sled Test Cold Wall Shear .....	57
33.	Sled Vehicle During Peak Velocity.....	58
34.	Sled Test Samples After Test.....	58
35.	Pre- and Post-Photo of Sled Sample .....	59
36.	Measured Thermal Properties .....	61
37.	Intumescent Material Thermal Conductivity .....	61
38.	Intumescent Material Specific Heat.....	62
39.	Thermogravimetric Analysis at 50°C/Minute.....	64
40.	DSC Data .....	65
41.	Intumescence Model Functions .....	69
42.	Intumescence Model Validation Tests Heating Rates .....	69
43.	Laser Thermal Testing 0.05-inch Thermocouple Heating Rate.....	70
44.	Intumescence Behavior Predictions Versus Data .....	71
45.	Test 1, Overall Thermocouple Response Predictions Versus Data.....	72
46.	Test 1, In-depth Thermocouple Response Predictions Versus Data.....	73



## LIST OF ILLUSTRATIONS (CONCL)

47.	Test 2, Overall Thermocouple Response Predictions Versus Data.....	74
48.	Test 2, In-depth Thermocouple Response Predictions Versus Data.....	74
49.	Test 3, Overall Thermocouple Response Predictions Versus Data.....	76
50.	Test 3, In-depth Thermocouple Response Predictions Versus Data.....	77
51.	Test 3, Previous and New Model Prediction Comparisons.....	77
52.	Sled Test In-depth Heating Rate Predictions.....	78
53.	Sled Test In-depth Thermal Response Predictions .....	79
54.	Sled Test Char State Gradient and In-depth Density Predictions.....	79
55.	Intumescence and In-depth Decomposition History Predictions .....	81
56.	Sled Test Predicted Thermal Response Predictions.....	81

## LIST OF TABLES

	<b><u>Page</u></b>
<b>1. Pre- and Post-Test Measurements .....</b>	<b>41</b>
<b>2. Ablation Measurements for Mach 6 Test .....</b>	<b>49</b>
<b>3. Measured Ablation Depths .....</b>	<b>59</b>
<b>4. Organic Elemental Composition .....</b>	<b>62</b>
<b>5. Inorganic Elemental Composition .....</b>	<b>63</b>
<b>6. Mass Loss Comparison of Predictions and Measurements .....</b>	<b>75</b>

## I. INTRODUCTION

### A. Background

During the past several years, a significant level of research and development has been applied to optimization of missile systems for performance enhancement. One of the primary methods of enhancing performance is to reduce weight, thereby increasing velocity and range. To accomplish the weight reduction requirement, composite technology has been increasingly utilized in missile airframe design. While these composite structures afford a significant weight reduction, they are typically limited in operating temperature. As a result, a thermal protection system is required and must be designed in an optimal manner to maintain the weight reduction achieved through the use of the composite airframe. At present, there are essentially three methods of predicting thermal protection requirements: (1) the Simplified Heat Of Ablation (SHOA) approach [1] requires significant levels of testing at the thermal environment of interest for each material and is generally considered a conservative approximation; (2) the sublimation approach [2], while more complex, only models the mass loss and latent heat removal due to surface material temperature rise and is still limited in its application to decomposing heatshield materials; (3) the surface thermochemistry and thermochemical decomposition approach [3] is significantly more complex, attempting to model the thermodynamic phenomena occurring throughout the material and boundary layer. The third approach is a more rigorous mathematical treatment allowing for the identification of sensitivities to the various phenomena and provides a means of optimizing heatshield requirements for given geometries and aerothermal environments. While this approach adds significantly to the analytic capability of modeling heatshield thermodynamic behavior, it still requires a level of empiricism due to its current inability to model intumescence (swell or expansion) and mechanical shear. Recent empirical studies [4] have led to the identification of some intumescent heatshield materials having significantly higher thermal performance than many of the non-decomposing and ablating materials commonly used. The phenomenon of intumescence increases conduction path length, thereby reducing in-depth thermal penetration and increases insulative performance. Figure 1 provides a schematic of the non-intumescent model compared to the new intumescent model. This figure shows the various regions within the heatshield undergoing decomposition. The char region is assumed to be fully decomposed. As can be seen for the non-intumescent model, the conduction path is fixed, whereas the new intumescent model accounts for the effects of conduction path growth. This report provides an in-depth study to further enhance the complex modeling capability through the addition of a more rigorous mathematical treatment of the intumescent behavior of thermochemically decomposing materials.

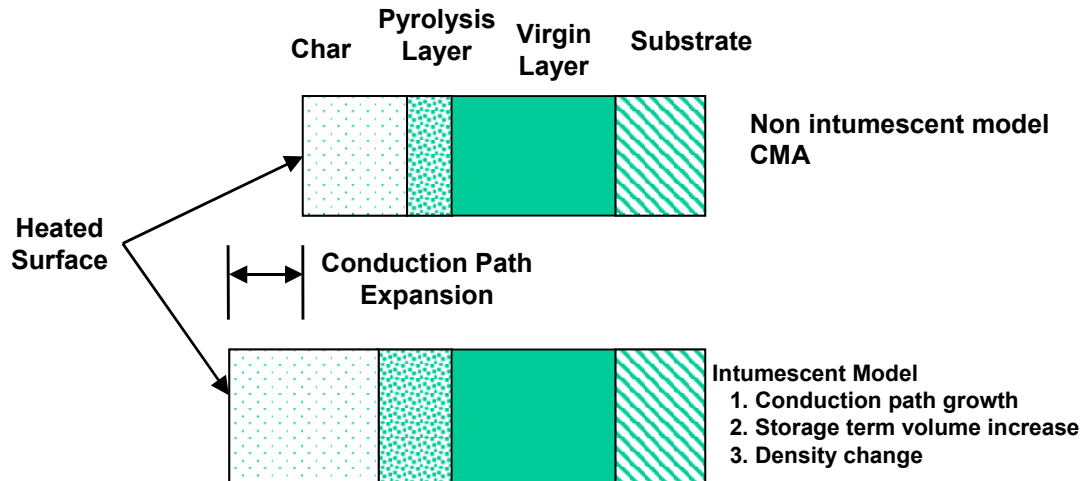


Figure 1. Schematic of Models for Thermochemically Decomposing Heatshields

## B. Objective

The objective of this research is to further reduce the level of empiricism through the development and experimental validation of mathematical relationships for intumescence and incorporate these relationships into the Charring Material Thermal Response and Ablation (CMA) Code [5] providing a means of more accurately predicting heatshield requirements and enhancing system level optimization. These additions to the existing model will provide the potential capability of developing heatshield material thermodynamic models applicable over a wide range of aerothermal environments, and optimize the level of experimental validation required for flight system design.

## C. Approach

The approach for accomplishing the research objectives initiated with the development of mathematical expressions for intumescence. These expressions were then incorporated into the existing CMA in a one-dimensional finite difference approach. Experimental data was collected through the use of a high heat flux test facility while minimizing aerodynamic shear effects. This allowed for a rigorous study of intumescence behavior and in-depth thermal response decoupled from mechanical removal of surface char. The test environment also provided a controlled thermal boundary condition and allowed for in-depth decomposition to be monitored as a function of time and space. With the additional use of embedded thermocouples, the results provided a means of quantifying the intumescence as a function of char state and heating rate for validating the analytic model. These tests allowed for the material intumescence properties to be quantified and incorporated into the analytic model. The resulting validated model was then applied to a low-shear hypersonic convective thermal environment for which test data had been previously collected. This provided verification and an additional level of confidence in the model for low-shear, hypersonic flight applications. The validated model was then utilized for a sea level supersonic sled test environment to evaluate the high-shear, aerothermal environment applicability. These results provided an indication of the model

accuracy in an actual free stream air environment for various levels of mechanical shear. The comparisons of predictions with test data for the convective aerothermal environments allowed for the identification of sensitivities to mechanical shear and the necessity to further enhance the analytic approach through modeling mechanical erosion.

#### **D. Expected Results**

The expected results for this research include a validated numerical model of the intumescent behavior of thermochemically decomposing heatshield materials. The analytic model provides the unique ability to quantify intumescence properties applicable over a wide range of aerothermal environments. Through the development of an intumescence model, thermodynamic properties of the various decomposing layers could be more accurately quantified as opposed to assuming “effective” properties. During this model development, it was also anticipated that specific experimental methods would be defined to support analytic modeling of any heatshield material. These methods include experimental approaches to obtaining transient intumescence properties, char state thermodynamic properties, thermochemical analysis procedures for assessing the char chemical species, and relative mechanical shear strength of the various char states. Additionally, it was anticipated that through application of the analytic model to high shear convective aerothermal environments, the importance of modeling mechanical shear would be indicated giving credence to performing future research for developing analytic models of mechanical shear coupled to the intumescence model. The intumescence phenomena of heatshield materials have exhibited a significant capability for providing thermal protection from hypersonic aerothermal environments. The uniqueness of the analytic model presented in this research is identified through the ability to quantify specific thermodynamic phenomena previously ignored or approximated in heatshield analysis and design.

## II. DISCUSSION OF THEORY

### A. Thermodynamic Phenomena Overview

A schematic of the physical processes that occur for heatshield materials during exposure to aerothermal environments can be seen in Figure 2. It is quickly evident that a significant level of chemical reactions, mechanical interactions, and boundary layer effects are possible during the heating and corresponding out-gassing of decomposing materials. The following is a discussion of each of the parameters specifically identified in Figure 2.

#### 1. Free-Stream Flow

The free-stream flow represents the resulting airflow over a missile airframe during flight. This term also represents the flow imparted over a test item during aerothermal experimentation.

#### 2. Boundary Layer

The boundary layer is defined as the viscous region adjacent to a surface exposed to aerodynamic flow. The analytic modeling of boundary layer flow is extensively discussed in Schlichting [6] and the methodology defined there is utilized in this research effort.

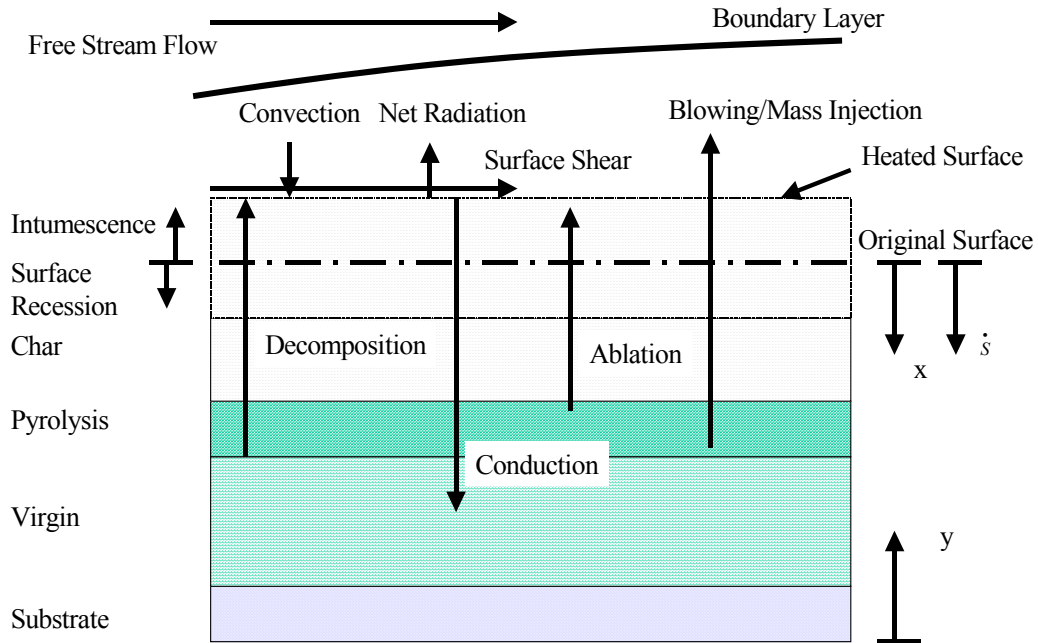


Figure 2. Schematic Description of Thermochemical Decomposition Phenomena

### 3. Convective & Radiative Heat Transfer

The convection heat transfer term corresponds to the thermal effects of aerodynamic flow over a missile airframe. The resulting viscous dissipation within the boundary layer results in a temperature rise at the wall surface. The net radiation term defines the external radiation energy exchange between the external reservoir and the heatshield surface temperature. A more detailed discussion of the convective and radiative heat transfer phenomena and corresponding terms for analytically predicting the relative influence on material thermodynamic behavior are available in a variety of references [7] [8]. A short primer is provided in Section II.C.

### 4. Chemical Diffusion/Reactions

The chemical diffusion and reaction processes are a result of gas generation from the thermochemically decomposing material being injected through the solid surface into the boundary layer. Additional reactions can occur between the solid surface and boundary layer gas species. The reaction kinetics and diffusion rates are highly dependent on the free-stream and injected gas components. For heatshields dominated by mechanical erosion, these rates are less important than for materials having a high level of decomposition and gas injection.

### 5. Decomposition

As a heatshield material is exposed to a sufficient level of convective or radiative heat transfer, the in-depth thermal gradients induce relative levels of thermochemical decomposition. The decomposition is a response to material achieving temperatures at which specific components that make up that material begin to react and give off gaseous products. The corresponding gas loss reduces the material density. This density reduction is quantified through the use of Thermogravimetric Analysis (TGA) [9] during which a finitely small sample of material is heated in an inert medium while recording weight and calculating weight loss rate. Since the sample is sufficiently small, the weight can be considered proportional to the density. The decomposition region is defined by two material states. Use of an inert medium while heating the sample eliminates the potential influence of reactions with air and represents the in-depth thermodynamic response of the decomposing material where air is not present due to pressure gradients. A brief description of the specific terms considered in the analytic heatshield model follows.

#### a. Char

The char term is defined by the fully decomposed or fully reacted heatshield material region and is quantified during TGA where no appreciable density changes occur during additional temperature rise. This region can vary significantly depending on the level of thermochemical ablation and mechanical erosion. The char layer is typically of a black carbonaceous nature. However, the char can also be represented by a combination of a variety of non-reacting species that collect on the surface.

## b. Pyrolysis

The pyrolysis region is defined as the layer at which the heated material is undergoing thermodynamic reactions and is bounded by the fully reacted char layer and the non-reacting virgin material. This is the region from which the pyrolysis gases are generated and percolated through the char to the boundary layer. It is also considered, for this research, the primary region where intumescence occurs and expansion of the conduction path moves the heated surface away from the substrate.

## 6. Blowing/Mass Injection

The evolving gases due to decomposition are percolated up from the pyrolyzing layers through the fully decomposed porous char layer and injected into the boundary layer. As a result of the mass injection, the boundary layer thickness increases, providing a potential reduction in heat transfer from the boundary layer edge to the heated surface. Depending on the severity of the thermal environment, these gases can also react with air in the boundary layer.

## 7. Surface Shear

In some cases, if the char layer does not have sufficient structural integrity for the given aerodynamic shear, the char is mechanically removed until a region is reached at which the char strength is sufficient to withstand the aerodynamic shear. If the thermal environment induces high enthalpies, some heatshield materials can thermochemically ablate and react in the boundary layer as opposed to mechanical erosion. However, for high-speed aerodynamic heating and sufficiently weak char layers, the mechanical shear removal typically dominates the ablation process and can greatly reduce the influence of thermochemical ablation.

## 8. Surface Recession/Intumescence

The surface recession term is defined as the mechanical or thermochemical removal of condensed species from the surface of the heatshield material. This phenomenon is highly dependent on the level of aerodynamic shear, heatshield char strength, enthalpy level, reactivity of boundary layer gases, and surface material decomposition state. The intumescence is a direct result of the internal thermodynamic decomposition causing a range of expansion levels of the pyrolyzing material. The specific difference in the existing non-intumescing and new intumescing models is contained in the ability to model the effect intumescence or swelling has on conduction heat transfer into the decomposing material. Figure 1 provided a schematic of this difference. A variety of approaches such as thermal expansion [10] and equivalent thermal properties [11] have been defined in an attempt to model this behavior with varied success. A new approach will be presented for intumescence relating the pyrolysis region expansion to decomposition state and heating rate with the goal of more accurately capturing the thermodynamic phenomenon and relative effects on conduction heat transfer.



## B. Theoretical Model of Phenomena

### 1. Existing Model Development

The theoretical model of the phenomena discussed in Section II.A is formulated on the principal use of the First Law of Thermodynamics to derive the thermomechanically Coupled heat conduction equation discussed in more detail by Chung [12]. This approach is compared to various simpler techniques of modeling ablation by Russell [13] and gives an indication of the complexity of ablation phenomena. The in-depth energy balance for a heatshield material initiates with

$$\dot{K} + \dot{U} = M + \Sigma E , \quad (1)$$

where  $\dot{K}$  is the time rate of change of kinetic energy,  $\dot{U}$  is the time rate of change of internal energy,  $M$  is the mechanical energy, and  $\Sigma E$  represents the remaining energies per unit time such as heat, magnetic, electrical, and chemical.

For the thermochemical decomposition model, conservation of mass equation is

$$\left. \frac{\partial \dot{m}_g}{\partial y} \right|_{\theta} = A \left. \frac{\partial \rho}{\partial \theta} \right|_y . \quad (2)$$

For this discussion, the subscripts 0, 1, and 2 represent the unreacted, reacting, and completely reacted components of the material. It is typically assumed that while pyrolysis gases are escaping the material through the char and into the boundary layer, the pressure differences in the material pyrolysis and char layers are insignificant so as to satisfy the momentum equation, as discussed by Hurwicz [14].

Through the use of conservation laws, the Green-Gauss Theorem and Helmholtz free energy relationship, Cauchy's first law of motion and energy can be derived.

$$\sigma_{ij,i} + \rho F_j - \rho \dot{v}_j = 0 \quad (3)$$

and

$$\rho \dot{\epsilon} = \sigma_{ij} v_{i,j} + q_{i,i} + \rho q_{gen} . \quad (4)$$

The three terms in Equation (3) are identically zero, due to the assumption that stresses in the material do not induce temperature changes, satisfying the momentum equation. Equation (4) can be reduced to the energy balance

$$\rho \dot{\mathcal{E}} = q_{i,i} + \rho q_{gen} . \quad (5)$$

The total heat flux added to the in-depth control volume with terms of combustion and gas flow is

$$dQ = dQ_{cond} + dQ_g + dQ_{chem} , \quad (6)$$

where the conduction heat transfer term is

$$dQ_{cond} = \frac{\partial}{\partial x} \left( k \frac{\partial T}{\partial x} \right) dx d\theta , \quad (7)$$

the pyrolysis gas flow heat transfer is

$$dQ_g = \frac{\partial}{\partial x} (\dot{m}_g H_g) dx d\theta , \quad (8)$$

and the chemical reaction heat transfer is

$$dQ_{chem} = \dot{\rho}_1 \Delta H_c dx d\theta , \quad (9)$$

neglecting in-depth radiant energy transfer. Continuing with the assumptions discussed by Chung [15] for a constant specific heat of the gaseous decomposition products,  $C_{p_g}$ , and assuming thermal equilibrium the heat transfer by gas flow can be written as

$$dQ_g = C_{p_g} \left( m_g \frac{\partial T}{\partial x} + \dot{\rho}_1 T \right) dx d\theta . \quad (10)$$

It should be noted that the CMA code allows for a variable  $C_{p_g}$  to be utilized based on the user defined gas conditions such as chemical equilibrium. By relating total heat flux,  $dQ$ , to the change in enthalpy of the control volume and neglecting higher order differential products, shown by Hurwicz [16], Equation (11) results.

$$\frac{d}{d\theta}(\rho H) = \frac{\partial}{\partial x} \left( k \frac{\partial T}{\partial x} \right) + C_{p_g} \dot{m}_g \frac{\partial T}{\partial x} + \dot{\rho}_l (C_{p_g} T + \Delta H_c) , \quad (11)$$

with the surface boundary conditions shown in Figure 2:

$$\begin{aligned} -k \frac{\partial T}{\partial x} \Big|_{x=s} &= q_c(\theta) - q_r(\theta) - \rho_2 \dot{s} [H_v + \eta_c (H_r - H_w)] \\ &- (\rho_s - \rho_2) \dot{s} [\Delta H_c + \eta_g (H_r - H_w)] - \dot{m}_g(s) \eta_g (H_r - H_w) \end{aligned} \quad (12)$$

and an adiabatic backside surface with the initial conditions

$$T = T_o \Big|_{\theta=0} \quad (13)$$

$$\rho = \rho_o \Big|_{\theta=0} . \quad (14)$$

In these equations,  $\eta_g$  is the blowing factor attributed to the pyrolysis gases affecting the heat transfer to the surface,  $\eta_c$  is the blowing factor for the char accounting for the effect the eroded char has on the heat transfer to the surface,  $\rho_s$  is the surface material density, and  $\dot{m}_g(s)$  is the gas flow rate per unit area leaving the surface. It should be noted that the existing numerical model maintains a constant node thickness in Equations (11) and (12). The current addition of intumescence allows for an increase in conduction path length as a function of char state and heating rate. This addition is specifically defined in the iterative solution during the in-depth energy balance to define thermal gradients. A more detailed discussion of this modification is provided in Section II.B.2 and the numerical model discussion provided in Section XII.

The blowing term represents the gaseous diffusion of the decomposing material into the boundary layer causing a thickening of the boundary layer and a reduction in the boundary layer temperature gradient. It can be thought of as the ratio of convective heat transfer with mass injection to that without mass injection. The blowing consists of the difference between the recovery enthalpy,  $H_r$ , and the wall enthalpy,  $H_w$ , multiplied by the blowing or blockage factor. The blowing factor,  $\eta$ , represents the percent that the heat transfer is reduced due to this thickening. The blowing factor is a function of the mass injection rate of the surface

gases, properties of the injected gas and local flow conditions. The blowing factor is reasonably well defined for laminar flow in air as provided by Katsikas et al. [17], and varies with the molecular weight of the injected species as

$$\eta_{lam} = 0.7 \left( \frac{29}{M_v} \right)^a, \quad (15)$$

where  $0.25 < a < 0.4$  and  $M_v$  is the molecular weight of the injected species. For turbulent flow the approximation

$$\eta_{turb} = \frac{1}{3} \eta_{lam} \quad (16)$$

is recommended. There are several models available for calculating the blowing factor. Each model is based on empirical correlations and can vary somewhat. The parameters used in the numerical model for blowing are somewhat modified versions of those discussed above and are given in Section VI.

The  $\dot{s}$  term shown in Equation (12) defines the recession rate of the surface and must be specifically defined. Munson and Spindler [18] discuss a method for modeling the ablation rate for a charring material using an Arrhenius rate relationship:

$$\dot{s} = \beta_1 T_s^{\beta_2} e^{-\beta_3 / T_s}, \quad (17)$$

where the constants,  $\beta_1$ ,  $\beta_2$ , and  $\beta_3$  are empirically determined through the simultaneous measurement of recession rate,  $\dot{s}$ , and surface temperature,  $T_s$  for a given aerothermal environment. The present form of CMA does not specifically associate the recession rate with aerodynamic shear.

## 2. Intumescence Phenomena Model

The intumescence phenomenon has been documented in a variety of analytic investigations of heatshield materials. In particular, when heatshields are utilized as internal insulators for rocket motors, a significant level of intumescence can occur affording additional insulative value. During the Ramburner Internal Insulation Investigation [19], an extensive quantitative effort was performed to better understand the thermodynamic behavior of the motor internal insulation, DC93-104. In support of this effort, Laub et al. [20] performed detailed radiographic and chemical analyses to quantify chemical species of the various char states as well as attempted to map the location of thermocouples to quantify expansion or intumescence of the various char layers. Significant advances resulted from these investigations with the exception of quantifying the transient intumescence phenomena. During the period of the Ramburner Investigation, transient radiography was not readily available to the investigators

resulting in the measurement of only the pretest and posttest thermocouple position. Since the heatshield experienced significant thermochemical decomposition and transient intumescence, an analytic model of the intumescence as a function of char state or other material property could not be validated. As a result, the Charring Material Thermal Response and Ablation Program [21] could not be modified to incorporate the effects of intumescence on the in-depth energy balance. However, based on these experiments, the recognition for the need to quantify the transient intumescence phenomena was identified. This phenomena was again observed during a heatshield test and evaluation program [22] in which the intumescence was such that simplified modeling techniques could not readily be used to predict heatshield thickness requirements until a more in-depth study of char state thickness could be performed [23] to produce limited applicability. As a result of these analytical and experimental findings, the dissertation topic presented here was directed to identifying a method of theoretically predicting intumescent behavior of heatshields along with validation efforts for specific environments. As shown in Figures 1 and 2, the intumescence behavior increases the conduction path and can correspondingly reduce conduction heat transfer into the material. The current numerical technique for modeling thermochemically decomposing materials requires a constant nodal thickness throughout the material restricting the incorporation of intumescence phenomena and resulting effects on thermal gradients. The efforts devoted toward the current research represent a unique and more rigorous approach for modeling intumescent materials and incorporate the ability to modify node dimensions for calculating in-depth thermal response.

The initially proposed analytic expression for modeling the intumescence as a function of char state is shown below

$$L = fnc(\varphi), \quad (18)$$

where  $L$  is the node thickness (as related to the  $x$  coordinate system in the numerical scheme) and  $\varphi$  is an expression quantifying char state. The change in  $L$  ( $\partial L$ ) is related to the change in  $x$  ( $\partial x$ ) as shown in the first term (conduction term) on the right hand side of Equation (11) and the left hand term in Equation (12). The intumescence of any element within the decomposing material is defined as

$$\frac{\partial L}{\partial \theta} = \frac{\partial L}{\partial \varphi} \frac{\partial \varphi}{\partial \theta} \quad (19)$$

The char state is a function of the virgin and fully charred material defined as

$$\varphi = \frac{\rho_v - \rho}{\rho_v - \rho_c}, \quad (20)$$

where the subscripts  $v$  and  $c$  represent the virgin and fully charred conditions, and  $\rho$  is the instantaneous density. Differentiating the char state with respect to time provides

$$\frac{\partial \phi}{\partial \theta} = - \frac{1}{\rho_v - \rho_c} \frac{\partial \rho}{\partial \theta} \quad (21)$$

Combining terms results in the expression for intumescence

$$\frac{\partial L}{\partial \theta} = - \frac{1}{\rho_v - \rho_c} \frac{\partial \rho}{\partial \theta} \frac{\partial L}{\partial \phi} \quad (22)$$

These expressions provide the basis for relating intumescence to char state for the thermochemically decomposing material. TGA and Differential Scanning Calorimetry (DSC) are used to quantify the reactions and resulting pyrolysis gas generation defining material density changes. The virgin and charred material densities are constant based on laboratory measurements and TGA. The fully charred state is identified using TGA and locating the conditions where no additional decomposition occurs. It is important to obtain TGA data for heating rates and temperature ranges which will be experienced during actual flight environments. The remaining expression,  $\partial L / \partial \phi$ , must be formulated to model the actual intumescence of the material. Until additional research and development is devoted to understanding on a micro scale, the material properties that cause growth, tabularized data must be used. These data must be collected during flight similar hypersonic aerothermal test and evaluation programs in which real time radiography of intumescence and decomposition as well as pre- and post- test intumescence are measured. Along with transient intumescence and decomposition measurements, in-depth thermocouple measurements must be collected to verify in-depth thermal response and thermal properties of the various decomposition states.

The  $\partial L / \partial \phi$  contribution to the intumescence relationships was selected utilizing a variety of analytic and experimental means. Oven tests were performed to correlate material color with char state. These oven tests also provided an indication of the onset and termination of intumescence for the respective heating rate. The laser facility tests provided the most useful data as a result of recording transient radiography. This allowed for validating both char surface position and internal layer position as a function of time. These results coupled with the density measurements through the thickness as a function of time allowed for very accurate predictions of in-depth thermochemical decomposition and intumescence. The embedded thermocouples provided a means of quantifying the thermal properties of the various char states. Since the thermocouple locations, density gradients, and temperatures were known as a function of time, reasonable accuracy could be assumed with respect to thermal properties such as thermal conductivity and specific heat.

It was discovered through experimental validation that the intumescence model was also highly dependent on heating rate to define the onset and termination of intumescence. While the rate of change of char state is heating rate dependent, it was necessary to specifically define the heating rate dependency to adequately model each of the aerothermal environments. As a result, the  $\partial L / \partial \phi$  term was defined in tabular form as a function of both decomposition state

and heating rate to provide an approximate method of quantifying intumescence. The tabular data was collected from the various aerothermal tests and imposed as a multiplier of the non-intumescing thickness. The resulting relationship to define the char state and heating rate dependent intumescence is shown in Equation (23).

$$\frac{\partial L}{\partial \varphi} \propto LFAC(\varphi) * LFAC(\dot{q}) * L_{initial} \text{ for } (100^\circ\text{C} / \text{min} \leq \dot{q} \leq 20000^\circ\text{C} / \text{min}). \quad (23)$$

This expression essentially represents the use of multipliers for char state and heating rate effects on the initial node thickness for each time step. These multipliers are characteristic of material properties and since they incorporate both decomposition state and heating rate, they should be applicable to a variety of aerothermal environments. The laser test facility was utilized to isolate and quantify these intumescence properties for the analytic model. The resulting overall intumescence as defined in Equation (22) is utilized in the in-depth energy balance to define conduction path length and in-depth heat transfer.

The data collected during the LHMEI tests provided the regions of intumescence as a function of char state and heating rate used to establish the  $\partial L / \partial \varphi$  tabular model. The resulting tabular multiplier generated and validated for the laser thermal testing was also used for predicting intumescence and in-depth thermal response for the NASA Hot Gas Test Facility high altitude hypersonic aerothermal testing (Test 3) and the Holloman High Speed Test Track testing (Test 4). These predictions provided very good agreement with post-test measured decomposition and intumescence data as well as embedded thermocouple data for the lower shear conditions. However, the comparisons are not as good for the higher shear conditions. Additional research and the future incorporation of a mechanical erosion model will provide better agreement for Test 4 accounting for the higher shear levels.

These expressions have been incorporated into the existing CMA program by coupling the intumescence to the in-depth energy balance. This allowed for a conduction path growth and increased resistance to in-depth heat transfer.

## C. Convective & Radiative Heat Transfer

### 1. Conventional Definition of Convective Heat Transfer

The necessity for heatshields is a result of aerodynamic heating and its adverse effect on material structural performance. When system optimization becomes more important for flight performance, weight constraints are placed on the system requiring the use of advanced lightweight materials and minimization of structure thickness. To accommodate system optimization, composite materials are utilized having much lower thermostructural thresholds than metals. To maintain these composites below thermal constraints, the lightweight sacrificial heatshield material is applied to the composite external surface. The viscous dissipation within the boundary layer along the surface of the heatshield results in convective heat transfer. As the wall temperature rises, the radiation interchange with the surroundings increases.

The derivation of the equations required to calculate heat transfer to structures using boundary layer theory has been extensively performed in numerous references and, therefore, only the pertinent equations required for calculating heat transfer will be presented here.

As discussed by Harms [24], it has been shown that heating to structures can be modeled using Newton's Law of Cooling:

$$\frac{Q}{A_{cs}} = q = h \Delta T \quad , \quad (24)$$

where  $\Delta T$  is the forcing function or difference in temperature between the heat source and the receiving medium. To continue the development of the convective heat transfer equations several parameters must be defined.

The Reynolds number,  $Re$ , is the ratio of momentum forces to viscous forces of the fluid and is defined as

$$Re = \frac{\rho V L_c}{\mu} \quad . \quad (25)$$

The Nusselt number,  $Nu$ , is the ratio of convective to conductive heat transfer and is defined as

$$Nu = \frac{h L_c}{k} \quad . \quad (26)$$

Solving Equation (26) for  $h$  and combining the result with Equation (24),

$$Nu = \frac{q_c}{\left( \frac{k \Delta T}{L_c} \right)} \quad , \quad (27)$$

which can be further modified to

$$Nu = \frac{\left. \frac{\partial T}{\partial y} \right|_{y=0}}{\left( \frac{\Delta T}{L_c} \right)} \quad , \quad (28)$$

where  $y$  is the coordinate normal to the surface and represents the fluid region, and  $\partial T / \partial y$  is the temperature gradient at the wall in the direction normal to the surface through the fluid.



The Stanton number,  $St$ , represents the ratio of heat convected to heat available in the fluid. The Stanton number is defined as

$$St = \frac{h}{3600 \rho V C_p} \quad . \quad (29)$$

The Prandtl number,  $Pr$ , relates the mechanisms which produce the flow boundary layer and the thermal boundary layer and is defined as

$$Pr = 3600 \frac{\mu C_p}{k} \quad . \quad (30)$$

The Nusselt number can be expressed as a function of the Reynolds, Stanton, and Prandtl numbers:

$$Nu = f(St, Re, Pr) \quad . \quad (31)$$

For the case of steady-state aerodynamic heating, if the geometry is exposed for a sufficiently long time and if radiative and conductive heat transfer is eliminated, the convective heat flux will approach zero because the wall temperature will approach the adiabatic wall or recovery temperature,  $T_r$ . Depending on the type of aerodynamic heating, as well as free stream conditions, the recovery temperature can be either less than or greater than the total temperature,  $T_T$ , because the fluid is not brought to rest adiabatically. If  $Pr$  is less than 1, then  $T_r$  will be less than the total temperature due to heat loss to the fluid outside the boundary layer. If  $Pr$  is greater than 1, then the  $T_r$  will be greater than the total temperature due to heat conducted into the thermal boundary layer. The method used to determine  $T_r$  requires the introduction of a simplifying parameter called the recovery factor,  $r$ :

$$r = \frac{T_r - T}{T_T - T} \quad . \quad (32)$$

The recovery factor provides a means of accounting for the irreversibilities and is a measure of the ability of the fluid to convert kinetic energy to heat energy by viscous dissipation. It has been shown experimentally and analytically that a simplified relationship for the recovery factor can be used for laminar and turbulent flow.

$$r = \sqrt{Pr} \quad \text{Laminar flow} \quad (33)$$

$$r = \sqrt[3]{Pr} \quad \text{Turbulent flow} \quad . \quad (34)$$

For air, these equations give recovery factors for laminar and turbulent flow of 0.85 and 0.90, respectively.

Because, in high-speed flow the temperature of the fluid can vary significantly between the free stream and close to the wall due to compressibility effects, a means of determining a temperature used to evaluate fluid properties providing the best accuracy is desirable. Eckert [25] suggests the use of the following equation to determine fluid properties.

$$T^* = 0.5(T_\delta + T_w) + 0.22(T_r - T_\delta) . \quad (35)$$

The variable,  $T_\delta$ , is the local temperature at the boundary layer interface with the free stream. Eckert's reference temperature,  $T^*$ , is a weighted mean of the wall, local static, and stagnation temperatures.

For the aerodynamic heating case, by identifying the forcing function, Equation (24) can be further expanded to

$$q_c = h ( T_r - T_w ) . \quad (36)$$

Rearranging Equation (36) and solving for the heat transfer coefficient as shown by Schlichting [26],

$$h = \frac{q_c}{T_r - T_w} = \frac{k_w \frac{\partial T}{\partial y} \big|_{y=0}}{T_r - T_w} , \quad (37)$$

where  $k_w$  is the thermal conductivity of the fluid at the wall. The slope of the temperature distribution through the boundary layer, evaluated at the wall, must be determined in order to evaluate the heat transfer coefficient.

Due to the complexity of turbulent flow fields and the lack of understanding of turbulent exchange of momentum and energy, it is necessary to determine heat transfer parameters experimentally. The exact solution offered by Pohlhausen [27] for laminar flow with the Prandtl Number correlation is

$$Nu = 0.332 Re^{\frac{1}{2}} Pr^{\frac{1}{3}} , \quad (38)$$

and for turbulent flow Colburn [28] suggests the use of

$$Nu = 0.0296 Re^{\frac{4}{5}} Pr^{\frac{1}{3}} , \quad (39)$$

determined through experimental analysis of skin friction measurements for turbulent flow. The resulting equations for the heat transfer coefficient for laminar and turbulent flat plate flow are

$$h = 0.332 \frac{k}{x} Re^{\frac{1}{2}} Pr^{\frac{1}{3}} \quad \text{Laminar} \quad (40)$$

$$h = 0.0296 \frac{k}{x} Re^{\frac{4}{5}} Pr^{\frac{1}{3}} \quad \text{Turbulent} . \quad (41)$$

For conical flow the constants used in Equations (40) and (41) must be modified. The laminar heat transfer coefficient must be multiplied by 1.732 and the turbulent heat transfer coefficient multiplied by 1.15. The resulting conical flow heat transfer coefficients are

$$h = 0.575 \frac{k}{x} Re^{\frac{1}{2}} Pr^{\frac{1}{3}} \quad \text{Laminar} \quad (42)$$

$$h = 0.034 \frac{k}{x} Re^{\frac{4}{5}} Pr^{\frac{1}{3}} \quad \text{Turbulent} \quad (43)$$

for laminar and turbulent flow, respectively. These equations represent the general convective heat transfer correlations from which the convective boundary conditions were obtained for the Simplified Heat of Ablation model [29]. Similar relationships were used to develop the convective boundary conditions for the more complex model, CMA, and are discussed in more detail in Murray [30].

## 2. Radiation Heat Transfer

The definition of thermal radiation interchange as defined by White [31] is the emittance by atomic excitation of any substance with the radiant energy traveling at the speed of light until it strikes another substance where it can be absorbed, reflected, transmitted, or scattered. The resulting mathematical formulation for the radiative flux from a heated surface is defined as

$$q_{rad} = \varepsilon \sigma T_w^4 . \quad (44)$$

The emissivity,  $\varepsilon$ , is a function of temperature and can vary as a function of the relative decomposition state of the material. For most heatshield materials, an acceptable value of emissivity is in the range of 0.8 to 0.9. This is generally a result of the black carbonaceous char that is generated as thermochemical decomposition occurs. However, for various heatshield materials with multiple char constituents, this value may differ. If a shiny siliceous char condenses on the surface, the emissivity may be reduced affecting the total absorbed energy. Under high shear aerothermal environments, the emissivity takes on a less important role due to the dominant convective heating contribution. It is imperative that during test and evaluation of heatshield materials the surface emissivity be measured to ensure accurate surface temperatures are recorded. Since embedded thermocouple data must be used for the various heating rates to quantify char state thermal properties, accurate surface temperatures must also be collected to ensure the in-depth heat flux is correct. This importance is represented in Equation (45). The wall temperature reradiates to the surroundings that can range from very low to very high temperatures depending on the relative humidity as well as other factors [32]. The net radiation for a heatshield is

$$q_{rad} = \sigma \varepsilon F (T_{surr}^4 - T_w^4) , \quad (45)$$

where  $F$  is the view factor and is a function of geometry.

### **III. DISCUSSION OF NUMERICAL MODELS**

#### **A. Numerical Modeling Process**

Development of numerical models of intumescent heatshield materials requires a significant level of understanding of the thermodynamic phenomenon. Generally, these phenomena are quantified through the use of a variety of experimental methods requiring a rigorous design of experiments effort to quantitatively capture the material properties. Thermochemical decomposition requires the use of TGA and DSC. Intumescence phenomena must be quantified through accurate tracking of the surface position as a function of time. However, additional in-depth intumescence must also be quantified due to the variation of intumescence for a range of decomposition states. As a result, it is imperative to utilize real-time radiography to capture spatially and temporally the decomposition and intumescence behavior. Having these phenomena quantified assures the analytic model's accuracy and applicability over a wide range of aerothermal environments. The final experimental evaluation should include realistic aerothermal environments to validate the model's applicability to convective type heating. These environments also subject the materials to flight aerodynamic shear to assess mechanical erosion.

Figure 3 provides a flowchart that defines the various experimental methods utilized to quantify ablation phenomena for developing analytic models. As can be seen, the aerothermal boundary conditions of the flight environment of interest must be quantified to determine what laboratory tests must be performed. Again, these tests must quantify phenomenon such as intumescence, decomposition, conduction heat transfer, and mechanical and thermochemical erosion. These properties are then used to predict expected thermal performance for actual aerothermal environments. Depending on the level of accuracy and applicability of the laboratory experiments in quantifying the thermophysical response, some level of model refinement may be necessary based on the aerothermal test results. Upon completion of simulated flight validation of the analytic model, predictions can then be performed for the actual flight configuration and any range of trajectories to perform system optimization. This process has the potential to reduce flight test requirements, test schedule, and hardware dedicated to flight validate external thermal protection systems.

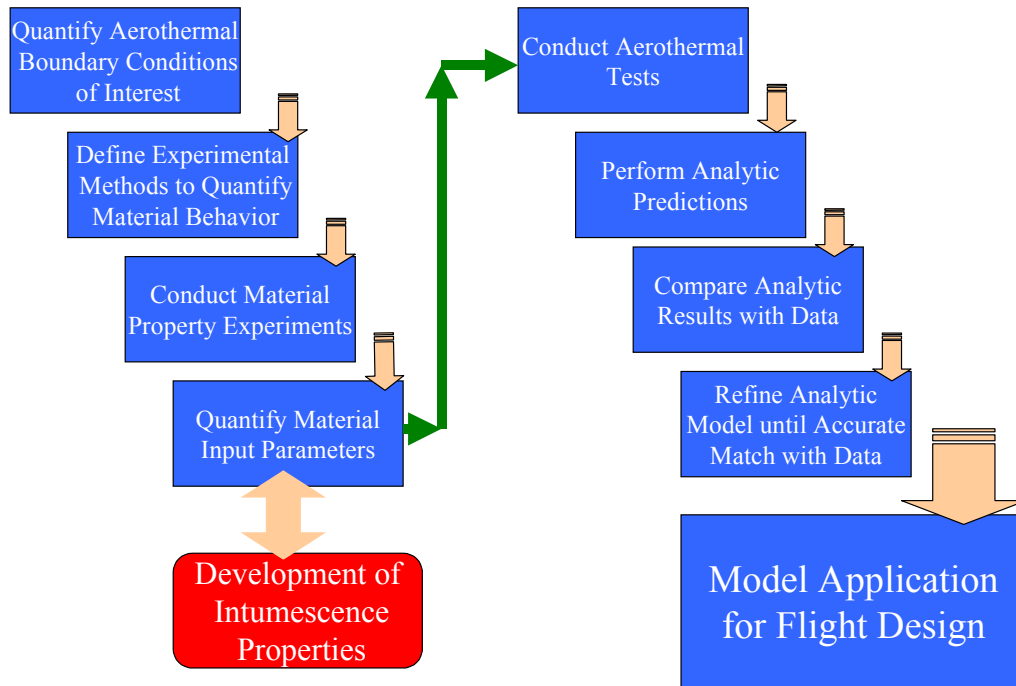


*Figure 3. Model Development Process*

## **B. Thermochemical Decomposition Model**

### **1. Description**

As discussed in Section I, the thermochemical decomposition numerical model has been extensively documented through the years. The approach to providing a means of analytically predicting specific behavior of decomposing heatshield materials has been of great interest to missile design engineers due to the excessive heat loads of reentry and hypersonic flight. In the initial stages of understanding ablation phenomena, semi-empirical models were developed such as SHOA model [33]. This approach was design efficient and adequate as long as experiments could be carried out having similar thermal environments to those of flight. However, as design requirements were refined, optimization played a more significant role in missile design. This required refinement of thermal protection system design to minimize weight while providing increased thermal protection. To obtain this analytical refinement in design of thermal protection systems, more accurate models of the ablation phenomena were required. Section II provided an overview of the various contributors to the ablation process exhibiting the level of complexity of modeling ablation. In response to the need for a more accurate characterization of the ablation phenomena desired for typical reentry vehicle thermal design, significant steps toward providing a more theoretical model of heatshield thermodynamic behavior was developed by Moyer et al. [34] and called the Aerotherm Charring Material Thermal Response and Ablation Computer Program.

This program provided a means of individually modeling much of the ablation phenomena allowing for identification of specific contributors to providing insulation capability. This program has application to external and internal heatshield materials as well as nozzle insulation materials due to the more rigorous handling of ablation and in-depth heat transfer. However, due to the limited experimental methods available during the period of code development, while some phenomena were recognized as contributors to the ablation and heat transfer process, they could not adequately be measured to ensure validation of the mathematical relationships. This was specifically noted during the work of Laub et al. [35] [36] [37], where intumescence and mechanical erosion were identified as significant but could not be adequately measured.

With the increased interest in hypersonics and long flight times, these contributions have again taken on an increased level of importance. The objective of the current research was to enhance the theoretical approach for modeling ablation and heat transfer of thermochemically decomposing materials by adding the ability to model intumescence and corresponding effects on the surface and in-depth energy balances. A discussion of the pertinent derivations and resulting finite difference expressions is provided with a more complete discussion of derivations and resulting expressions provided in Appendix A.

## 2. In-depth Energy Differential Equations

Mathematically representing the terms shown in Figure 2 as discussed by Moyer et al. [38], the differential equation defining the in-depth energy balance is

$$\frac{\partial}{\partial \theta}(\rho h A)_y = \frac{\partial}{\partial y} \left( k A \frac{\partial T}{\partial y} \right)_\theta + \frac{\partial}{\partial y} (\dot{m}_g h_g)_\theta \quad . \quad (46)$$

The conservation of mass for a chemically decomposing material is defined as

$$\frac{\partial \dot{m}}{\partial y} \bigg|_\theta = A \frac{\partial \rho}{\partial \theta} \bigg|_y \quad , \quad (47)$$

where mass transfer is associated with the pyrolyzing constituents percolating through the char assuming no reaction with the char (coking). It is necessary to further evaluate the partial derivative on the right side of the equation to characterize the material decomposition rate. As pointed out by Rohsenow and Hartnett [39], the use of an Arrhenius type fit has been found to adequately model the decomposition behavior of thermochemically decomposing materials. The expression is written as

$$\frac{\partial \rho}{\partial \theta} \bigg|_y = -P_F e^{\frac{-E}{RT}} \rho_o \left( \frac{\rho - \rho_r}{\rho_o} \right)^n \quad . \quad (48)$$

The expression for density can be defined in terms of a variety of reacting components combined to form the single material. TGA characterizes the weight loss and weight loss rate based on specific reactions occurring in the material while being heated. The general form of the expression is

$$\rho = \Gamma \sum \rho_i + (1 - \Gamma) \sum \rho_j \quad (49)$$

where  $\Gamma$  represents the volume fraction of effective resin to effective reinforcement, the subscripts  $i$  and  $j$  represent the various reactions attributable to the resin and reinforcement densities, respectively. The general approach for using this model is to assume a three-component material where the first two components represent the first two resin reactions and the final component is the reinforcement reaction identified from TGA. However, recent modifications to the mathematical model of density change have incorporated the ability to model more than three reactions that can occur for the highly decomposing materials of interest for this research.

These expressions represent the in-depth energy balance for decomposing materials. They incorporate the condensed form of various terms defined in Figure 2. The “y” coordinate defines the “fixed” to the back surface spatial system. A transformation is performed to obtain “x” or a “moving” coordinate system referenced to the heated surface. The nodal thicknesses along the x coordinate are fixed in the existing CMA numerical scheme. The modification discussed in the current research defines modifications of the transient nodal thickness,  $\partial L / \partial \theta$ , along the x coordinate. This nodal thickness increase defines the intumescence phenomena. Further expansion of the specific terms will be provided in the following sections along with a more detailed discussion of the finite difference formulations in Appendix A.



### 3. Boundary Conditions

The surface boundary conditions defined for the thermochemical decomposition model are shown in Figure 4. This figure provides each of the terms specifically handled in the numerical scheme.

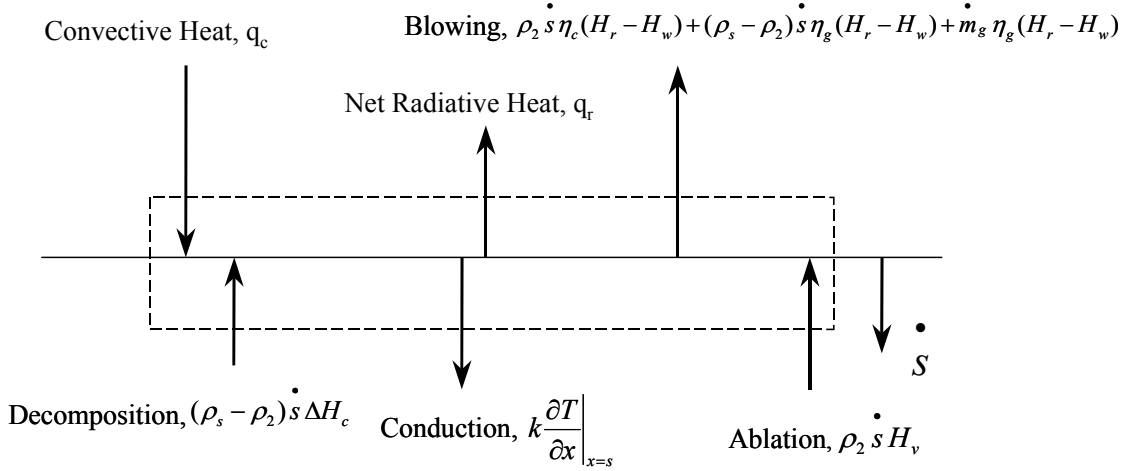


Figure 4. Surface Boundary Condition Schematic

The control volume is allowed to move with the receding surface as ablation/erosion occurs. The energy fluxes entering the control volume include radiation from the boundary layer, char and pyrolysis gas mass flow rate enthalpy, and all diffusive energy fluxes from the gas boundary layer. The exiting energy terms represent the conduction, reradiation, condensed phase material removal (thermochemical/mechanical), and blowing at the surface.

### 4. Finite Difference Formulation

The existing mathematical model is a finite differencing scheme and requires fixed node sizes. To account for surface removal, nodes are removed from the backside of the ablating material such that the nodal network is referenced to the receding surface. A transformation of the differential equations is performed from the global or “fixed” coordinate system to a body or “moving” coordinate system. This approach also allows for conservation of energy and mass. The difference form of the energy equation reduces to the conservation of mass equation when temperature and enthalpy are uniform. These finite difference equations are implicit in temperature. However, the decomposition finite difference forms are explicit in temperature. The decomposition nodal network utilizes a refinement of the thermal nodal network to provide better resolution of decomposition gradients. The resolution is user defined and should be based on the required level of refinement to capture density gradients through the decomposing material.

The process utilized in the numerical scheme first involves the calculation of the decomposition gradients using the fixed nodal and nodelet thicknesses. Then the intumescence or nodal thicknesses are determined using the char state and heating rate obtained during the decomposition gradient calculation. The thermal gradients are then calculated using the intumesced nodal thicknesses. The resulting thermal gradients are used to define the decomposition gradients for each successive temporal iteration.

a. Geometry

The phenomenological schematic of the decomposition and ablation process is provided in Figure 2. Each of these parameters is defined in the finite difference equation for in-depth decomposition and surface removal.

b. Transformation of the Conservation of Mass Equation

It should again be noted that the decomposition and mass conservation equations are solved using a fixed node and nodelet thickness throughout the analysis. The assumed reaction for heatshield materials is the transformation from a plastic through a pyrolysis period reaching the fully charred state due to heating and thermochemical reactions. The mass conservation equation is

$$\left. \frac{\partial \dot{m}_g}{\partial y} \right|_{\theta} = \frac{\partial}{\partial \theta} (\rho A)_y = A \left. \frac{\partial \rho}{\partial \theta} \right|_y + \rho \left. \frac{\partial A}{\partial \theta} \right|_y, \quad (50)$$

which, as discussed in Appendix A, results in the conservation of mass expressions shown in Equations (51) (52) and (53).

$$\left. \frac{\partial \rho}{\partial \theta} \right|_y = \Gamma \left( \sum \frac{\partial \rho_i}{\partial \theta} \right) + (1 - \Gamma) \left. \left( \frac{\partial \rho_j}{\partial \theta} \right) \right|_y. \quad (51)$$

Since multiple reactions can occur during resin decomposition, a summation of the decomposition rates is used along with the assumed mass fraction ratios of resin to reinforcement. The decomposition of each reaction component is given by

$$\left. \frac{\partial \rho_i}{\partial \theta} \right|_y = -P_{Fi} e^{\frac{-E_i}{RT}} \rho_{oi} \left( \frac{\rho_i - \rho_{ri}}{\rho_{oi}} \right)^{m_i}. \quad (52)$$

The mass conservation equation transformed from y to x coordinates is

$$\left. \frac{\partial \rho}{\partial \theta} \right|_x = \left. \frac{\partial \rho}{\partial x} \right|_{\theta} \dot{S} + \left. \frac{\partial \rho}{\partial \theta} \right|_y. \quad (53)$$

c. Transformation of the Conservation of Energy Equation

The energy equation solution provides the thermal gradient and is where the node thickness is allowed to intumesce to define the increased thermal resistance or conduction path. This node thickness increase is only accounted for in the energy equation and not utilized in the decomposition gradient calculation. The basic in-depth energy balance includes energy storage, net conduction, and convection as shown in Equation (46). This equation must be transformed to the moving coordinate system as performed for the conservation of mass equation. The resulting in-depth energy balance expression for which additional development is provided in Appendix A is

$$\frac{\partial}{\partial \theta}(\rho h A)_x = \frac{\partial}{\partial x} \left( k A \frac{\partial T}{\partial x} \right)_\theta + \dot{S} \frac{\partial}{\partial x}(\rho h A)_\theta + \frac{\partial}{\partial x} \left( \dot{m}_g h_g \right)_\theta . \quad (54)$$

The conduction term containing “x” defines the nodal thickness modified according to the level of intumescence experienced for each node through the thickness of the material. The  $\partial \mathcal{L}$  term is calculated each time step and substituted for  $\partial x$  to account for the conduction path increase.

The fully expanded first term is

$$\frac{\partial}{\partial \theta}(\rho h A)_x = \rho h \left( \frac{\partial A}{\partial \theta} \right)_x + A \left[ \frac{\rho_p h_p - \rho_c h_c}{\rho_p - \rho_c} \left( \frac{\partial \rho}{\partial \theta} \right)_x + \rho C_p \left( \frac{\partial T}{\partial \theta} \right)_x \right] . \quad (55)$$

The second term in Equation (54) does not require additional manipulation. The third term must be modified and transformed resulting in the fully expanded form

$$\dot{S} \frac{\partial}{\partial x}(\rho h A)_\theta = \rho h \frac{\partial A}{\partial \theta}_x + \dot{S} A \frac{\partial}{\partial x}(\rho h)_\theta . \quad (56)$$

The expanded final term in Equation (54) is

$$\frac{\partial}{\partial x} \left( \dot{m}_g h_g \right)_\theta = \dot{m}_g \frac{\partial h_g}{\partial x}_\theta + h_g A \frac{\partial \rho}{\partial \theta}_y . \quad (57)$$

Taking Equations (55), (56), and (57) and substituting into Equation (54) provides

$$\begin{aligned} \rho C_p \frac{\partial T}{\partial \theta}_x &= \frac{1}{A} \frac{\partial}{\partial x} \left( k A \frac{\partial T}{\partial x} \right)_\theta - \bar{h} \frac{\partial \rho}{\partial \theta}_x + \dot{S} \frac{\partial}{\partial x}(\rho h)_\theta \\ &\quad + \frac{\dot{m}}{A} \frac{\partial h_g}{\partial x}_\theta + h_g \frac{\partial \rho}{\partial \theta}_y , \end{aligned} \quad (58)$$

where

$$\bar{h} = \frac{\rho_p h_p - \rho_c h_c}{\rho_p - \rho_c} \quad (59)$$

Equation (58) represents the sensible energy, net conduction, net chemical, and net convection occurring within the charring material.

Further simplifying Equation (58) for numerical treatment, the resulting expression is

$$\rho C_p \frac{\partial T}{\partial \theta} \bigg|_x = \frac{1}{A} \frac{\partial}{\partial x} \left( kA \frac{\partial T}{\partial x} \right)_{\theta} + (h_g - \bar{h}) \frac{\partial \rho}{\partial \theta} \bigg|_y + \dot{S} \rho C_p \frac{\partial T}{\partial x} \bigg|_{\theta} + \frac{\dot{m}}{A} \frac{\partial h_g}{\partial x} \bigg|_{\theta} \quad (60)$$

#### d. Finite Difference Formulations

A more detailed discussion of the finite difference formulations is provided in Appendix A based on the work by Moyer et al. [40]. Only the pertinent expressions are provided in the following. The specific locations where the intumescence model is incorporated is limited to the thermal solution and will be identified in the finite difference formulation for the energy equation.

##### (1) Mass Conservation Equation

- In-depth nodes

To better define the density gradients during thermochemical decomposition, it is necessary to incorporate a refined mesh between thermal nodes. This is accomplished through the use of “nodelets” which are evenly spaced between thermal nodes and are specifically utilized for the decomposition gradient calculations. The resulting gradients are then averaged over the volume and applied as a single density and decomposition rate for the energy balance.

##### (2) Decomposition Nodelet Density Change Rate

$$\frac{\rho'_{n,j} - \rho_{n,j}}{\Delta \theta} = \dot{S} \frac{\rho_{n,j+1} - \rho_{n,1}}{\delta_{n,j}} + \left( \frac{\partial \rho_{n,j}}{\partial \theta} \right)_d \quad (61)$$

##### (3) Thermal Solution for Nodelet Temperatures

$$T_{n,j} = T_{n-1} + \frac{T_n - T_{n-1}}{\frac{1}{2}(A_n \delta + A_{n-1} \delta_{n-1})} \left[ \frac{(A_{n-1} \delta_{n-1})}{2} + (j - 0.5) \frac{A_n \delta_n}{J} \right] \text{ for } j \leq J/2 \quad (62)$$

$$T_{n,j} = T_n + \frac{T_{n+1} - T_n}{\frac{1}{2}(A_{n+1}\delta_{n+1} + A_n\delta_n)} \left[ \frac{(j-0.5)}{J} - 0.5 \right] A_n \delta_n \quad \text{for } j > J/2 \quad (63)$$

(4) Nodelet Density Change Rate of Constituent i

$$\left( \frac{\partial \rho_{i,n,j}}{\partial \theta} \right)_D = -P_{F_i} e^{\frac{-E_i}{RT_{n,j}}} \rho_{o_i} \left( \frac{\rho_{i,n,j} - \rho_{r_i}}{\rho_{o_i}} \right)^{m_i} \quad (64)$$

$$\begin{aligned} \left( \frac{\partial \rho_{i,n,j}}{\partial \theta} \right)_D &= \left( \frac{\rho'_{i,n,j} - \rho_{i,n,j}}{\Delta \theta} \right)_y = \\ &= \frac{\rho_{r_i} - \rho_{i,n,j} + \left[ \left( \rho_{i,n,j} - \rho_{r_i} \right)^{(1-m_i)} - \frac{1-m_i}{\rho_{o_i}^{(m_i-1)}} P_{F_i} e^{\frac{-E_i}{RT_{n,j}}} \Delta \theta \right]^{\left( \frac{1}{1-m_i} \right)}}{\Delta \theta} \quad \text{for } m_i \neq 1 \end{aligned} \quad (65)$$

$$\left( \frac{\partial \rho_{i,n,j}}{\partial \theta} \right)_D = \left( \frac{\rho_{i,n,j} - \rho_{r_i}}{\Delta \theta} \right) \left[ \exp \left( -P_{F_i} e^{\frac{-E_i}{RT_{n,j}}} \Delta \theta \right) - 1 \right] \quad \text{for } m_i = 1 \quad (66)$$

$$\frac{\rho'_n - \rho_n}{\Delta \theta} = \dot{S} \frac{\rho_{n+1,1} - \rho_{n,1}}{\delta_n} + \frac{1}{J} \sum \left( \frac{\partial \rho_{n,j}}{\partial \theta} \right)_d \quad (67)$$

- Surface node

The surface node is treated as a half node centered within the volume using the above expressions and assigning half as many nodelets.

- Last ablating node

The last ablating node requires special treatment due to the variation of stationary and moving coordinate systems from the front to the back of the node. Remembering that erosion/ablation from the surface is accounted for at the back node, the back surface of the last node is considered stationary and the front of the node is removed. As a result, the ablation contribution must take the form of

$$\left. \frac{\partial y}{\partial \theta} \right)_{x,j} = \dot{S} \frac{J-j}{J} \quad (1 < j < J) \quad . \quad (68)$$

The resulting modified mass balance for the last ablating node is

$$\frac{d\rho_{N,j}}{d\theta} = \frac{1}{J} \sum_{j=1}^J \left( \frac{\partial \rho_{N,j}}{\partial \theta} \right)_d + \frac{\dot{S}}{\delta_N} (\rho_N - \rho_{N,1}) \quad (69)$$

### (5) Energy Equation

- In-depth nodes

The intumescence model contribution to CMA is incorporated in the energy balance equations through the increase in node thickness  $\delta_n$ . As discussed earlier, the instantaneous intumescence,  $\mathcal{A}$ , of the node thickness is defined as a function of char state and heating rate and is used to evaluate the thermal gradients through the material. The resulting gradients are then used on the next decomposition gradient calculation to define the “new” densities as a result of the increased conduction path length.

The following discusses the development of the energy equation finite difference expressions. Since enthalpy is a function of temperature and density only, it is acceptable to solve Equation (60) in two steps. The first step is to solve the density change for a constant temperature followed by solving the temperature field for a constant density. The energy equation solved implicitly in temperature is defined as

$$\begin{aligned} (\rho' \bar{C}_p)_n (T'_n - T_n) &= \frac{\Delta \theta}{\delta_n A'_n} \left( \frac{\frac{T'_{n-1} - T'_n}{\delta_{n-1}/2 + \frac{\delta_n}{k_n A'_n}} - \frac{T'_n - T'_{n+1}}{\frac{\delta_n}{k_n A'_n} + \frac{\delta_{n+1}/2}{k_{n+1} A'_{n+1}}} \right) + \\ &\left\{ \left[ h_{g_n} + \left( \frac{\partial h_g}{\partial T} \right)_n (T'_n - T_n) \right] \left( \frac{\partial \rho_n}{\partial \theta} \right)_d - \bar{h}_n \left( \frac{\Delta \rho}{\Delta \theta} \right)_n + \right. \\ &\frac{\dot{m}_{g_n}}{A'_n} \left[ h_{g_{n+1}} + \left( \frac{\partial h_g}{\partial T} \right)_{n+1} (T'_{n+1} - T_{n+1}) - h_{g_n} - \left( \frac{\partial h_g}{\partial T} \right)_n (T'_n - T_n) \right] \\ &\left. \frac{\dot{S}}{\delta_n} \left[ (\rho h)_{n+1,1} + (\rho C_p)_{n+1,1} (T'_{n+1} - T_{n+1}) - (\rho h)_{n,1} - (\rho C_p)_{n,1} (T'_n - T_n) \right] \right\} \Delta \theta, \end{aligned} \quad (70)$$

where primed values are taken at

$$\theta' = \theta + \Delta\theta \quad . \quad (71)$$

The specific terms modified as a function of intumescence can be seen in the first term on the right hand side of Equation (70). The instantaneous conduction path is defined by  $\delta_n$  as is the specific term represented by  $\partial L$ .

- Surface Node

$$\begin{aligned} (\rho' \bar{C}_p)_1 (T'_1 - T_1) &= \frac{\Delta\theta}{\delta_1 A'_1} \left( q_{cond} - \frac{T'_1 - T'_2}{\frac{\delta_1}{k_1 A'_1} + \frac{\delta_2/2}{k_2 A'_2}} \right) + \\ \Delta\theta \left\{ \left[ h_{g_1} + \left( \frac{\partial h_g}{\partial T} \right)_1 (T'_1 - T_1) \right] \left( \frac{\partial \rho_1}{\partial \theta} \right)_d - \bar{h}_1 \left( \frac{\Delta\rho}{\Delta\theta} \right)_1 + \right. \\ \left. \frac{\dot{m}_{g_1}}{A'_1} \frac{\left[ h_{g_2} + \left( \frac{\partial h_g}{\partial T} \right)_2 (T'_2 - T_1) - h_{g_1} - \left( \frac{\partial h_g}{\partial T} \right)_2 (T'_1 - T_1) \right]}{\delta_1} + \right. \\ \left. \frac{\dot{S}}{\delta_1} \left[ (\rho h)_{2,1} + (\rho C_p)_{2,1} (T'_2 - T_2) - (\rho h)_1 - (\rho C_p)_1 (T'_1 - T_1) \right] \right\} \end{aligned} \quad (72)$$

- Last Ablating Node

$$\begin{aligned} (\rho' \bar{C}_p)_n (T'_n - T_n) &= \frac{2\Delta\theta}{\delta_n A'_n} \left( \frac{T'_{n-1} - T'_n}{\frac{\delta_{n-1}}{k_{n-1} A'_{n-1}} + \frac{\delta_n}{k_n A'_n}} - \frac{T'_n - T'_{n+1}}{\frac{\delta_n}{k_n A'_n} + \frac{\delta_{n+1}}{k_{n+1} A'_{n+1}}} \right) + \\ \Delta\theta \left\{ \left[ h_{g_n} + \left( \frac{\partial h_g}{\partial T} \right)_n (T'_n - T_n) \right] \left( \frac{\partial \rho_n}{\partial \theta} \right)_d \right\} - \bar{h}_n (\Delta\rho)_n + \\ \frac{\dot{S} \Delta\theta}{\delta_n} \left[ (\rho h)_n + (\rho C_p)_n (T'_n - T_n) - (\rho h)_{n,1} - (\rho C_p)_{n,1} (T'_n - T_n) \right] \end{aligned} \quad (73)$$

## 5. Computer Code Parameters

The CMA mathematical model is based on the previous derivations and assumptions for simulating thermochemical ablation heatshield materials. The following is a brief discussion of input parameters for the CMA code. CMA considers thermal effects due to convection-radiation heating with coupled mass transfer, using a transfer coefficient approach, including the effects of unequal heat and mass transfer coefficients and unequal diffusion coefficients. The processes considered in this code are the same as those shown in Figure 2. The in-depth energy balance used in CMA is provided in Equation (74) and is further discussed in the CMA manual.

$$\rho C_p \frac{\partial T}{\partial \theta} \Big|_x = \frac{1}{A} \frac{\partial}{\partial x} \left( k A \frac{\partial T}{\partial x} \Big|_\theta \right) + (H_g - \bar{h}) \frac{\partial \rho}{\partial \theta} \Big|_y + \dot{\rho} C_p \frac{\partial T}{\partial x} \Big|_\theta + \frac{\dot{m}}{A} \frac{\partial H_g}{\partial x} \Big|_\theta, \quad (74)$$

where  $\bar{h}$  is the weighted mean enthalpy between the char and virgin material enthalpies. The specific heat and thermal conductivity are input as functions of temperature for the virgin and charred materials. The pyrolysis layer thermal properties are determined with a special mixing rule:

$$C_p = F_w C_{p_v} + (1 - F_w) C_{p_c} \quad (75)$$

$$k = F_w k_v + (1 - F_w) k_c, \quad (76)$$

assuming that the pyrolysis layer is a simple mixture of pure virgin and pure char material. The variable " $F_w$ " is defined as a function of the decomposition:

$$F_w = \frac{\rho_v}{\rho_v - \rho_c} \left( 1 - \frac{\rho_c}{\rho} \right), \quad (77)$$

which is considered a weighting factor. The subscripts "v" and "c" refer to the virgin and char material, respectively.

The boundary condition option in CMA used for this investigation is the general convective heating and thermochemical erosion option using the following surface energy balance:

$$q_{sens} + q_{chem} + q_{rad_{in}} - q_{rad_{out}} - q_{cond} = 0 \quad (78)$$



or more specifically

$$\rho_e u_e C_H (H_r - H_{e_w}) + \rho_e u_e C_M [\sum (Z_{ie}^* - Z_{iw}^*) H_i^{T_w} - B' H_w] + \dot{m} H_c + \dot{m} H_g + \alpha_w q_{rad} - F \sigma \varepsilon_w T_w^4 - q_{cond} = 0 \quad . \quad (79)$$

Noting that the subscripts “e” and “w” represent the conditions at the boundary layer edge and wall, respectively,  $Z^*$  difference is the transport of chemical energy associated with chemical reactions at the wall and in the boundary layer,  $F$  is the radiation view factor, and

$$B' = B'_g + B'_c, \quad (80)$$

where  $B'$  is the summation of pyrolysis gas and char mass normalized by the freestream mass transfer rate. The pyrolysis gas normalized ablation rate is determined using

$$B'_g = \frac{\dot{m}_g}{\rho_e u_e C_M} \quad . \quad (81)$$

The char normalized ablation rate using a similar relationship is

$$B'_c = \frac{\dot{m}_c}{\rho_e u_e C_M} \quad . \quad (82)$$

The normalized ablation rates are determined using boundary layer edge conditions of density, velocity, and the mass transfer coefficient along with the pyrolysis gas and char removal rates. The following relationships are used to determine the normalized heat and mass transfer coefficients:

$$C_M = Le^{\frac{2}{3}} C_H \quad , \quad (83)$$

where  $Le$  is the Lewis number and is defined as

$$Le = \frac{Pr}{Sc} \quad (84)$$

and

$$C_H = \frac{h}{C_p \rho_e u_e} \quad . \quad (85)$$

As can be observed in the numerical model, a significantly more complex system of equations is required, as compared to the simplified heat of ablation model, to account for thermal decomposition and chemical reactions during aerodynamic heating of thermal protection systems. It is obvious that the required inputs must be accurately characterized to provide sufficient accuracy in predictions.

### C. Simplified Heat of Ablation Model

To obtain an appreciation of the complexity of the actual ablation phenomena and the commonly used simplifications, a brief discussion of the sublimer and simplified heat of ablation models is presented. Assuming the material behaves as a true subliming material, a simplification to the complex charring material model can be performed. In the subliming material model, several terms drop from Equation (46) and solving for  $\rho \dot{s}$ , the resulting relationship can be obtained:

$$\rho \dot{s} = \frac{q_{conv}(\theta) - q_{rad}(\theta)}{H_v + \eta(H_r - H_w) + C_p(T_w - T_o)} \quad (86)$$

By letting

$$H_a = H_v + \eta(H_r - H_w) + C_p(T_w - T_o) \quad (87)$$

the definition for effective heat of ablation is developed for a subliming, melting, or vaporizing material. It can be seen in Equations (86) and (87) that the effective heat of ablation for a subliming material contains several terms requiring an understanding of the reaction phenomena that can be difficult to obtain or measure. However, if, for a truly subliming material, the reaction phenomena can be fairly well quantified, the heat of ablation model can provide relatively good approximations of in-depth temperature response and ablation behavior.

If the sublimer model approach is used for modeling a charring ablator, it must incorporate several non-linear terms as well as indirectly account for in-depth decomposition of the material for conduction purposes. Since no attempt is made to specifically model these effects, some question of the accuracy in predicting ablation and in-depth temperature profiles arises. Variations in decomposition rate, thermal properties as a function of density, ablation rate, pyrolysis gas composition, and thermochemical reaction all affect the heat of ablation parameter for a given thermal environment.

An additional simplification commonly used in heatshield design is an over-simplified sublimation model similar to Equations (86) and (87) but without the radiation, latent heat, sensible, or blowing terms specifically modeled. The resulting equation represents the simplified heat of ablation considered as a measure of the ability of an ablative material to absorb, block, and dissipate heat per unit mass ablated presented by Rohsenow et al. [41], and is expressed as

$$H_a = \frac{q_c}{\dot{m}} = \frac{q_c}{\rho \dot{s}} \quad , \quad (88)$$

where  $q_c$  is the convective heat flux to a non ablating surface at the ablation temperature,  $\dot{m}$  is the mass ablation rate of the material. Expanding Equation (88) for application to test data and integrating over the period in which ablation occurs:

$$H_a = \frac{\int q_c d\theta}{\rho \int \dot{s} d\theta} = \frac{\int h(T_r - T_m) d\theta}{\rho s_T} \quad . \quad (89)$$

By accurately knowing the aerothermal environment and total measured ablation depth, the simplified heat of ablation can be determined for the tested heating environment. While, in practice, this heat of ablation model is usually a sufficient means of obtaining design parameters for a conservative approach and is very simplified in concept, it has several limitations. One limitation, brought out by Rohsenow [42], is the fact that the heat of ablation determined for a particular thermal environment is not necessarily applicable for a different thermal environment (the heat of ablation is a function of heating rate). Any extrapolation to other thermal environments could result in significant errors. This is a result of not modeling the reaction phenomena occurring. In addition, the selection of an ablation temperature is arbitrary and may not represent the actual surface temperature or pyrolysis/virgin material interface temperature used in the conduction model. This can result in overly conservative predictions of thermal protection thicknesses to maintain structure temperatures at acceptable limits. For these reasons, if desired accuracy can be obtained for the required input parameters, attempting to characterize the actual chemical and mechanical processes occurring in the material and modeling the boundary layer interactions may enhance the accuracy of in-depth temperature predictions and provide a means of reducing the thermal protection system weight contribution.

## **IV. DISCUSSION OF EXPERIMENTS**

### **A. Overview**

To develop mathematical models of heatshield material thermodynamic behavior some physical understanding of the phenomena must be gained through experimentation. A significant level of thought must be devoted to identifying the most sensitive parameters of the experimental approach to minimize uncertainty and ensure accurate representation using specific mathematical expressions. Each of the test facilities used to experimentally evaluate material performance represent a broad range of aerothermal environments with the intent of quantifying a variety of material behavior parameters. The three test facilities utilized in this research were the Wright Patterson Air Force Base Laser Hardened Materials Evaluation Laboratory (LHMEL) [43], the NASA Hot Gas Test Facility (HGTF) [44], and the Holloman High Speed Test Track (HHSTT) [45]. The in-depth thermophysical behavior of the intumescent materials was quantified using the real time radiography and embedded thermocouples at the LHMEL facility. The high shear behavior was demonstrated during the HHSTT sled test, and the hypersonic high altitude environment tested at the NASA HGTF. In addition, the resulting experimental data allows for validation of the mathematical models and provides for widest application. The following is a discussion of each of the three test facilities utilized and corresponding experimental efforts to quantify heatshield material thermodynamic behavior. This discussion provides an understanding of the advantages and disadvantages of each test facility and why more than one facility should be used if possible. General experimental parameters of interest include flow velocity and uniformity, altitude simulation, aerodynamic shear, heat transfer coefficient, recovery temperature, heat flux, local pressure, test time, and measurement capability. All test facilities have specific capabilities to either reproduce or simulate some specific flight environment or effect. Significant importance should be placed on identifying the appropriate experimental facility and method to obtain the physical response necessary to quantify the phenomena of interest. For example, if in-depth thermal response of a heatshield material is the desired experimental result, preliminary analyses should be performed to identify the test facility not only having the appropriate aerothermal flow field, but also the time of exposure taking into consideration the effect of time on in-depth decomposition, substrate thermal response, and potential bondline thermal response concerns. For this example, the LHMEL facility provided an opportunity to measure the transient densities and thermocouple responses through the thickness of material. Additionally, the surface movement due to intumescence was captured and quantified through the use of the transient radiography.

### **B. Laser Thermal Testing**

#### **1. Facility Description**

The Wright-Patterson Air Force Base LHMEL is located in Dayton, Ohio. Located at the facility are two carbon dioxide laser systems. LHMEL-1 is a 15-kilowatt continuous wave Electric Discharge Coaxial Laser (EDCL) and the LHMEL-II is a 150-kilowatt continuous wave EDCL. The LHMEL-1 was utilized for this research effort and is shown in Figure 5. As can be seen in this figure, the laser beam is delivered and reflected to the target sample through the use of mirrors. The sample is attached to the holding fixture where the real-time radiography X-ray

head is located. An exhaust system is in place to help evacuate pyrolysis gases during testing. Additionally, the exhaust system ducting is design to also deliver cold-gas supersonic flow over the sample surface. For this test program, the flow gas was used only to help evacuate fumes for most of the tests. One test series was performed using a Mach 0.9 flow. However, the test conditions and mechanical erosion resulted in surface phenomena not readily understood. Therefore, this discussion will be limited to the no-shear test conditions. This test facility provided a means of quantifying the transient intumescence and accompanying material decomposition. Through the use of these measurements and corresponding in-depth thermocouple data, the numerical model of the heatshield thermochemical behavior could be validated.

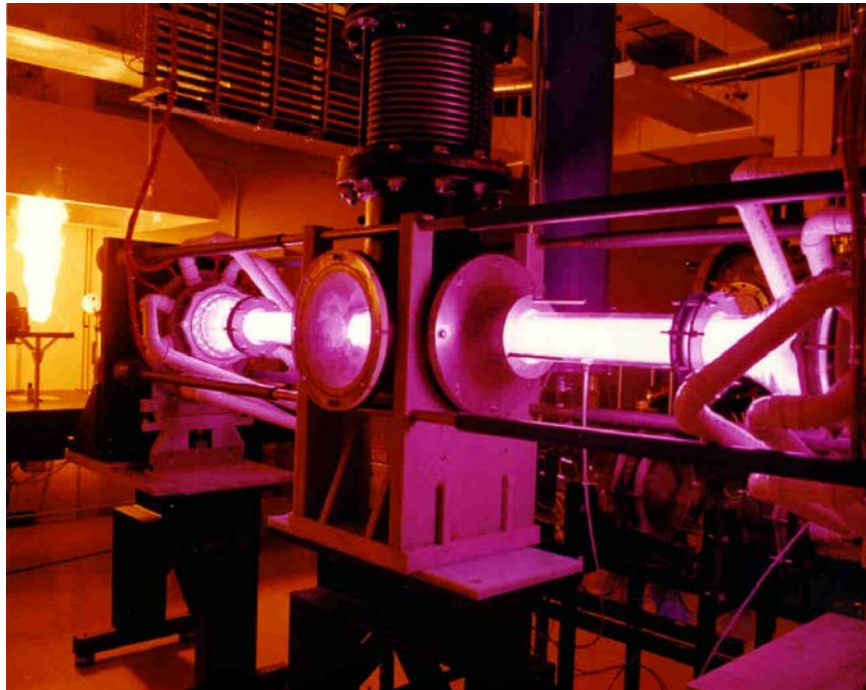


*Figure 5. LHMEF Test Facility*

A summary of some of the advantages for using the LHMEF facility to characterize the heatshield thermochemical behavior and in-depth thermal response include

- a. Constant surface boundary conditions
- b. Decoupling of decomposition and mechanical erosion
- c. Transient radiography for in-depth density measurements as a function of depth and heating rate
- d. Potential to obtain TGA for high heating rates
- e. Samples are subjected to repeatable conditions giving a good indication of relative performance.

The advantages for using the LH MEL facility represent methods of isolating specific thermodynamic events for validating analytic models. The disadvantages simply suggest that other more appropriate aerothermal test facilities should be utilized to quantify the phenomena the LH MEL facility cannot induce such as surface shear.

## 2. Test Setup

The test samples were attached to the holding fixture as shown in Figure 6. The laser beam was split and adjusted to impart the desired heat load on the sample minimizing two-dimensional effects. The radiography head was located above the sample looking down. The thermocouple plug was located in the center of the sample. The thermocouple plug configuration is shown in Figure 7. As can be seen, the wire leads were inserted into the sample at the desired depths and exited along the side of the plug. The leads were brought out the back of the aluminum substrate, strain relieved, and extended sufficiently to reach the Data Acquisition System (DAS). The fixed X-ray measurement plane was selected to be the 0.05-inch thermocouple bead location based on predicted thermal response and expansion.

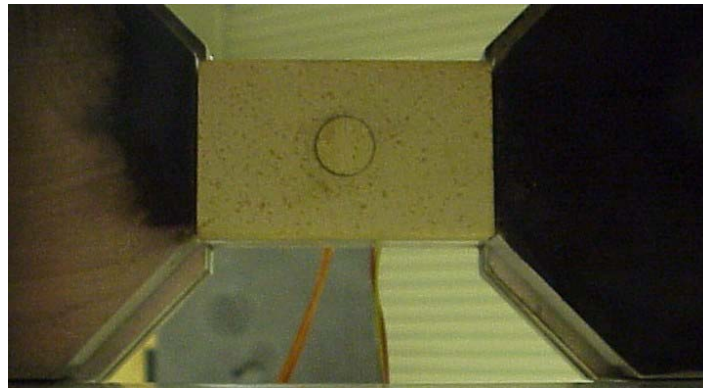


*Figure 6. Assembled Sample Configuration*

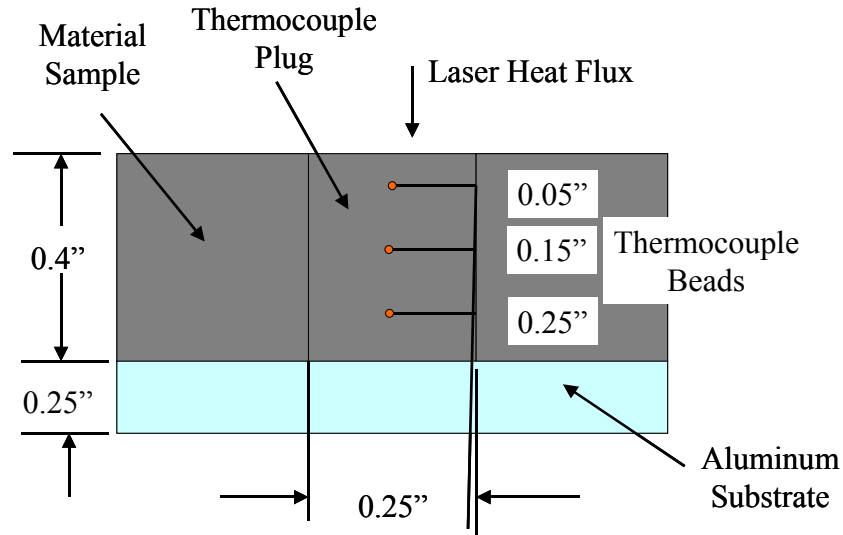


Figure 7. Thermocouple Plug Configuration

### 3. Thermal Environment

Two heat fluxes were imparted to the samples representing Mach 4 and Mach 5 type environments. These heat fluxes were imparted using 22 Btu/ft<sup>2</sup>-s and 66 Btu/ft<sup>2</sup>-sec, respectively, to induce the desired material thermal response. A two-inch diameter beam width was used and minimized two-dimensional conduction effects at the sample edges.

### 4. Experimental Results

The experimental results include in-depth thermocouple responses as well as transient in-depth decomposition and intumescence of the posttest sample. Through the use of real time radiography video, an additional data point was obtained through the tracking of the thermocouple bead motion where intumescence occurred in-depth. This coupled with the transient surface motion provided a means of matching the intumescence rate at various depths in the material. Surface temperature data was not yet available, so only approximate magnitudes are presented. Three samples were tested for each thermal environment. However, only two tests were instrumented with thermocouple plugs. As can be seen in Figure 8 for Test 1 at a heating rate of 22 Btu/ft<sup>2</sup>-hr, the two tests gave very similar thermocouple responses throughout the test period. The 0.05-inch thermocouple response begins to deviate later in the test, but this a probable result of the thermocouple detachment occurring at slightly different times and varying in position more significantly later in the test. It is interesting to note the remaining thermocouple responses agree very well throughout the entire test. Very little variation occurs between test data. At approximately 17 seconds into the heating portion of the test, the 0.05-inch thermocouple reaches approximately 260 °F and appears to detach and drop in temperature. This same behavior is not as obvious for the other test sample. However, some slight change can be observed at approximately 200 °F. It appears that the 0.05-inch thermocouple motion begins due to material intumescence below that depth around the time the material reaches 200 to 260 °F. This results in a drop in temperature measurement. This motion was further validated

through the use of real-time radiography video during which the initiation and continuation of thermocouple bead motion can be clearly observed. The remaining two thermocouples provide smooth data at temperatures below levels for which any significant decomposition occurs. Typical surface temperatures for the 22 Btu/ft<sup>2</sup>-sec (Test 1) reached approximately 2000 °F. Figure 9 provides the in-depth thermocouple response for the 66 Btu/ft<sup>2</sup>-sec laser heating test (Test 2). It can again be observed that an event occurs near the 250 °F temperature level on the 0.05-inch thermocouple position. However, at the higher heating rate this temperature is reached within 10 seconds. The thermocouple event can be clearly observed for both tests in this figure and for the same time and temperature. The two test sample responses agree well throughout the test for all three thermocouple locations. The 0.15-inch and 0.25-inch thermocouples provide smooth data throughout the test. Typical surface temperatures for this test were approximately 2800 °F. Figure 10 provides a view of the post-test material surface response for the 22 Btu/ft<sup>2</sup>-sec laser test. A black, carbonaceous char forms during heating and is retained for these tests due to the lack of significant airflow or shear. The chemical constituents of the various layers of decomposition have not yet been fully quantified. However, based on previous material property measurements [46], the higher decomposition regions consist of silica and carbon with graduated mixtures as the layers become less decomposed. The char developed fissures with and increased surface roughness [47]. The circular region of laser heating can be observed in each of the tests. Some level of two-dimensional effects occurred due to lateral conduction. However, this was judged to be relatively small compared to the in-depth decomposition. While total intumescence was measured after each test, the in-depth decomposition layers were initially quantified by sectioning each sample. Figure 11 provides a magnified view of a typical section where the various decomposition layers can be identified. While this approach provided an approximate method of determining thermal penetration, the primary means of quantifying decomposition will be the digitized real-time radiography. This data has not yet become available but will provide a transient density plot as a function of depth into the material. This will also take into account the intumescent behavior.



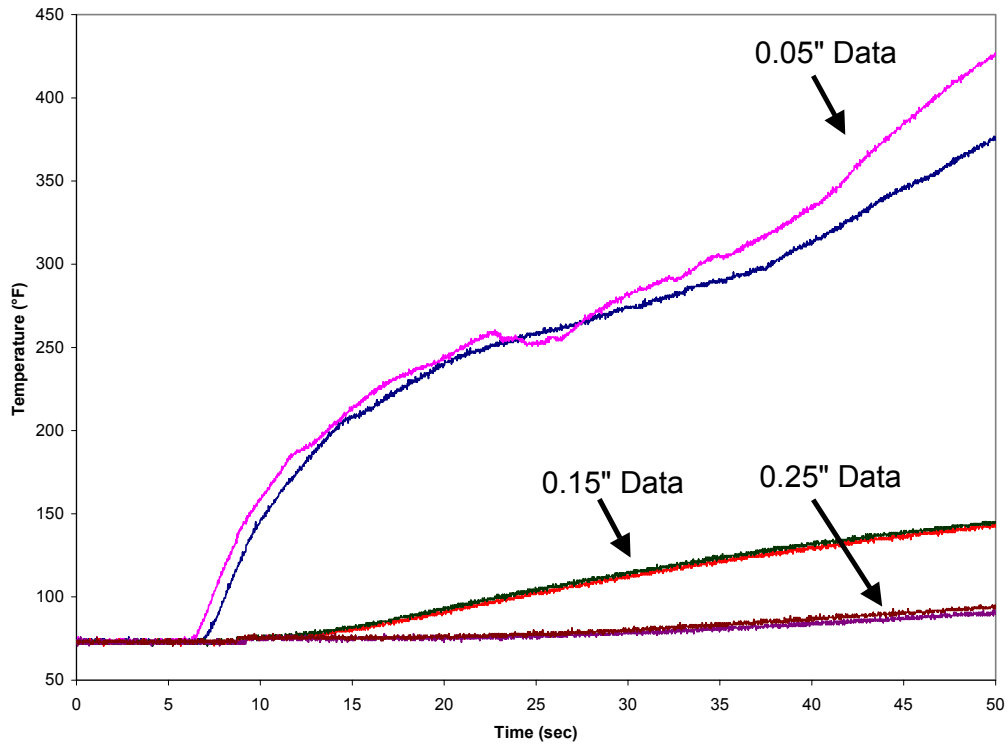


Figure 8. Test 1, 22 Btu/ft<sup>2</sup>-sec Laser Heating Thermal Response

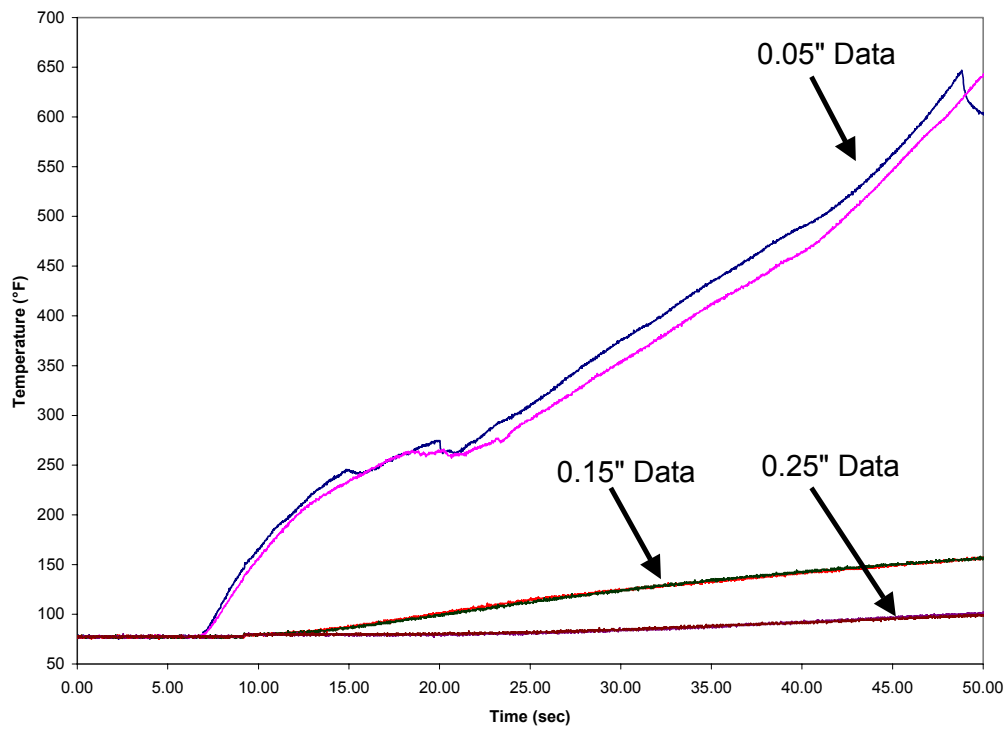
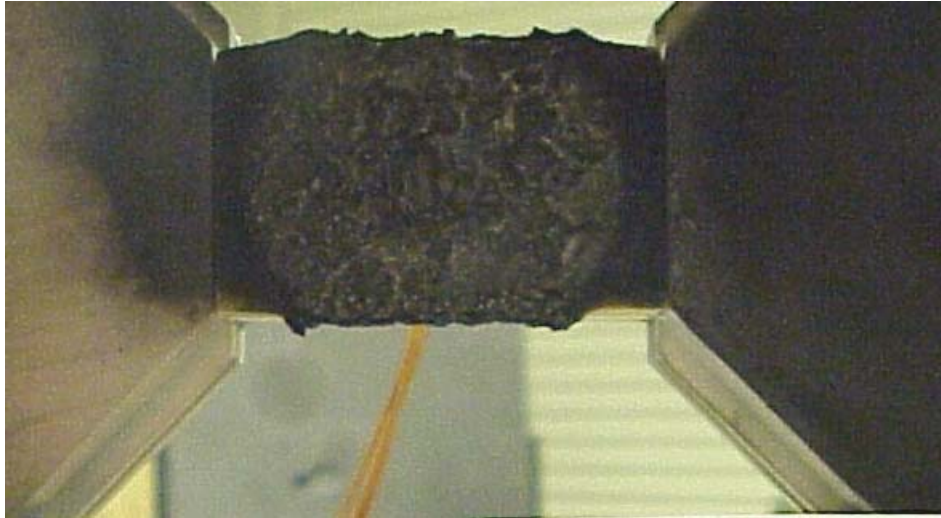


Figure 9. Test 2, 66 Btu/ft<sup>2</sup>-sec Laser Heating Thermocouple Response



*Figure 10. Post-Test Material Response*



*Figure 11. Sectioned View of Material Sample Post-Test*

Typical pre- and post-test measurements are provided in Table 1. The weight measurement was obtained to validate the analytic model decomposition predictions of mass loss and in-depth decomposition. The pre- and post-test thickness measurements provide the total intumescence or swell which can be used in conjunction with the real-time radiography to validate the intumescence analytic model. The lower heating rate Test 1 resulted in approximately one half the total mass loss that the higher heating rate Test 2 induced. However, the total intumescence was very similar for each test.

Table 1. Pre- and Post-Test Measurements

	Test 1			Test 2		
	Pre-test	Post-test	Change	Pre-test	Post-test	Change
Weight (grams)	107.7	106.1	1.6	108.4	105.3	3.2
Thickness (inch)	0.4	0.53	0.13	0.4	0.56	0.16

## 5. Laser Test Summary

The LHME thermal test facility provides a unique method of quantifying in-depth thermophysical and thermochemical behavior of intumescent and decomposing materials. The utilization of real-time radiography ensures the accuracy of analytic model validation. Previous test efforts allowed for only posttest measurements resulting in the lack of rate effects. Additionally, the embedded thermocouples provide a significant capability in accurately obtaining the thermal penetration and corresponding decomposition state. Use of these measurements also allows for the determination of more accurate thermal properties. It is generally very difficult to obtain thermal conductivity and specific heat of the various pyrolyzing and charring regions as a function of temperature. Through the use of the radiography and embedded thermocouples, the properties of each of these regions can be better quantified.

## C. NASA Hot Gas Test Facility Aerothermal Testing

### 1. Facility Description

The NASA MSFC-HGTF [48] located at Redstone Arsenal, Alabama, was developed for thermal test and evaluation of launch vehicle heatshields and provided a means of obtaining charring heatshield material thermal response in a low-shear hypersonic aerothermal environment. This test facility was used to experimentally evaluate candidate heatshield material performance in hypersonic high altitude environments [49]. This environment completes the range of shear and heating rate when coupled with the two previously discussed aerothermal environments. The sled test results in a high shear with the T-Range having a moderate to low shear rate and the HGTF delivering a very low shear level.

The HGTF is a combustion driven supersonic wind tunnel that burns a lean mixture of hydrogen and air. The combustion products are expanded from the combustion chamber through a two-dimensional contoured nozzle into a 16 x 16 inch test section with a nominal flow velocity of Mach 4. The flow then passes through an axisymmetric diffuser and is exhausted to the atmosphere. The tunnel is aided by an annular nitrogen ejector which pumps the tunnel to a pressure of about 1.0 psia before tunnel ignition. A photograph of the test facility is provided in Figure 12. This figure shows the aft end of the 20-foot subsonic diffuser section. The test cell is located forward under the tent-like structure and consists of a rectangular test section with an optical window on top for surface temperature measurement and radiant heat lamp devices. Openings on the sides at the test cell allow for test article placement.



*Figure 12. NASA Marshall Space Flight Center Hot Gas Aerothermal Test Facility*

## 2. Test Configuration

The test configuration is shown in Figure 13 with the six test panels visible prior to final positioning. Each test panel contained approximately 0.3-inch heatshield applied to a 0.05-inch 304 stainless steel substrate. Each panel was instrumented with five thermocouples spot-welded to the back surface of the substrate as shown in Figure 14. The panels were 0.05-inch 304 stainless steel substrate. Each panel was instrumented with five thermocouples 0.05-inch 304 stainless steel substrate. Each panel was instrumented with five thermocouples spot-welded to the back surface of the substrate as shown in Figure 14. The panels were mounted to a single support frame and hydraulically raised into the test cavity so as to maintain flush surfaces with the tunnel wall. Silica phenolic spacers were positioned in front and back of each heatshield sample to minimize leading edge effects due to shape change and ablation. Each material was alternated between front and rear positions to obtain sensitivities due to location in the test chamber. Mach 6 and Mach 8 aerodynamic flow was delivered over the test panels and transient surface and backside thermal response recorded. The thin skin calibration panel is shown in Figure 15. Two thin skin thicknesses, 0.1-inch and 0.06-inch, were used and front and



rear position sensitivity assessed. Analytic predictions of thin skin thermal response were correlated with temperature measurements. These results were then compared with heat flux gage measurements obtained during the test. Multiple methods of determining heat flux measurements reduced uncertainty in the accuracy of imparted convective environments.

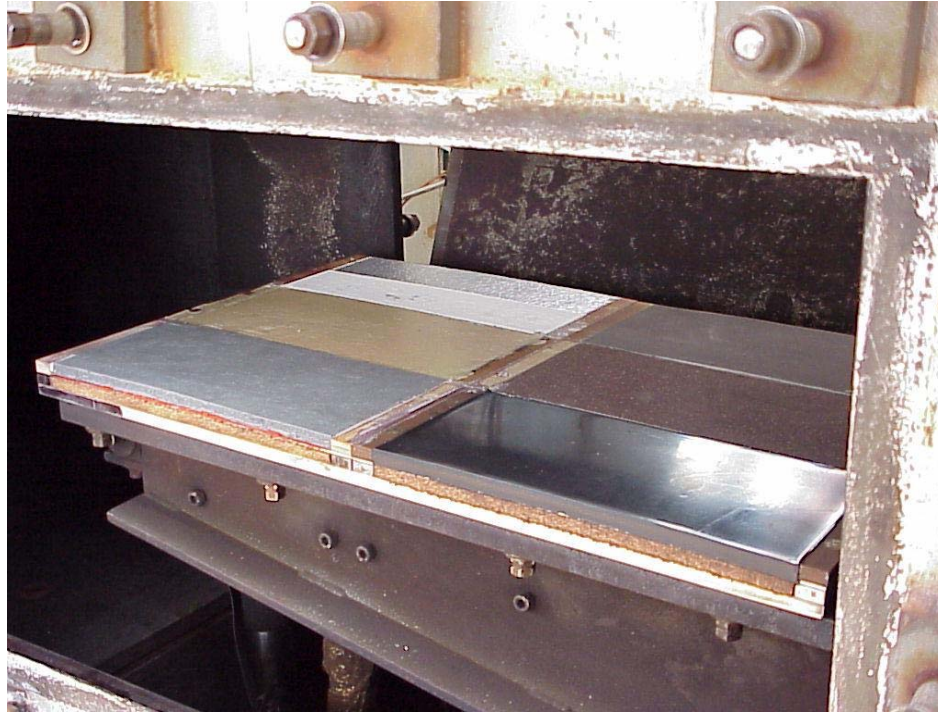


*Figure 13. Test Panel Configuration*

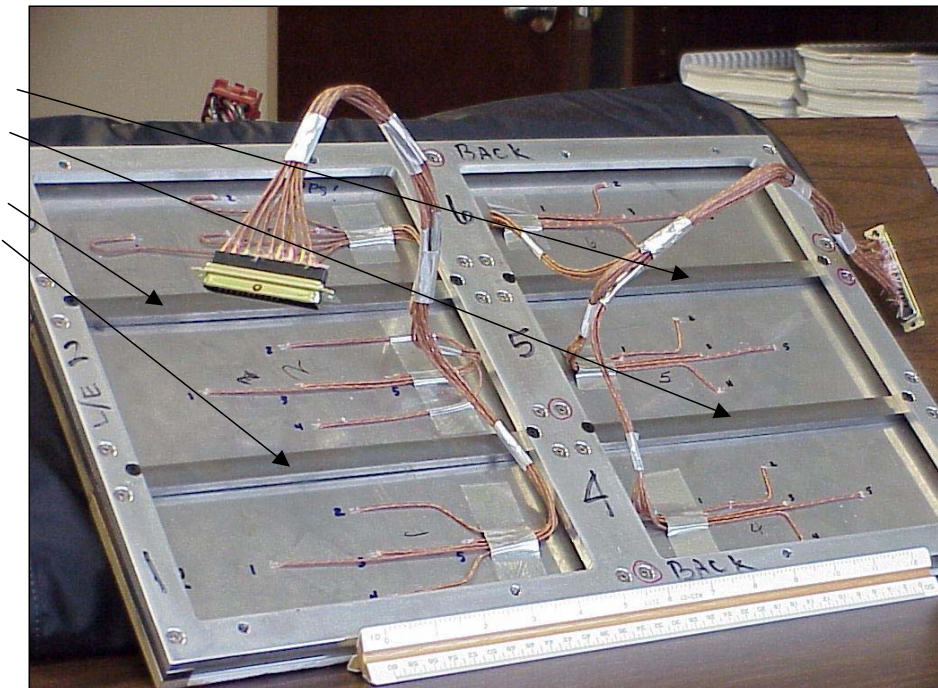


*Figure 14. HGTF Thermocouple Instrumentation*



*Figure 15. HGTF Thin Skin Calibration Panel*

### 3. Thermal Environment

Figures 16 and 17 define the aerothermal environments generated for these tests. Figure 16 provides the heat transfer coefficient, recovery temperature, and resulting cold wall heating rate for the Mach 6 test condition. The actual test time for the Mach 6 condition was 300 seconds. The driving temperature was approximately 2400 °F with a heat transfer coefficient of 10 Btu/ft<sup>2</sup>-hr-°F. The test goal was achieved through inducing a cold wall heating rate of 6 Btu/ft<sup>2</sup>-sec to the heatshield materials. Figure 17 provides the Mach 8 test conditions with a test period of 240 seconds. The reduction in test time was a result of wall temperature limitations for the test cell. The recovery temperature obtained during the test was approximately 2700 °F with a heat transfer coefficient of 11 Btu/ft<sup>2</sup>-hr-°F, slightly more than that achieved for the Mach 6 test condition. The resulting cold wall heating rate was approximately 8 Btu/ft<sup>2</sup>-sec. The local pressure for the test panels was approximately 1.0 psia. The corresponding cold wall shear level is shown in Figure 18 for the two test conditions. As can be seen, a significantly lower shear level was obtained using this test facility and is indicative of the high altitude environment simulation.

These test conditions were verified through the use of both heat flux gages and thin skin calorimetry panels. The analytical results are compared with the thin skin measurements in Figures 19 and 20 for the Mach 6 and Mach 8 test conditions, respectively. The thin skin calorimeter configuration was a 0.06 inch and 0.1 inch thick steel plate with both backside thermocouple and infrared surface temperature measurements collected. Due to the high thermal conductivity and relatively thin calorimetry sections, the backside thermocouple provided a good representation of the surface temperature response. This result was then analytically matched providing the aerothermal boundary conditions for the test environment.

As can be seen, very good agreement was obtained and provided additional confidence in the analytic modeling.

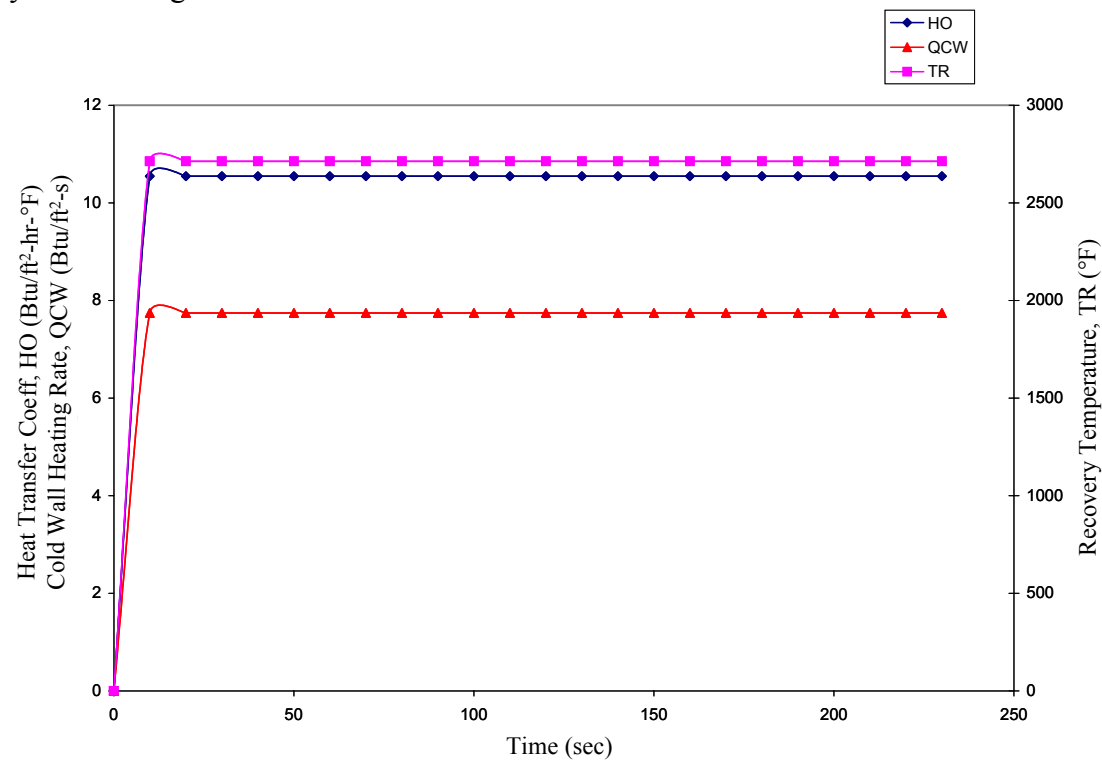


Figure 16. Mach 6 Test Thermal Boundary Conditions

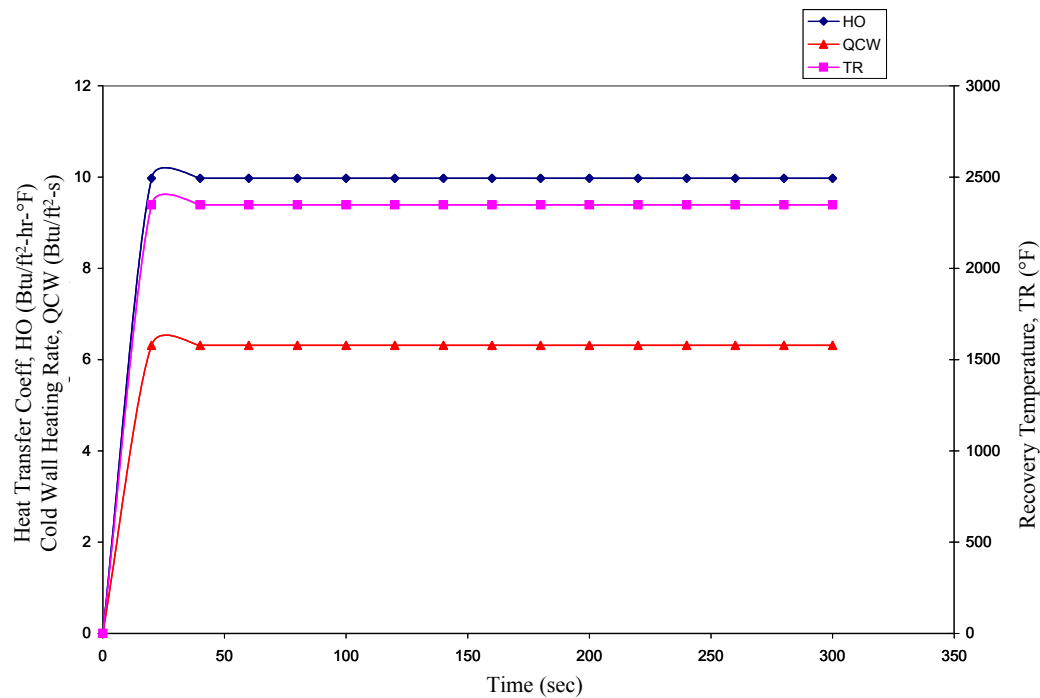


Figure 17. Mach 8 Test Thermal Boundary Conditions

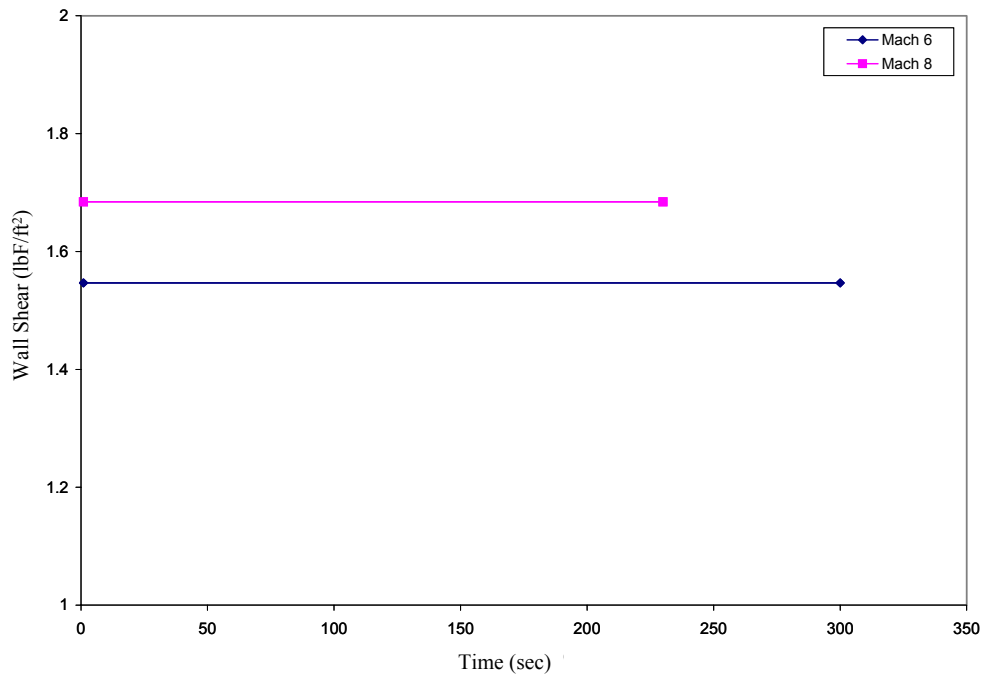


Figure 18. Cold Wall Shear for Mach 6 and Mach 8 Test Conditions

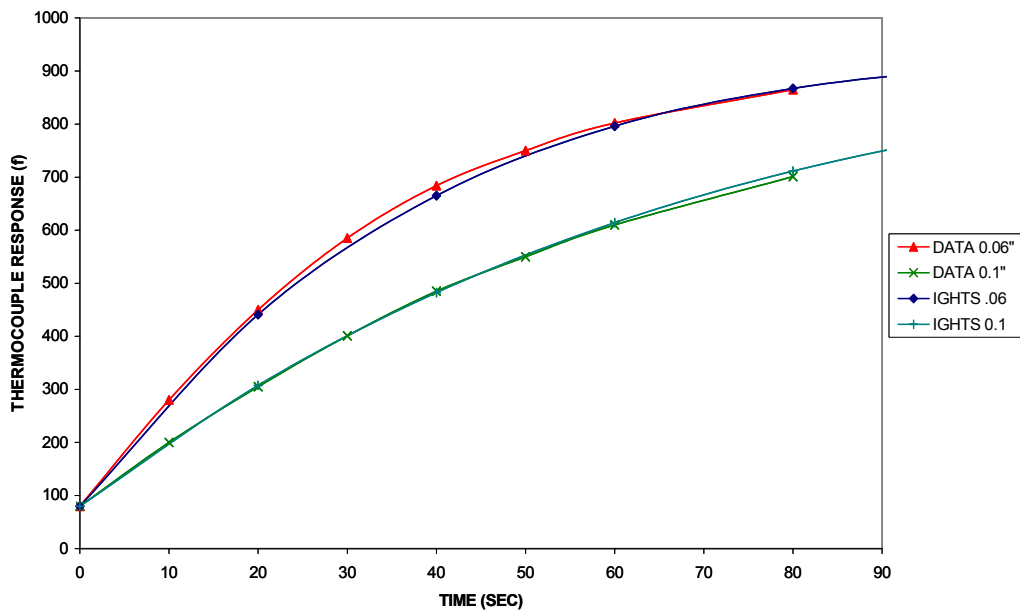
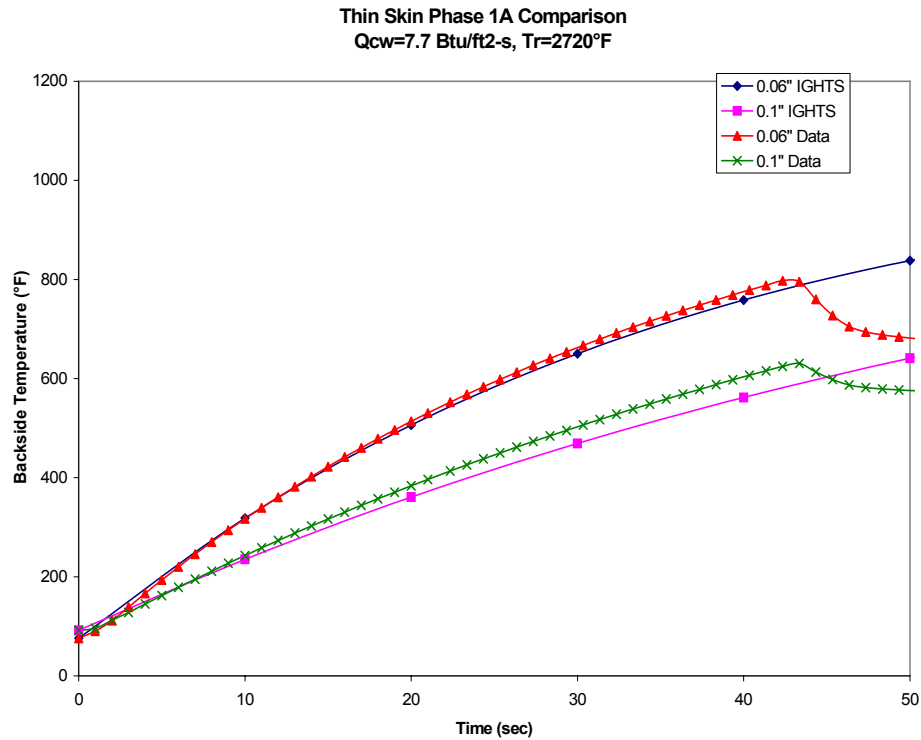


Figure 19. Calibration of Analytic Model for Mach 6 Test





*Figure 20. Calibration of Analytic Model for Mach 8 Test*

#### 4. Experimental Results

The Mach 6 and Mach 8 environments of interest were represented by constant cold wall heat flux values of 6 and  $8.5 \text{ Btu/ft}^2\text{-s}$ , respectively. The total temperatures delivered by the test facility were  $2300^\circ\text{F}$  for the Mach 6 condition and  $3000^\circ\text{F}$  for the Mach 8 condition. The thermal response for the Mach 6 test environment is shown in Figure 21. This figure provides the transient thermal response measured for the surface as well as the backside of the substrate. Also visible is the black carbonaceous char that formed during the test. The surface temperature response reached approximately  $950^\circ\text{F}$  with the average backside thermal response reaching  $160^\circ\text{F}$ .

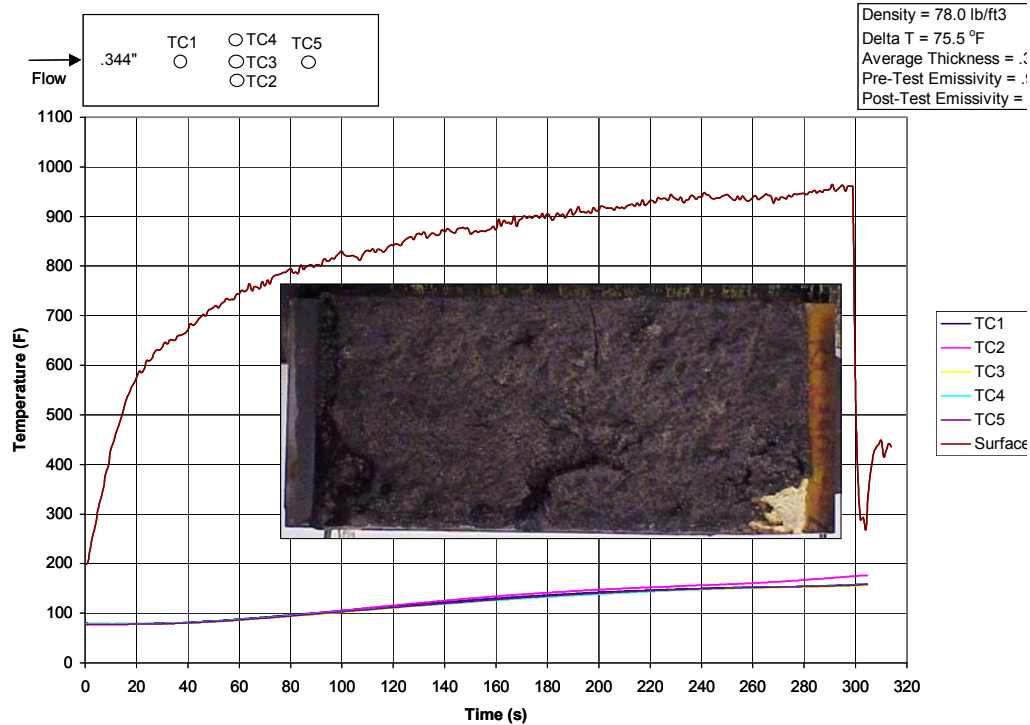
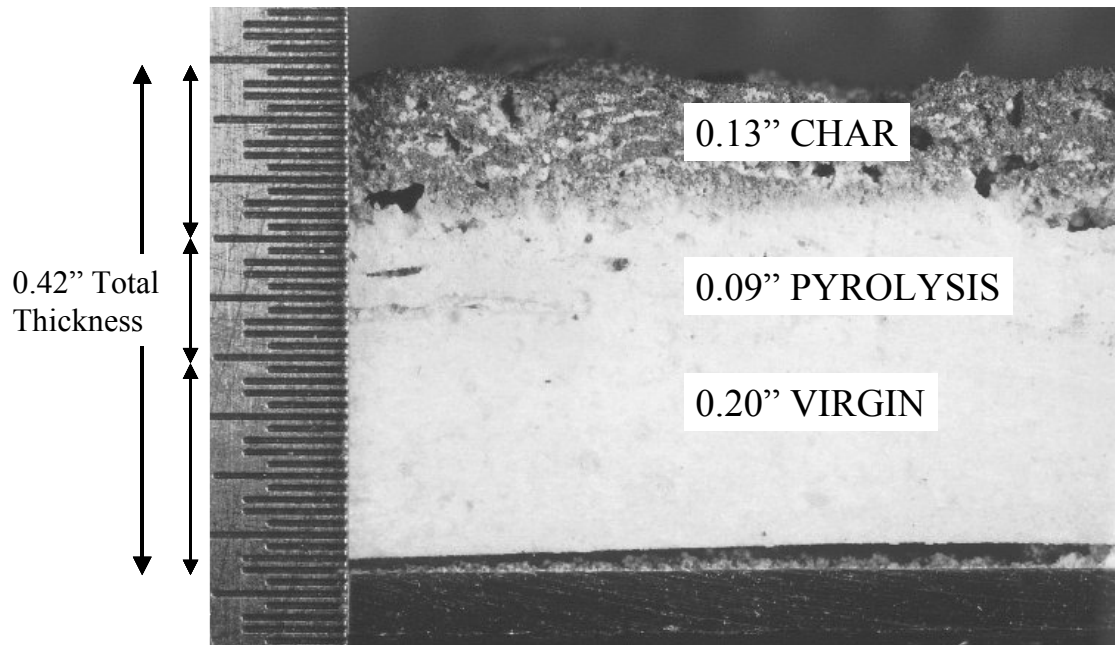


Figure 21. Thermal Response for Mach 6 Test

The resulting in-depth thermochemical decomposition is shown in Figure 22 for the Mach 6 test condition. As can be seen, a significant level of internal decomposition occurred during the test. The material maintained a relatively strong char. Table 2 provides a summary of decomposition as measured after the test. The value of total ablation for the test sample was 0.10 inch. This highly decomposing material provided significant thermal performance in the form of limiting backside temperature rise when compared to low-density, low thermal conductivity materials. It should be noted that where volume constraints are more important than weight constraints, decomposing material performance should be investigated. When weight constraints are equal or more severe than volume constraints, decomposing materials become less attractive. However, simply assuming the need for low-density low thermal conductivity materials can greatly restrict the potential identification of superior heatshield materials.



*Figure 22. Sectioned View of In-depth Decomposition*

Table 2. Ablation Measurements for Mach 6 Test

Measurement	Material
Pretest Thickness	0.3"
Char Depth	0.13"
Pyrolysis Depth	0.09"
Virgin Material Depth	0.2"
Posttest Thickness	0.42"
Intumescence	120%
SHOA Total Ablation	0.1"

## **D. Aerothermal Sled Testing**

### **1. Facility Description**

The HHSTT located at Holloman Air Force Base in Alamogordo, New Mexico has a sled track approximately 10 miles in length running north and south with the ability to achieve 10,000 ft/sec velocities duplicating sea-level hypersonic aerothermal environments. Specifically, hypersonic mechanical shear and high heat flux can be imparted to heatshield materials as well as other missile components of interest. Three specific rails are available two of which (Rail A & B) are roughly 10 miles long with a trough located between the two for water breaking. The third rail (Rail C) is a shorter version located to the east of Rail B and is currently under modification to provide a narrow gage sled vehicle design to minimize dynamics and coupled with Rail B operates as the lethality test section. The lethality test capability allows for the full-scale testing of missile lethality mechanisms up to Mach 10 velocities at sea level. The aerothermal test capability allows for the duplication of hypersonic missile flight in free stream air environments for several seconds. These environments induce the hypersonic free stream shear that plays a significant role in heatshield analysis and design. This level of shear at near sea level conditions cannot be duplicated at any other test facility for the test periods necessary to obtain sufficient ablation minimizing measurement uncertainty.

A summary of some of the advantages for using the sled facility to characterize the ablation performance and in-depth thermal response of heatshield materials include

- a. Well-characterized free-stream air environment
- b. Well-defined velocity and pressure
- c. Flow occurs over a simple, symmetrical geometry for which local flow values and heating rates can be calculated with confidence
- d. Materials are exposed to environments fully representative of an actual sea level hypersonic missile flight with respect to heating and shear
- e. Samples are subjected to equal conditions giving a good indication of relative performance.

Some of the current disadvantages of using the sled facility are

- a. Sled tests have a highly transient nature
- b. Surface and in-depth temperature cannot easily be obtained from these tests
- c. The test environment is highly dynamic requiring significant isolation systems to ensure data collection and no loss of test samples.

However, current research and development is underway to reduce or eliminate these disadvantages. Sustained velocities along with step function heating and methodologies to instantaneously remove the test samples from heating during the coast phase are being developed. A significant level of effort is underway to utilize embedded thermocouples and surface temperature measurement methodologies to obtain accurate transient temperature measurements through heatshield materials during test. Significant reductions in the dynamic environment have been realized through recent sled facility enhancements.

The sled test aerothermal results [50] were specifically used to obtain material response in a high-shear, low-altitude, supersonic air environment. The altitude at Holloman is approximately 4000 feet providing a good representation of low altitude supersonic flight. The test samples used provide a simple uniform configuration for which correlations have been validated using a significant level of experimental data. This coupled with calorimetry further ensures the accuracy of the aerothermal boundary conditions predicted using the analytical models and adds confidence in quantifying material response subjected to a given environment. While the actual test delivered a transient thermal environment to the samples, the validated analytical tools provide a means of reducing uncertainty in material thermal response predictions for the transient effects.

## 2. Test Setup

A schematic of the seven-arm test sting and rail orientation is provided in Figure 23. The test samples are positioned in front of all sled hardware to induce a uniform free stream air environment. The seven-arm sting is attached to an instrumentation cylinder that is designed to contain and dynamically isolate telemetry hardware as well as additional recording devices. The instrumentation cylinder is attached to the last stage motor. A brake wedge and sled rail slipper hardware constraining and supports the instrumentation cylinder on the rail. The candidate materials were applied to 15-degree sharp-nose cones as shown in Figure 24. A 17-4 stainless steel tip, base, and substrate were coated with 0.25 inches of heatshield material. A 22.5-degree blunt-nose cone Duroid™ sample was used to fill the seventh position (center) on the test-sting and based on the well-characterized material thermal performance [51] provided a means of normalizing the aerothermal environment in the event of anomalies. Figure 25 shows the sample orientation on the seven-arm sting. Figures 26 and 27 provide actual photos of the sled test vehicle and samples, respectively, located on the sled track shortly before the test. As can be seen in Figure 26, the test-sting is attached to a two-stage rocket system with the seven-arm sting cantilevered in front ensuring the material samples will be exposed to an undisturbed free-stream environment. Figure 27 provides a close view of the mounted heatshield samples. The configuration is designed to prevent shock interactions between samples and from the rail. The material of interest for this research is positioned in the lower right location. An alumina hardcoat is applied to the seven-arm sting as short duration thermal and shock attachment protection.

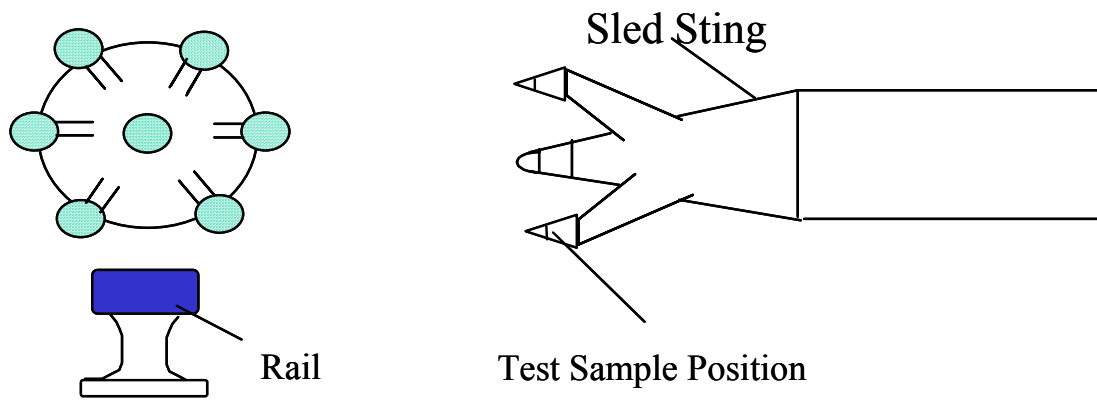


*Figure 23. Sled Test Hardware Configuration*

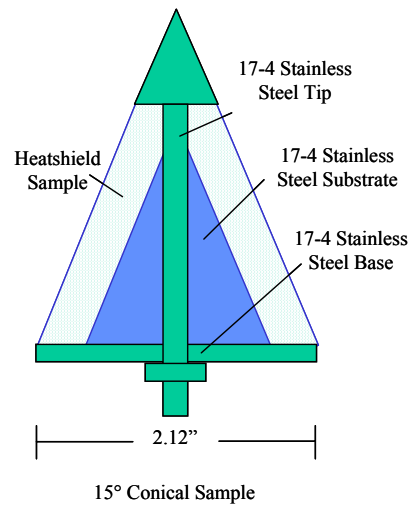


*Figure 24. Sled Test Sample Configuration*

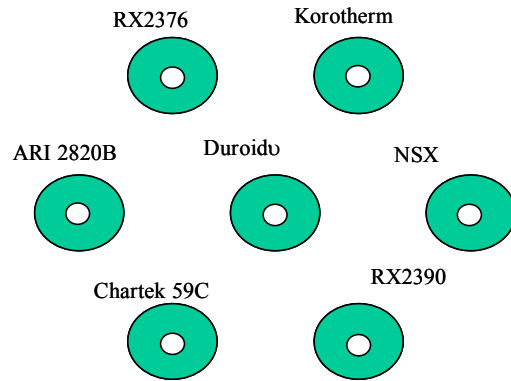


*Figure 25. Material Orientation*

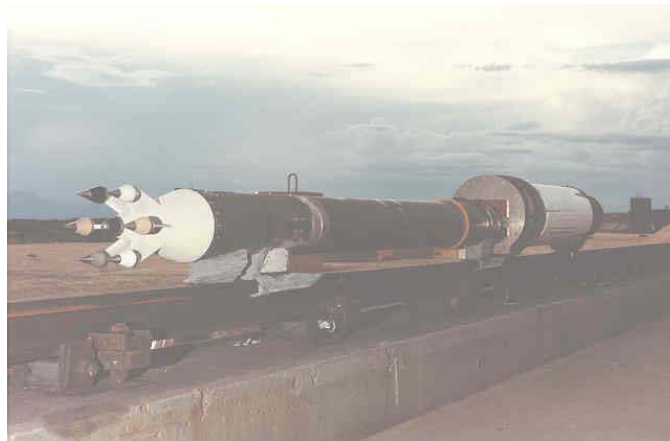


*Figure 26. Sled Vehicle Configuration*

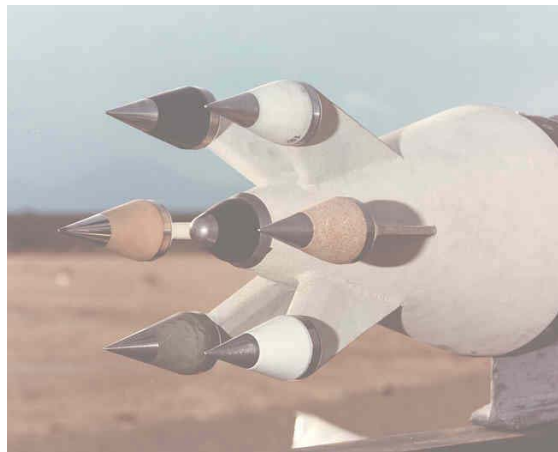


*Figure 27. Sled Test Samples*

### 3. Thermal Environment

The resulting velocity and recovery temperature history for the sled test are provided in Figure 28. A peak velocity of 4950 ft/sec was achieved at 4 seconds with a corresponding recovery temperature of 1723 °F. As previously discussed, the sled environment is a relatively transient condition. However, use of engineering methods and adequate measurements can provide an accurate means of quantifying ablation behavior in high shear environments. With the added instrumentation of embedded thermocouples, sled facilities can provide an accurate means of heatshield aerothermal testing.

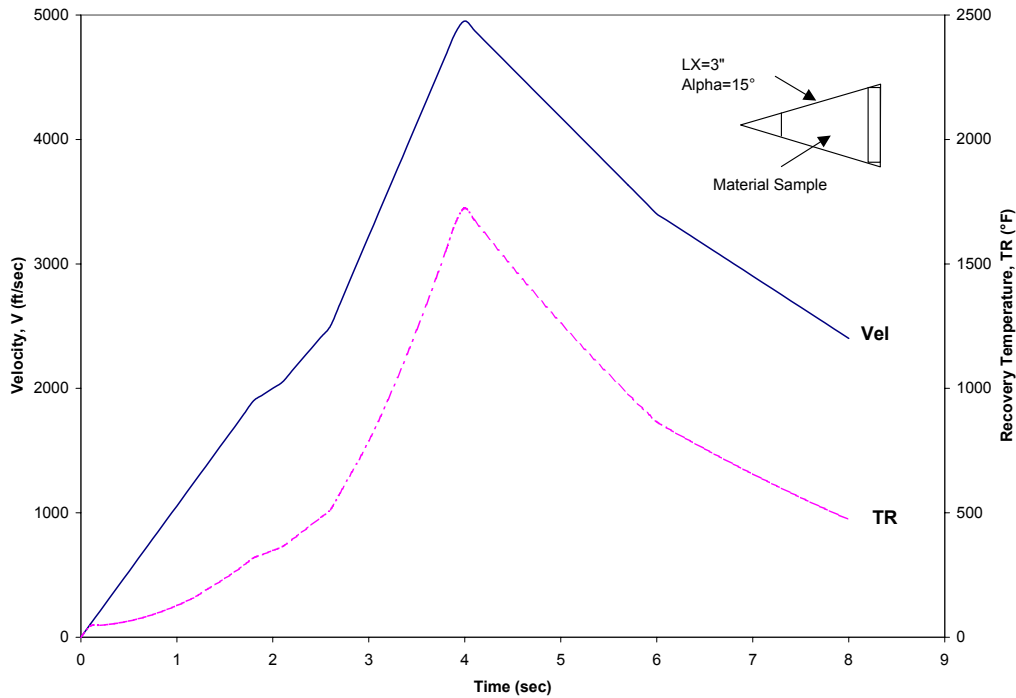


*Figure 28. Sled Velocity and Recovery Temperature History*

Two analytic tools were utilized to define the aerothermal environment as well as quantify ablation performance parameters. The first code, Ideal Gas Heat Transfer to Structures (IGHTS) [52], contains the SHOA methodology for designing heatshields. The Aeroheating and Thermal Analysis Code 3D (ATAC3D) [53] allows for transient real gas aerothermal boundary condition development of hypersonic, non-axisymmetric missile bodies coupled with the more complex thermochemical decomposition material thermal response [54] to which the addition of mechanical shear and intumescence was added and discussed in Section III of this report. Use of the Newtonian methodology in the ATAC3D code showed good agreement with the IGHTS code and the following boundary conditions were analytically defined for the sled test. The cold wall heat transfer coefficient history is shown in Figure 29. As can be seen, a peak value of 935 Btu/ft<sup>2</sup>-hr-°F is reached at 4 seconds. This value coupled with the recovery temperature shown in Figure 28 represent the aerothermal boundary conditions that define the heating rate imparted to the materials. The cold-wall heating rate along with the overall integrated heat is provided in Figure 30. A peak of 450 Btu/ft<sup>2</sup>-sec was achieved with a total integrated heat of 1050 Btu/ft<sup>2</sup>.



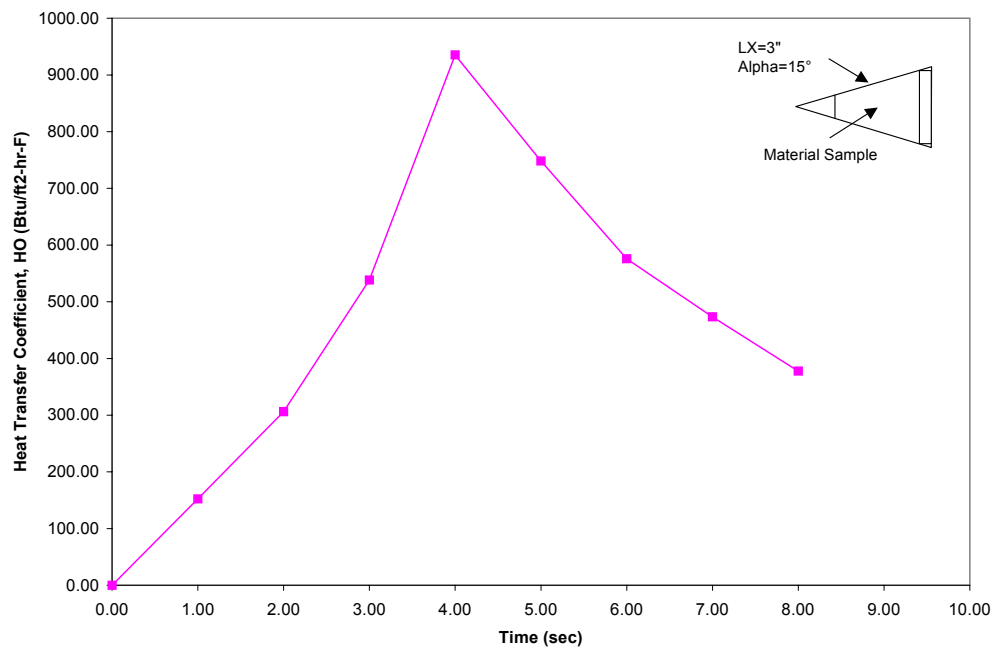


Figure 29. Sled Test Cold Wall Heat Transfer Coefficient

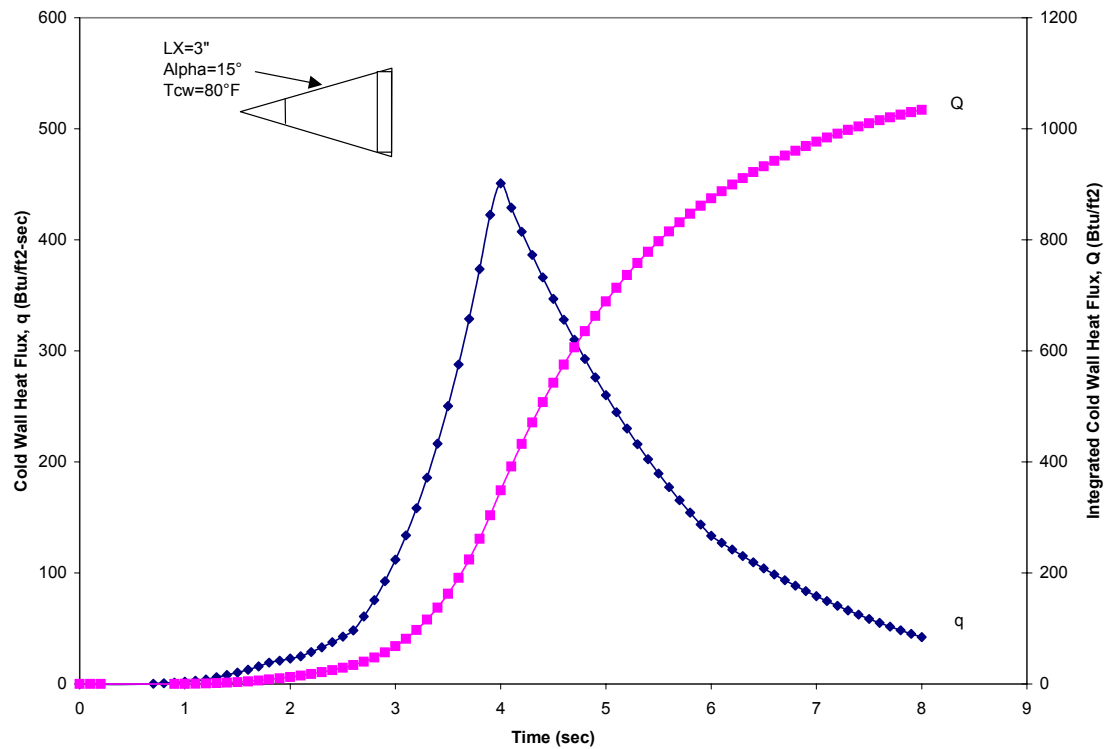
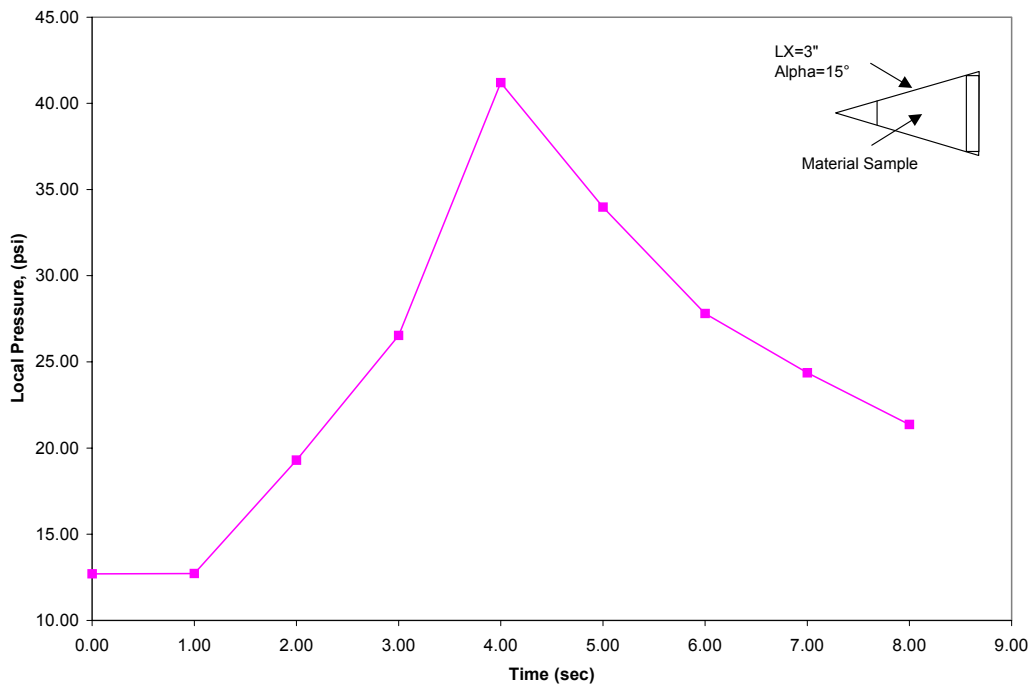
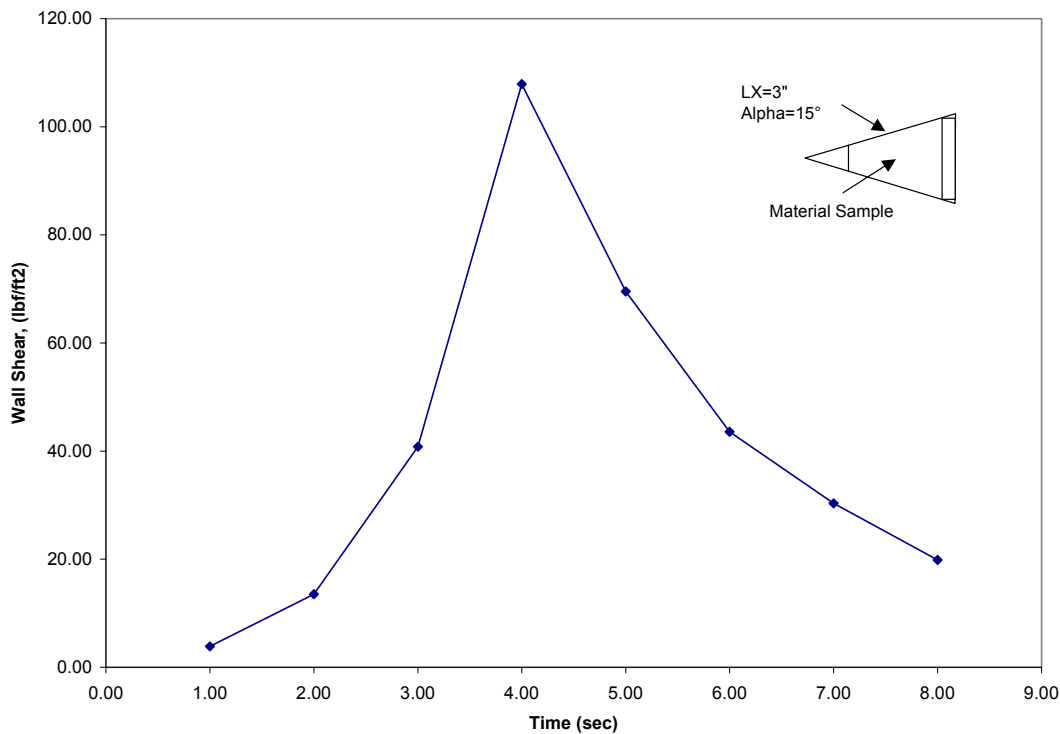


Figure 30. Sled Test Cold Wall Heating Environment

Additional boundary conditions of interest are the local pressure and wall shear along the heatshield surface. Figure 31 provides the local pressure for the 15-degree sharp-nosed cone. A peak local pressure of approximately 41 psia was achieved on the cone. The peak wall shear is approximately 108 lbf/ft<sup>2</sup> and is representative of high-speed sea level flight. While the analytic model development is primarily directed toward intumescence, mechanical shear removal of the charring surface is an additional phenomenon of interest to be investigated in future research efforts. Figure 32 provides the cold wall shear for the geometry of interest. As can be seen, a significant increase in shear is generated for the sled test environment as compared to the high altitude hypersonic environment of the NASA HGTF.



*Figure 31. Sled Test Local Pressure*



*Figure 32. Sled Test Cold Wall Shear*

#### 4. Experimental Results

Figure 33 shows the candidate materials on the sled vehicle during the peak velocity portion of the test. The high-temperature flow visible behind the sled slipper hardware is a result in the frictional interaction between the slipper and rail as well as additional flow field effects. Shock structure is slightly discernable in the seven-arm sting region. Figure 34 provides a view of the test samples after the test was conducted. As can be seen, significant ablation occurred on several material samples. Measurements of ablation depths were principally made with an optical comparator (10X magnification), using pre- and post-test X-ray photographs and weight measurements as verification of results. The total ablation depths were determined by scraping down to the virgin material (through the char and reaction zones). The material of interest for this research is located at the bottom right. The black carbonaceous char, as well as some level of intumescence, can be observed on the sample. The pre- and post-test photographs are provided in Figure 35. The resulting ablation measurements are provided in Table 3. The recession measurements represent the mechanical removal of material. Based on the level of aerodynamic shear, this erosion can be of fully charred carbonaceous material, various states of pyrolysing material, or virgin material. As shown in the table, the material actually intumesced past the original surface. Upon further investigation and measurement, it was determined that the material retained 0.02-inch of relatively strong carbonaceous char with an additional 0.01-inch of heat-affected material. This resulted in a distance from the original surface position to the virgin material of approximately 0.01-inch representing the total ablation. Uncertainties in the weight measurements limited usefulness for determining mass loss and were not used.



*Figure 33. Sled Vehicle During Peak Velocity*



*Figure 34. Sled Test Samples After Test*



*Figure 35. Pre- and Post-Photo of Sled Sample*

Table 3. Measured Ablation Depths

	Recession Depth (in.)	Fully Charred Thickness (in.)	Pyrolysis Depth (in)	Total Ablation Depth Atot (in.)
Material	- 0.020*	≈ 0.020	≈ 0.010	≈ 0.010

\* - negative sign implies swelling; material behaved as a true intumescent

## 5. Sled Test Summary

In summary, the sled test at 4950 ft/sec provided a means of characterizing mechanical shear effects on representative thermochemically decomposing and intumescent heatshield materials. Although thermocouple measurements were not performed, the measured erosion and decomposition provides sufficient data to assess the surface and in-depth phenomena occurring in response to aerodynamic heating. Future testing will include thermocouple data as well as sustained velocity environments that will further reduce the disadvantages of the sled test facility and ensure more accurate quantification of the thermodynamic and mechanical response of ablating heatshield materials.

## E. Material Description

### 1. Application

The material investigated for this research was selected due to the highly intumescent and internally decomposing behavior. This behavior has been identified under a number of test and evaluation efforts also recognizing these types of materials as being superior heatshield materials under moderate to low shear conditions. The material intumesces and through decomposition, reradiation, and conduction path growth, minimizes the support structure temperature rise. The material is a sprayable or trowelable fiber-reinforced intumescent-epoxy. It functions as an intumescent (char swells) under low to moderate shear in high temperature environments. The material goes through thermochemical decomposition when exposed to high temperatures and generates a relatively thick insulating layer. It has been observed by Nourse et al. [55], however, that possible thermal protection applications exist for these types of materials in moderate to high-shear aerothermal environments.

### 2. Thermal Properties

Temperature dependent thermodynamic properties were determined by Perry et al. [56] and are provided in Figure 36. The temperature range of the data is limited due to the decomposition phenomena that occur while trying to record data at elevated temperatures. This behavior further supports the goal of modeling the thermochemical decomposition and obtaining the relative thermal properties of the char, pyrolysis, and virgin layers as a function of temperature as opposed to “effective” thermal properties. If the contribution of each thermal property is not specifically identified, then use of the analytic model for different aerothermal environments may result in incorrect in-depth thermal response predictions. Utilizing the laser thermal test results with embedded thermocouples, it was possible to “back out” the necessary combination of thermal conductivity and specific heat while incorporating the thermochemical decomposition and intumescence or conduction path growth. This was accomplished through the use of transient density measurements and intumescence to validate the thermochemical decomposition predictions and ensure more realistic conduction effects to be isolated as opposed to assuming gross effective thermal properties to include decomposition. The resulting thermal conductivity and specific heat properties are provided in Figures 37 and 38, respectively. A comparison of previously used properties without the effects of intumescence is included to show the fundamental importance of modeling intumescence effects on conduction heat transfer. As evidenced in Figure 37, a fundamental difference in thermal conductivity for the various decomposition states can significantly affect the applicability of heatshield analytic design models when not accounting for the relative intumescence behavior in low shear aerothermal environments. The current approach in CMA is to utilize a weighting factor between fully charred and virgin states. A more appropriate method would be to attempt to understand the thermal properties for each phase of the decomposition process: virgin, pyrolysis, and fully charred. The same effect is experienced for the specific heat properties as shown in Figure 38. The primary point for these comparisons is that when attempting to model the true physics, material thermal properties can differ significantly causing concern for applying the “effective properties” method for environments and materials beyond what has been experimentally quantified.

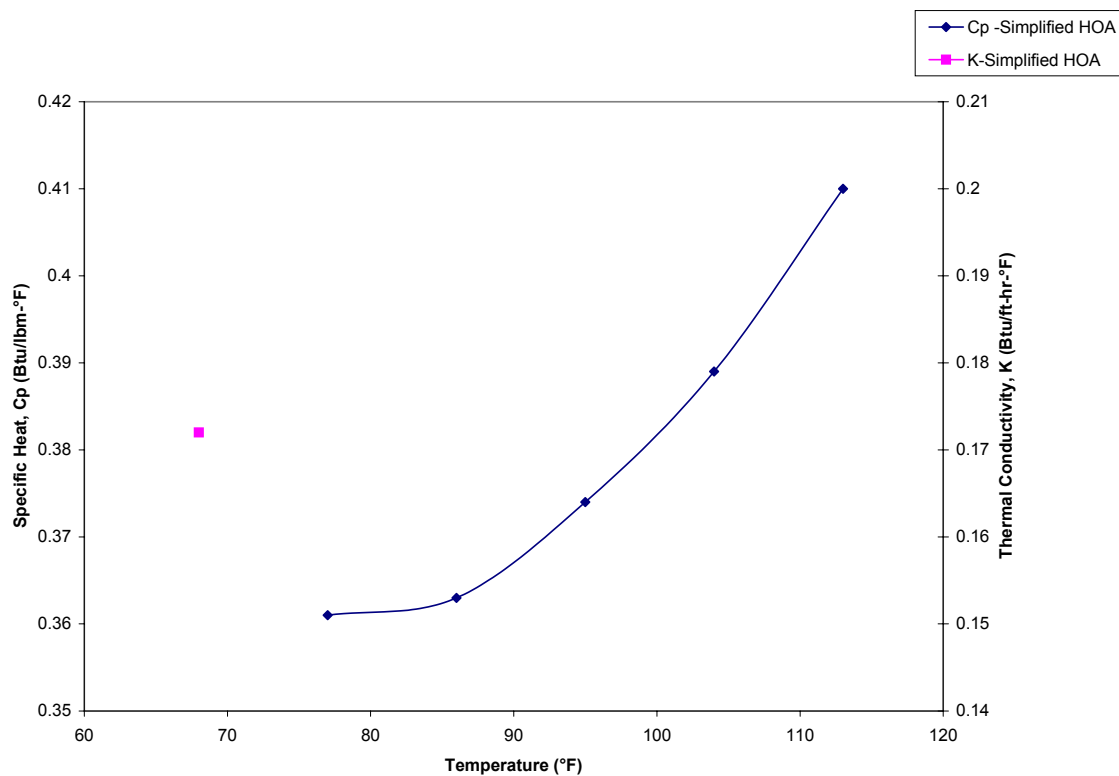


Figure 36. Measured Thermal Properties

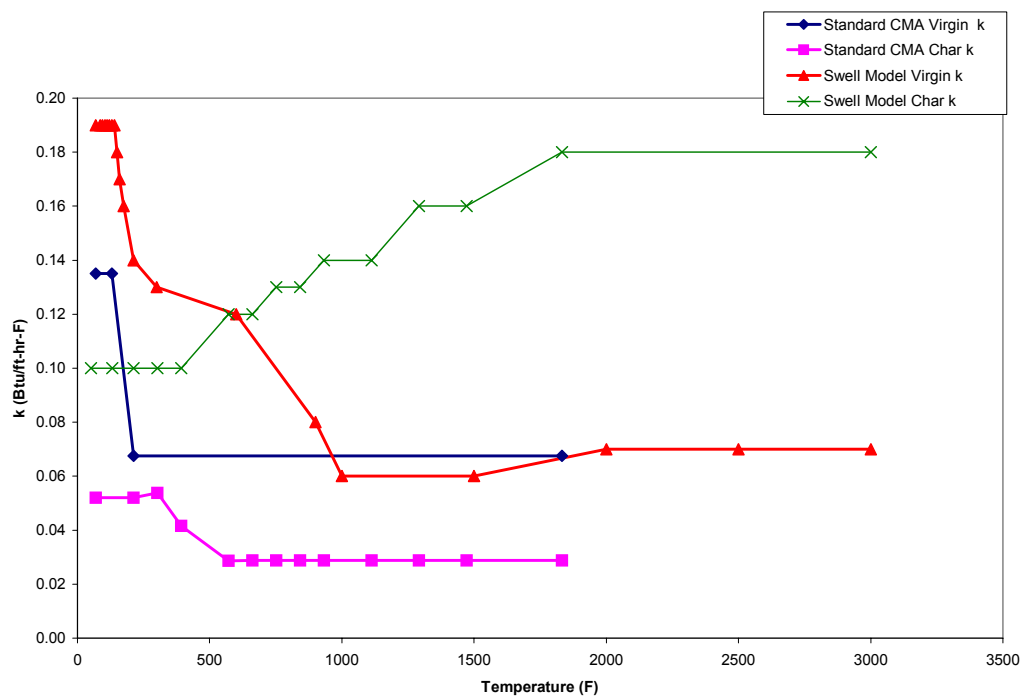


Figure 37. Intumescent Material Thermal Conductivity

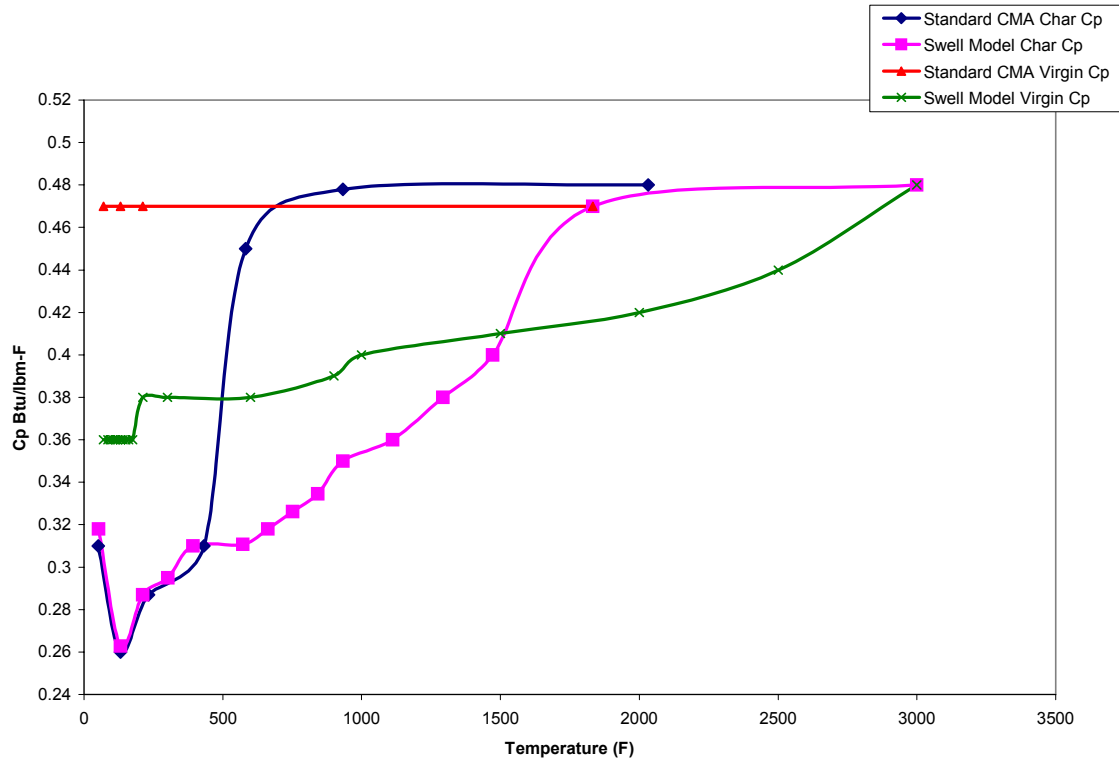


Figure 38. Intumescent Material Specific Heat

### 3. Elemental Composition

The elemental composition was determined for the virgin material [57]. The material composition was performed for use in the thermochemical decomposition model defining the virgin material, char, and pyrolysis gases. The organic composition shown in Table 4 represents the pyrolysis gases escaping the material, passing through the char, and mixing with the boundary layer gases. These elements gas out of the virgin material with increasing temperature leaving fully charred material. The inorganic composition shown in Table 5 represents the fully charred material that remains after decomposition is complete. The combination of organics and inorganics represents the virgin material before decomposition occurs. Percent weight of each element of organic and inorganic composition are required in the thermochemical equilibrium computer code, ACE81 [58], to define the pyrolysis gas composition in the boundary layer and their reaction with the free stream fluid as well as the fully charred material composition.

Table 4. Organic Elemental Composition

Moisture (%wt)	Carbon (%wt)	Hydrogen (%wt)	Nitrogen (%wt)	Oxygen (%wt)	Sulfur (%wt)
7.89	25.3	5.66	<0.50	24.7	8.54



Table 5. Inorganic Elemental Composition

LOI (%wt)*	Silica (%wt)	Sodium (%wt)	Sulfur (%wt)	Aluminum (%wt)
54.51	30.37	52.15	9.22	8.26

\* LOI - Loss On Ignition (Organic Constituents)

#### 4. Thermogravimetric Analysis

In addition to the characteristic thermal property measurements, thermodynamic decomposition (density decrease) as a function of temperature rise rate or heating rate was measured. These measurements are known as TGA, discussed in further detail by Doyle [59], and represent the outgasing effect that occurs when the temperature of a material exceeds reaction temperatures of the components. This outgasing causes the material to lose mass equal to the mass of the gases escaping. Since TGA involves using a very small sample to ensure no significant temperature gradient occurs and to assume a constant volume process, this mass loss can be directly related to a reduction in density. The curve generated by TGA represents the reduction in density as a function of temperature. Once the reaction process is complete and no additional decrease in density occurs, it is assumed that the remaining mass represents the fully charred material (i.e., char density). These results are utilized to define decomposition kinetics as discussed by Russell [60] where specific coefficients are developed to model an intumescent heatshield material decomposition response.

The TGA's were performed on a V2.2A Dupont 9900 [61] thermal analyzer considering two heating rates. The first heating rate was approximately 20 °C per minute representing a relatively common level for TGA. The second heating rate was the maximum possible for the device to assess sensitivities of the material decomposition and reaction rates. Nitrogen, an inert gas, at a pressure of 75 psig was used as the medium in the reaction chamber. A non-reactive medium was desirable to model in-depth anaerobic thermal decomposition in the material. Sample sizes ranged from 15.5 mg to 28.7 mg. Figure 39 provides the peak heating rate TGA data. As can be observed in Figure 39, there are essentially four or five reactions that must be specifically modeled to ensure an accurate characterization of the internal decomposition. The peak reaction rate of 0.17%/°F for RX2390 occurs at approximately 600 °F with fairly substantial reactions occurring at even lower temperatures. The current kinetic model used for this research accounts for four reactions all occurring below 1500 °F. The additional reaction after 2000 °F is questionable and will be investigated in future efforts. Based on weight loss for the LHME test series, this fifth reaction may be real and results in reducing the fully charred density to as low as 15 lbm/ft<sup>3</sup> as opposed to the 29 lbm/ft<sup>3</sup> assumed below 1500 °F. An additional consideration is that as heating rate increases, it has been observed that the TGA curves shift to the right resulting in less decomposition for a given temperature. While the 50 °C/min heating rate is experienced at depth, a significant portion of the decomposing and intumescent material experiences heating rate much higher. For the LHME tests, the heating rates reached more than an order of magnitude higher and stayed an order higher throughout the test. Additional test and evaluation using the LHME facility could allow for TGA to be performed at the actual heating rate experienced at hypersonic flight (without shear).

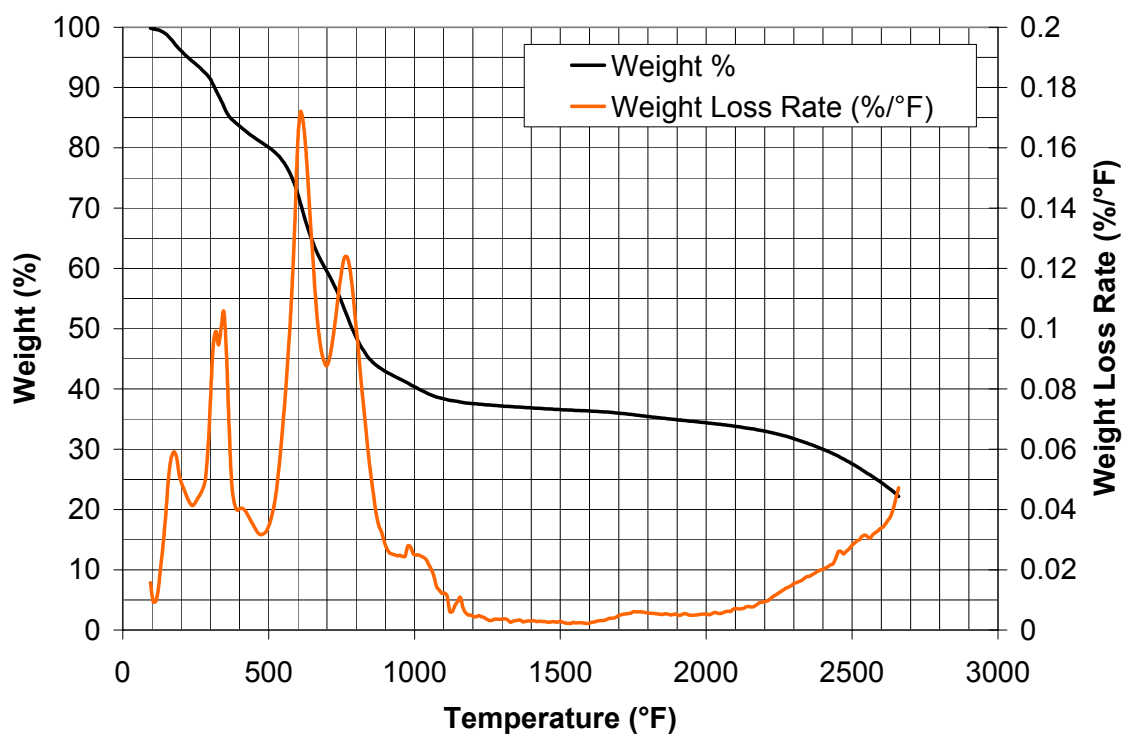
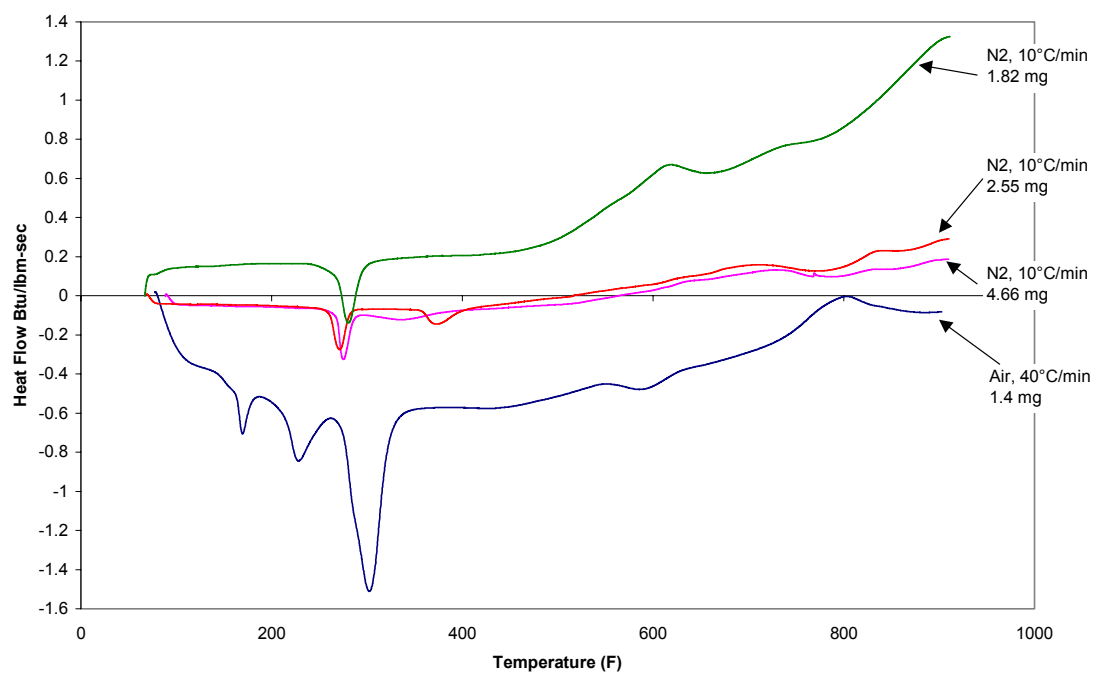


Figure 39. Thermogravimetric Analysis at 50 °C/minute

## 6. Differential Scanning Calorimetry

The Differential Scanning Calorimetry (DSC) can be used to determine specific heat as well as pyrolysis gas enthalpies [62]. Pyrolysis gas enthalpies are required when using a thermochemical decomposition model to account for the energies of decomposition in the in-depth energy balance. For highly endothermic reactions, effects can be significant for predicting temperature response. For highly exothermic reactions, the predicted temperature can increase significantly. As in the TGA, it is important to obtain DSC in an inert environment. For this research, both air and Nitrogen environments were used to obtain a comparison. Figure 40 provides the DSC obtained in both an air and Nitrogen environment. The air DSC heating rate was 40°C/min while the Nitrogen DSC was at 10°C/min. As a result of sample size differences, the plots were weight-normalized to provide a more appropriate comparison. The air DSC was the first data collected and primarily used to obtain the initial pyrolysis gas enthalpy tables for the material model. As can be seen, there are three main reactions. Since the measurement was taken in air and no additional data was available at the time, this DSC was only used as a guide and approximations were assumed on the shape of the DSC. Additional DSC data was collected in Nitrogen. However, based on the weight-normalized results, the data is suspect and additional investigation is required prior to incorporating the pyrolysis gas enthalpies from this data. As can be seen, the smallest sample size (1.82 mg) suggests exothermic reactions throughout the heating period of the sample. Additionally, near room temperature where determination of specific heat can be obtained prior to decomposition, the curve is exothermic which makes the data suspect. All curves show an upward trend toward less endothermic after 350 °F. However, no data was collected for the higher temperatures where according to TGA, additional reactions occur.



*Figure 40. DSC Data*

## **V. COMPARISON OF EXPERIMENTAL AND COMPUTATIONAL**

### **A. Intumescence Model Validation**

#### **1. Introduction**

The analytic modeling of intumescence behavior has been identified as being critical to the optimization of designing heatshield requirements. Intumescent materials have shown superior performance for a wide range of applications. The physical movement of the heated surface away from the structural components thereby increasing the conduction path can result in significant thermal performance. It is common for intumescent materials to increase conduction paths more than a factor of two. This phenomenon is widely utilized in fire protection and radiation insulation requirements. However, for high-performance missile system requirements, these types of materials are generally overlooked due to a lack of analytic modeling capability. Much of the phenomena that make an intumescent material superior is complex and requires a detailed understanding of material properties and decomposition. Through recent research and experimental validation, reasonable design models of intumescent materials have been developed. While there remains a level of empiricism, strides have been made in understanding either specific phenomena inducing intumescence or direction in which additional research should be performed to obtain a more accurate understanding of contributions to intumescence.

The following discussion provides a comparison of analytic predictions with experimental data in the hopes of obtaining validation of the numerical intumescence model incorporated in CMA87S. While the research initiated with some baseline premises, it was discovered that modifications to the original approach were required. Much of these modifications were a direct result of utilizing appropriate aerothermal test facilities to decouple phenomena and obtain specific contributions. An example of this was in the use of the LHMEI test facility to obtain real-time radiography and embedded thermocouples to specifically quantify in-depth thermochemical decomposition behavior. These tests, while not specifically duplicating a hypersonic convective environment, provided a means of quantifying intumescence and density changes as functions of heating rate. Additionally, a specific thermocouple response was directly associated with the various regions of decomposition. By allowing for the measurement of intumescence rate for a given decomposition state and heating rate, an analytic model could be developed to capture as accurately as possible the specific thermophysical behavior and make the model applicable for any external aerothermal environment. With the analytic modeling capability enhanced and design approaches available, confident use of the superior performance of intumescent materials is possible.

## 2. Test 1 & 2 Baseline Intumescence Model

The LHMEL test program provided the most appropriate method for quantifying the intumescence behavior of heatshield materials. Previous research efforts have been conducted prior to the development of real-time radiography and were greatly limited in development of models for intumescence. This was a result of only knowing pretest and posttest positions independent of highly transient decomposition zones and intumescence path. In some cases thermocouple bead separation from local layers caused thermal response to become erratic. In the case where epoxies or other filler materials were used to secure thermocouple beads, upon reaching the heat of decomposition temperature of the filler, a gassing off occurred effecting thermocouple response. Sometimes thermocouple wires failed during intumescence due to a lack of “slack” or sufficient strain relief. The ability to map the transient position of each thermocouple bead as well as the identification of each decomposition range and the intumesced heated surface provided the unique ability to validate the analytic models. The LHMEL test facility and use of real-time radiography provided the ability to validate the analytic models developed to predict intumescence as a result of hypersonic type heating environments.

The baseline intumescence model was developed using the transient data collected on the two thermal tests conducted at LHMEL. By having a range of heating rates, the heating rate dependency of intumescence could be determined. The model validation initiated by using the baseline intumescence model depending solely on decomposition state and comparing in-depth thermal response at each of the thermocouple stations. The intumescence function was modified until the transient positions of heated surface, initial thermocouple bead, and in-depth heat affected region (decomposition and virgin material interface) were matched. Matching rates rather than final positions provided an added fidelity to the analytic model. Once these intumescence trajectories were matched, the surface temperature and in-depth thermocouple response were matched through modification of temperature dependent properties. These properties were modified in two steps. The first step used the non-decomposing material regions and corresponding thermocouple response to obtain virgin material property matches. The 0.15-inch thermocouple station data was used as a driving boundary condition to match the 0.25-inch thermocouple station response. The resulting properties were considered appropriate for the virgin material below the onset of decomposition (approximately 220 °F). Assuming these properties fixed, the next step was to modify iteratively the intumescence model and pyrolyzing region thermal properties to obtain a best match for both intumescence rate, total, and thermal response. After these final “best match” conditions were selected, the same analytic model was used to predict heatshield behavior in a realistic convective hypersonic high altitude environment for which significant test data had been previously collected. Application to a convective environment quantified the usefulness of the analytic model as well as the use of the LHMEL test facility to develop intumescence material properties. The analytic model was then used to predict thermal response for a supersonic sea-level (high shear) convective environment to evaluate applicability for high shear conditions. The results of these predictions provided indications of accuracy, applicability, and necessary model refinements for future research.

The resulting char state and heating rate dependency factors are provided in Figure 41. These relationships represent the “best fit” combination for matching the LHMEI test conditions. However, through additional refinement and more accurate measurement of thermal properties for the various pyrolyzing regions, these fits may be improved. It is important to note that while these curves are considered a baseline, they do provide insight to the relative influence and trends associated with the intumescence phenomena. For example, considering the char state factor, it is evident that the majority of intumescence occurs in the initially pyrolyzing region where decomposition is below 32 percent weight loss. Therefore, the higher charred region experiences less intumescence that is contrary to the hypothesis suggested by Laub et al. [63] during the Ramburner Test Program. However, this may be material-dependent since the material investigated during the Ramburner program was an intumescent but different than that investigated during this research.

The lower intumescence of the charred region was again observed during the hypersonic convective thermal testing where it was seen that an insignificant level of additional swell was experienced between 200 and 300 seconds of testing. The additional 100 seconds of heating caused additional decomposition of the more fully charred regions but little additional intumescence. The addition of the heating rate factor was a result of realizing that the use of only char state to quantify intumescence, a reasonable match of intumescence and in-depth thermal response could not be obtained for the wide range of thermal environments. When either the char state or heating rate factor is zero, the intumescence prediction is zero since these represent multipliers in the analytic approach. While the heating rate factor shown in Figure 41 indicates values at the lower and higher char states while the char state factor is zero, this is largely due to model iterations to obtain an accurate match for the LHMEI test results. When a reasonable match was obtained for Test 1 data, the intumescence was unacceptably excessive for the lower heating rate of Tests 2 and 3. Using the data collected for Test 3 where no significant intumescence occurred after 200 seconds and the corresponding in-depth heating rates shown in Figure 42, the heating rate dependency factor was developed. It was observed that below heating rates of approximately 72 to 180 °F/min, very little intumescence occurred. Additionally, using the transient radiography from Tests 1 and 2, the thermocouple station at 0.05 inches began moving when the heating rate reached and exceeded 180 °F/min. The corresponding heating rate at the 0.05-inch station is provided in Figure 43 for Tests 1 and 2. This coupled with the transient radiography provided a means of determining the relative heating rate and temperature at which the thermocouple motion initiated. By adjusting this heating rate dependency, the resulting intumescence factors shown in Figure 41 were selected providing a reasonable match for both laser thermal tests as well as the hypersonic convective thermal tests of Test 3. It is possible that the heating rate dependency is a result of higher pyrolysis gas generation rates and limited gas transfer causing the localized material to “puff up” and initiate expansion after which intumescence is reduced and less dependent on heating rate. These concepts will be investigated in future research to expand the analytic model applicability to a wider range of convective aerothermal and radiative environments.

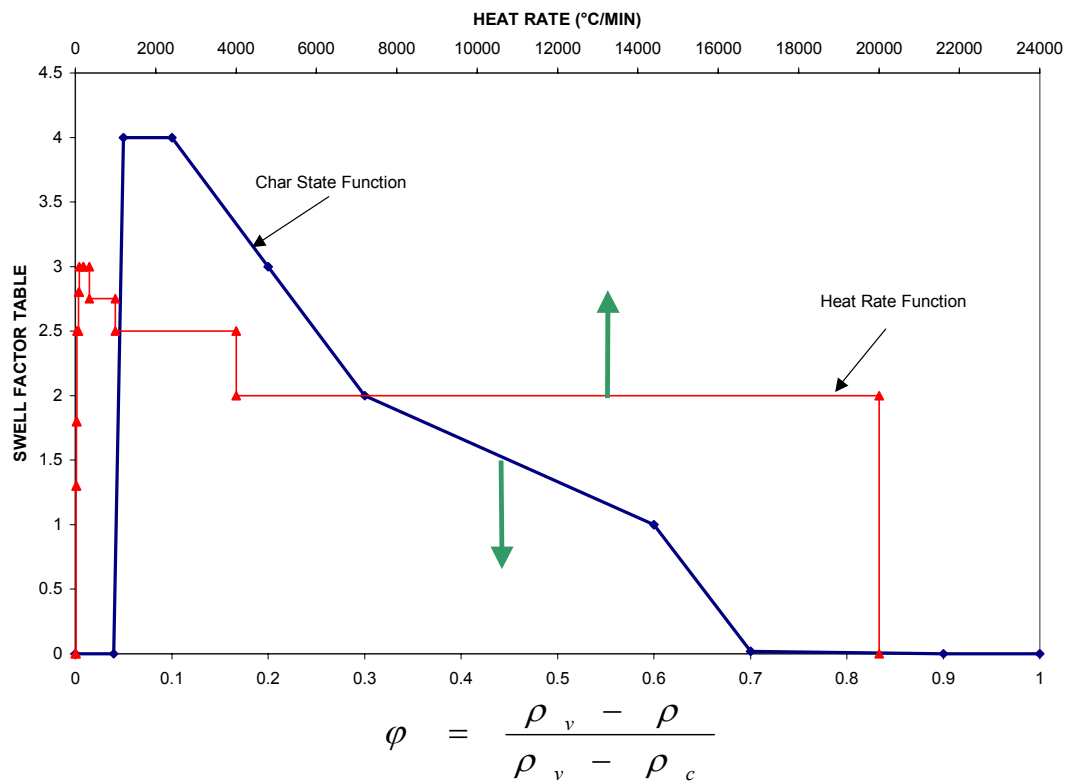


Figure 41. Intumesence Model Functions

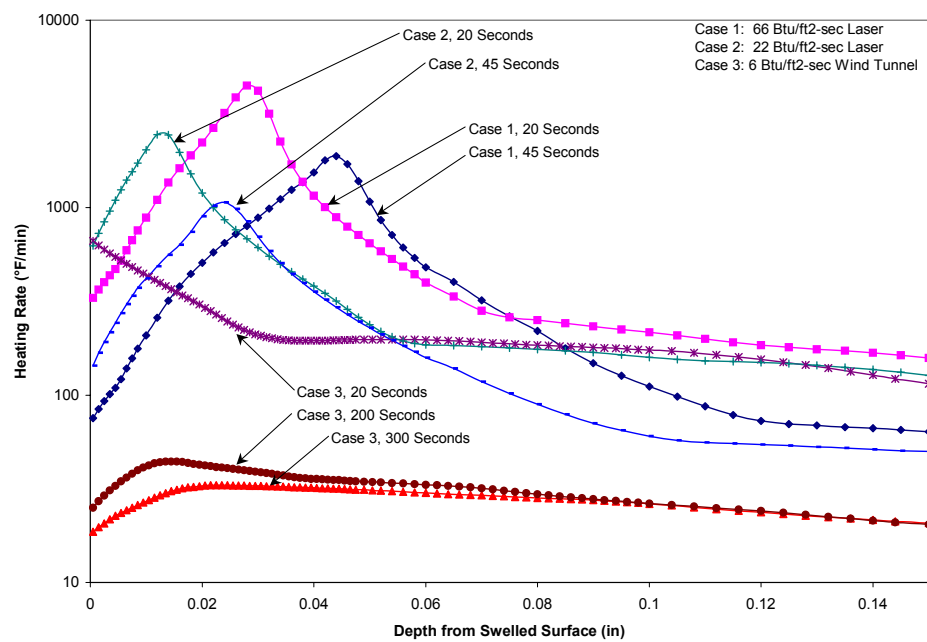
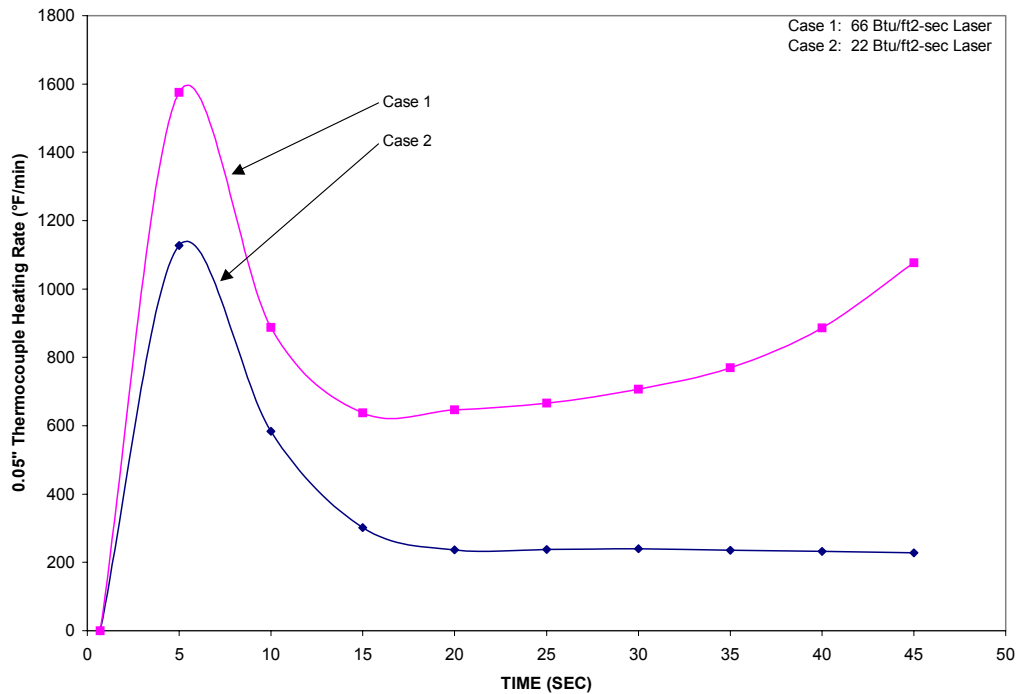


Figure 42. Intumesence Model Validation Tests Heating Rates



*Figure 43. Laser Thermal Testing 0.05-inch Thermocouple Heating Rate*

The predicted transient intumescence, as compared to data collected from the transient radiography is provided in Figure 44. Identified in this figure are the surface position, in-depth decomposition, and the 0.05-inch thermocouple motion. The data was collected from video of X-ray data. More accurate measurements will be provided upon completion of the digitized radiography where specific density measurements will be identified as a function of time and depth along with the transient intumescence. Exceptional agreement is obtained for the surface motion using the proposed factors. Some variation in data exists due to unevenness in the intumesced surface. A reasonable match was obtained for the in-depth decomposition assuming the ability to distinguish a 5 percent density loss in the radiography. The analytic model appears to over predict the initial decomposition rate moving in-depth. This could be a result of uncertainties in thermal properties or inaccuracies in identifying the decomposition front from the radiography. The digitized radiography data will provide a more accurate characterization of the relative decomposition regions and motion. The 0.05-inch thermocouple motion shows very good agreement suggesting that not only total growth but also expansion rate is being modeled with reasonable accuracy. The initiation of thermocouple motion was noticeable for each of the tests at approximately 17 to 20 seconds with a measured temperature of 250 to 260 °F. This data was identified by an event that appeared for the radiative heating environment imparted using the LHMEI test facility as well as the hypersonic convective environment imparted by the NASA HGTF. The thermocouple response appears to be disrupted at this time and temperature and is clearly an indication of intumescence and decomposition below the thermocouple. This event is highly repeatable and will be investigated using the digitized radiography.



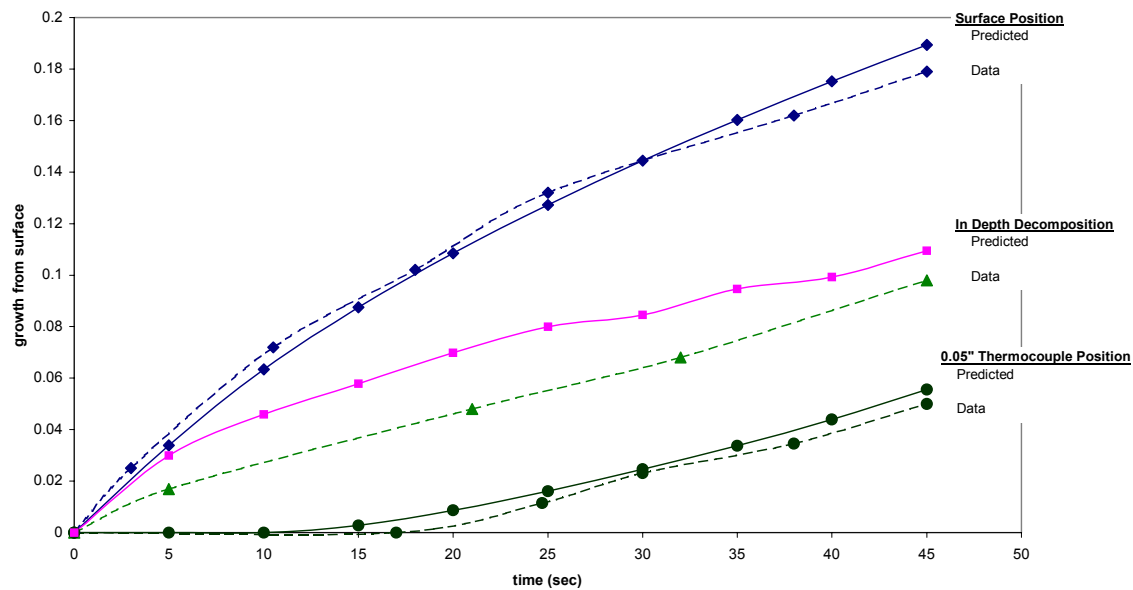
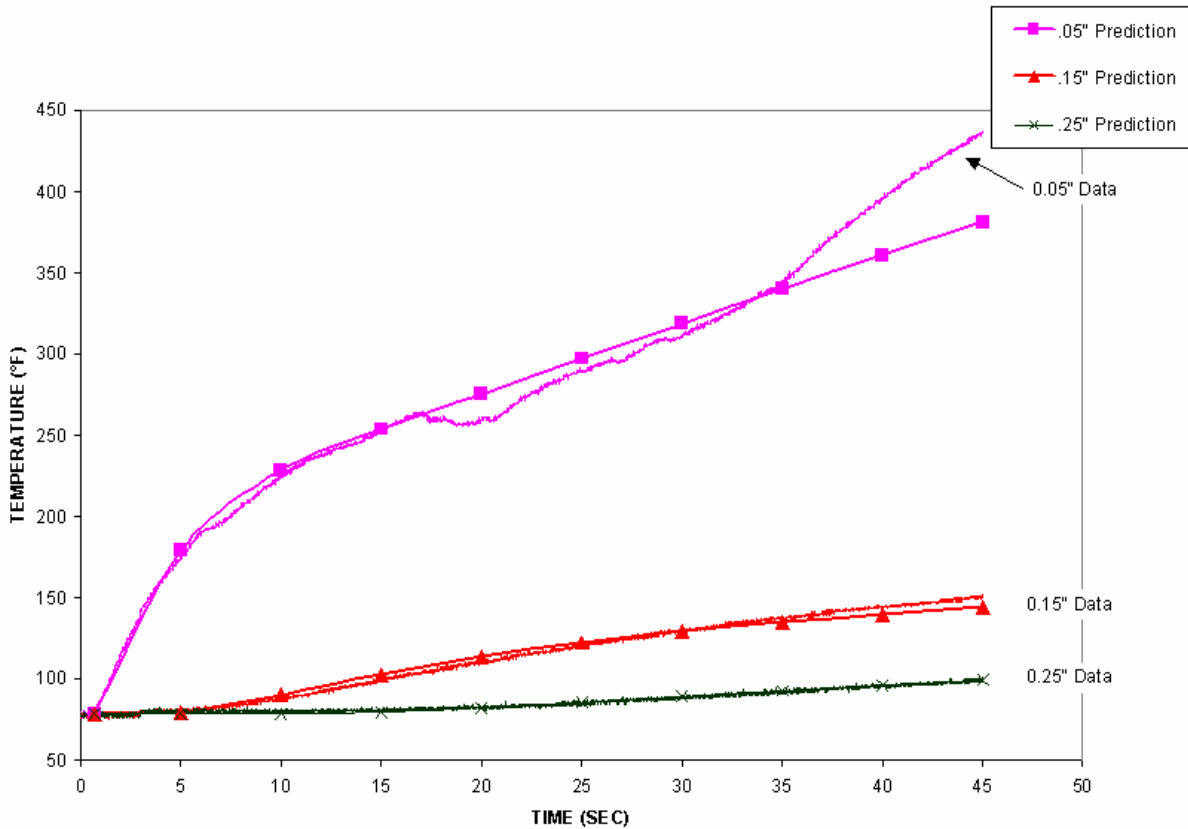


Figure 44. Intumescence Behavior Predictions Versus Data

Figure 45 provides a comparison of analytic model predictions with measured test data for the lower heating rate laser test, Test 1, in which a heating rate of 22 Btu/ft<sup>2</sup>-sec was imparted to the sample surface. Surface temperature data reduction has not been completed. However, “quick look” data indicated very good agreement between the model predictions and optical pyrometer measurements with peaks of approximately 2000 °F. The surface temperature data and prediction comparisons will be better quantified after completion of data reduction. As can be seen in the figure, a very good match was obtained throughout the test until the thermocouple measurement and prediction intersect at approximately 34 seconds. This is initially thought to be not possible because the intumescence should make the thermocouple bead always remain below the predicted thermal response of the prediction for the 0.05-inch location. It is possible that the slope of the predicted curve should be higher at the earlier time of approximately 17 seconds causing the prediction to remain above the measured response.



*Figure 45. Test 1, Overall Thermocouple Response Predictions Versus Data*

It should be noted that a series of analytic trades were performed during the thermal response predicts to define sensitivities to node size in the finite difference mesh resolution. Previous methods suggested node thicknesses on the order of 0.010 inch to 0.005 inch sufficiently captured the thermal gradient through the decomposing heatshield material. As a result of incorporating the intumescence model, it was determined that mesh resolution of 0.002 inch to 0.001 inch was required to accurately define the thermal gradients through the char and pyrolyzing regions. With additional statistically significant testing, better definition of thermodynamic response and corresponding sensitivities to mesh and material properties can be developed.

Since good agreement was obtained for the initial 20 seconds of heating, the thermal response predictions at the 0.15-inch and 0.25-inch positions matched the measurements well. Figure 46 provides an expanded scale of the 0.15-inch and 0.25-inch thermocouple responses. Some disagreement in slope at the end of the test was experienced, but with additional refinement of thermal properties this can be reduced.

Figure 47 provides the in-depth thermocouple response predictions for the higher heating laser test, Test 2, as compared to data. While not shown in the figure, the surface temperature measurement and predictions were in good agreement with peaks of approximately 2700 °F. Again, the surface temperature data and prediction comparisons will be better quantified after completion of data reduction. As can be seen, at approximately 17 seconds the measured thermal response drops and recovers its increasing slope. As a result, the 0.05-inch thermocouple response does not truly represent the 0.05-inch layer within the decomposing material. Therefore, the temperature prediction should be higher throughout the remainder of the test. Since no significant intumescence occurred at the 0.15-inch and 0.25-inch thermocouple positions, the thermal response measurements are smooth. For the assumed pyrolyzing region thermal properties and intumescence factors, a reasonable match is obtained for these thermocouple measurements. Figure 48 provides an expanded scale to see the in-depth thermal response predictions. As expected for the assumptions made, a slightly higher heat flux is reaching in-depth resulting in a slightly higher thermal response prediction as compared to the test data. This is primarily a result of not matching the 0.05-inch thermal response exactly during the first 15 seconds. With additional iteration of thermal properties, a better match could be obtained throughout the test. However, the primary goal of this effort is to develop analytic models to account for intumescence. Future efforts will be directed toward better quantifying in-depth thermal properties as a function of decomposition and temperature. The ability to model intumescence provides a means of more accurately decoupling and quantifying thermal properties of an intumescent material.

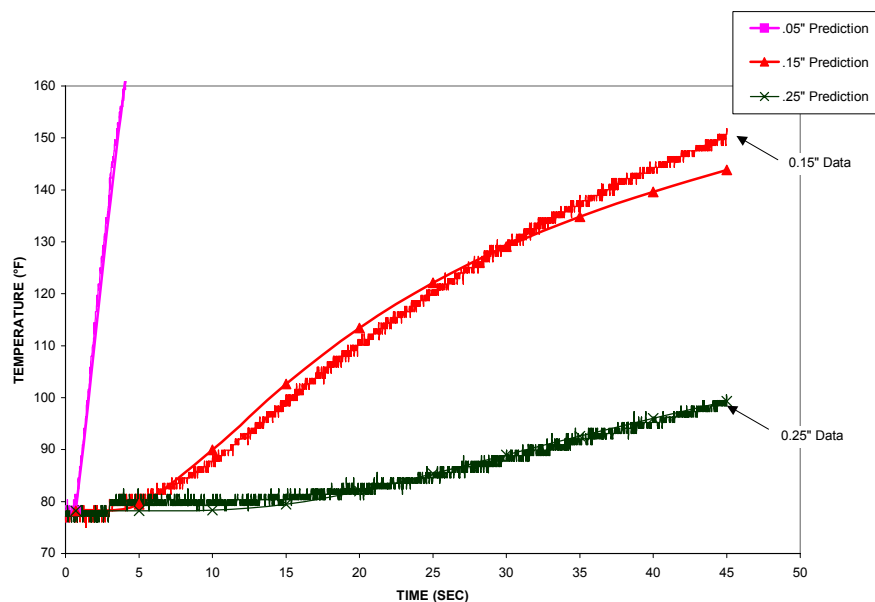


Figure 46. Test 1, In-depth Thermocouple Response Predictions Versus Data

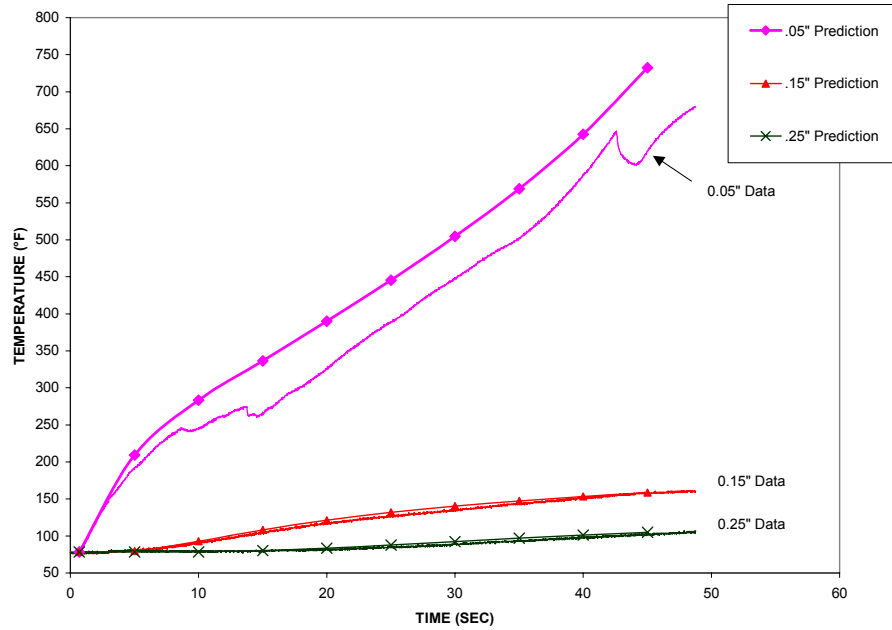


Figure 47. Test 2, Overall Thermocouple Response Predictions Versus Data

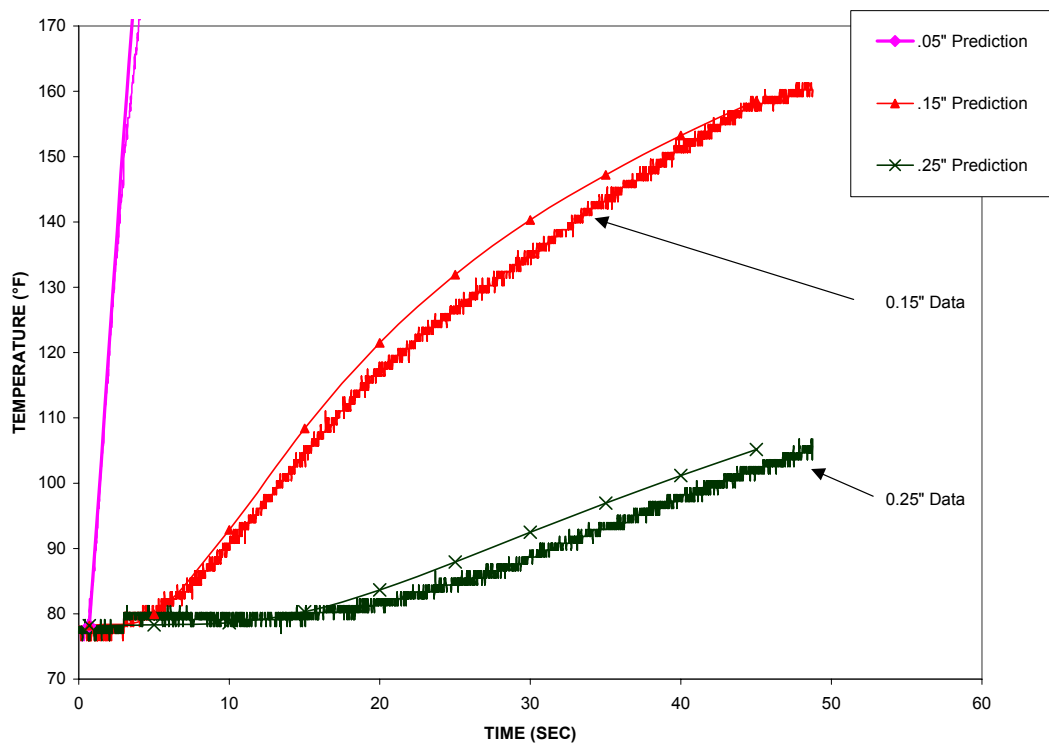


Figure 48. Test 2, In-depth Thermocouple Response Predictions Versus Data

Table 6 contains the predicted mass loss results as compared to the measured values. The initial predictions do not include observed two-dimensional effects due to conduction and increased decomposition outside the laser beam diameter. Additionally, not included is the increased decomposition seen in the TGA results for the higher heating rate and temperature levels induced during Test 2. The second predictions attempted to account for both effects seen during the test and as expected brought predictions and data within reasonable accuracy. It should be noted that the TGA model was developed for a maximum temperature of approximately 1500 °F. For the higher heating rate where surface temperatures approached or exceeded 2700 °F, additional decomposition occurs in the char and results in additional mass loss. To evaluate this effect, a series of analytic trades was performed verifying that with additional decomposition and char density reduction to approximately 15 lbm/ft<sup>3</sup>, the test data and analytic predictions show very good agreement. The result of this study indicates that a more rigorous study of TGA at very high heating rates and temperatures should be performed to minimize the uncertainty of the decomposition model at hypersonic aerothermal environments.

Table 6. Mass Loss Comparison of Predictions and Measurements

	Test 1			Test 2		
	Data	Prediction	Percent Delta	Data	Prediction	Percent Delta
Weight (grams)	1.60	1.21	32	3.2	1.40	220
Modified Model Weight (grams)	1.60	1.4	13	3.2	2.6	19

### 3. Test 3 Intumescence Predictions

The resulting predicted thermal response and intumescence agreement obtained for the two laser heating tests led to the application of the analytic model and corresponding intumescence properties to the hypersonic convective heating test environment. The resulting predictions as compared to data are provided in Figures 49 and 50. As can be seen in Figure 49, the surface temperature prediction matches for the initial 50 seconds. However, the curves deviate slightly suggesting the need for additional understanding of the char state density and thermal properties. Good agreement is obtained for the in-depth thermal response matching both magnitude and slope. This was one of the primary goals of developing the intumescence model. The necessity of better predicting the heat transfer and resulting thermal response slope was evident when applying the analytic model to longer heating times seen in actual flight conditions. Original model predictions gave significantly different slopes for the test time and would actually predict excessively higher thermal response and resulting excessive heatshield requirements for continued heating. The same thermocouple event can be seen as in the laser tests at a similar decomposition state and temperature. Using in-depth heating rate predictions and measured thermal response, an indication of motion and onset of decomposition was obtained. Similar to the lower heating rate laser test analytic results, the predicted 0.05-inch thermal response intersects the measurement and suggests additional refinement is necessary for the more decomposed high-temperature material. Figure 50 in-depth thermal response at 0.15-inch and 0.25-inch stations show reasonable agreement. The thermal penetration is slightly

high between the 0.05- and 0.15-inch stations but is slightly low between the 0.15- and 0.25-inch stations. This disagreement can also be remedied through better accuracy of thermal properties. To provide a comparison with the previous analytic model predictions and quantify the relative influence of modeling intumescence on thermal response, Figure 51 is provided for the Test 3 predictions. The in-depth thermocouple responses are shown along with the previous and new model predictions. As can be seen, the previous model predictions gave thermal response slopes significantly different than test data. The test data indicated a decreasing slope or “plateau” and gradual increase in temperature at the 0.25-inch thermocouple position. The previous model predicted a relatively constant temperature rise rate suggesting an under prediction for early times and an over prediction for longer test times. The impact of the slope can be expressed as a function of predicted thermal protection requirements for flight test times longer than those experimentally induced. A significant increase in thermal protection and corresponding weight would occur adversely affecting system performance. However, the new model predictions clearly demonstrate a better match with the transient thermal response of the in-depth thermocouples. By more accurately predicting the transient thermal response, the model applicability is extended to actual flight environments providing accurate thermal response and heatshield predictions for a wide range of aerothermal environments and geometric configurations.

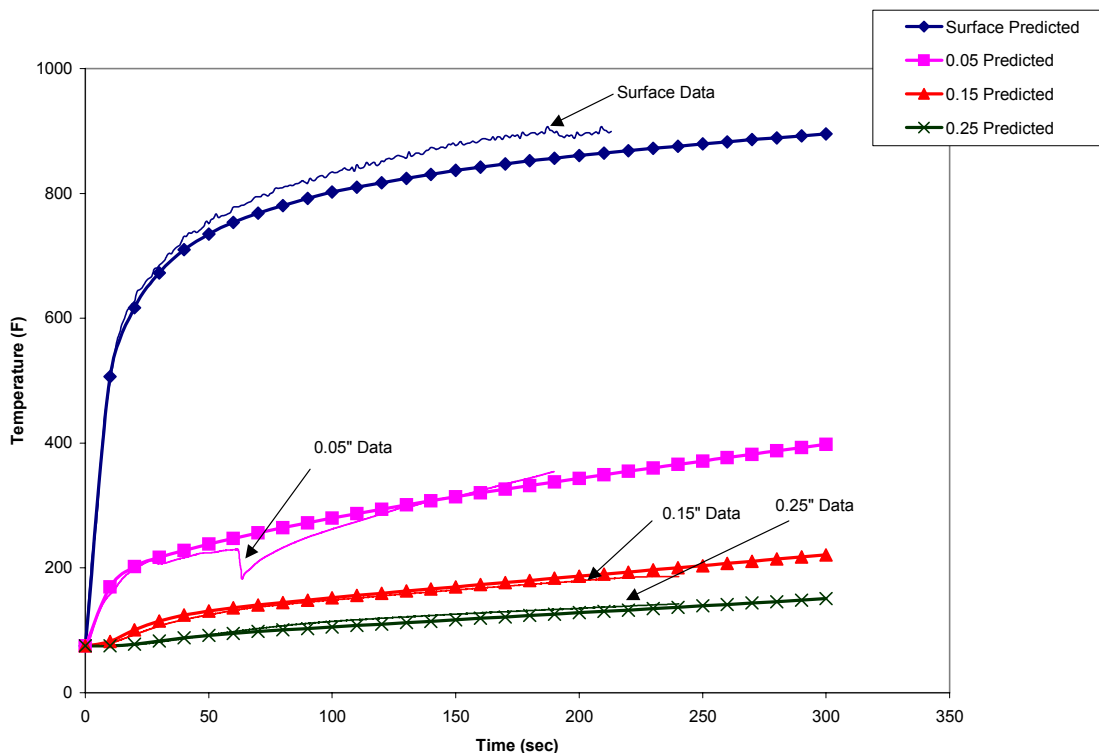


Figure 49. Test 3, Overall Thermocouple Response Predictions Versus Data

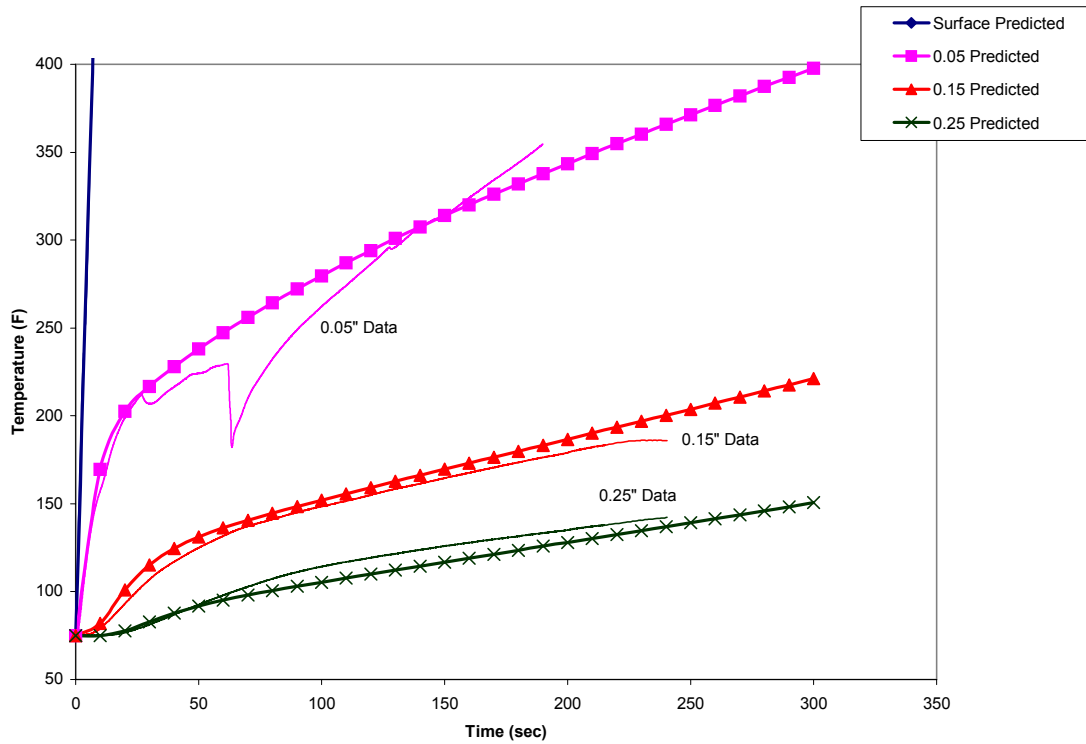


Figure 50. Test 3, In-depth Thermocouple Response Predictions Versus Data

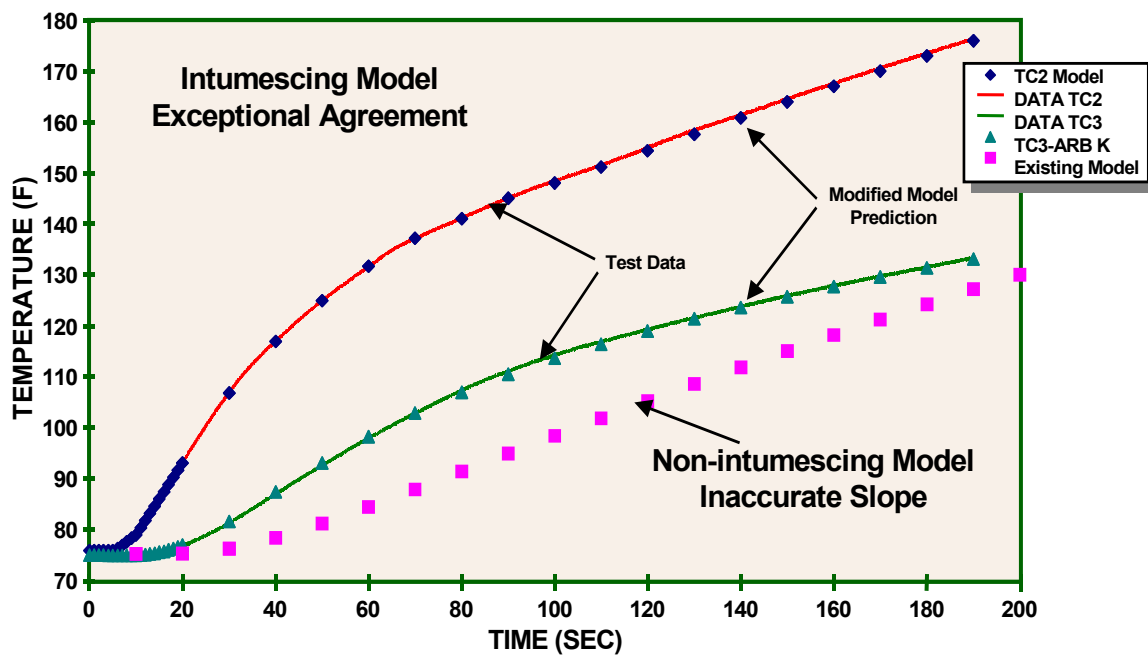
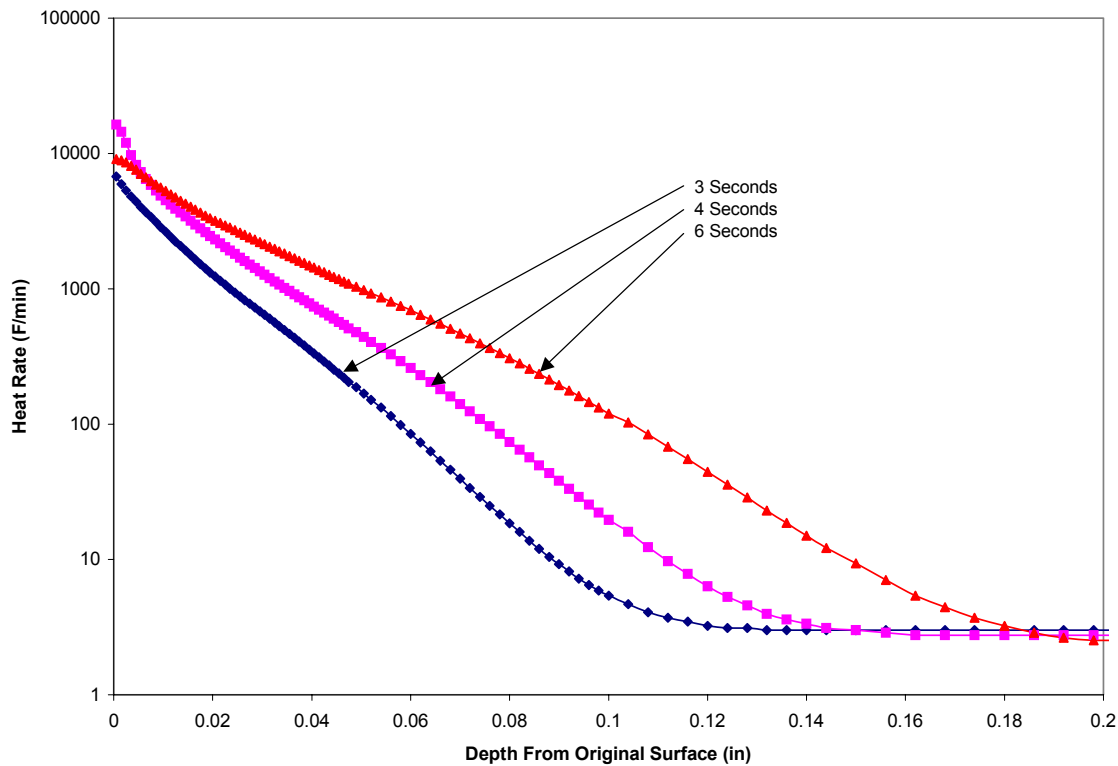


Figure 51. Test 3, Previous and New Model Prediction Comparisons

## B. High Shear Application

### 1. Sled Test Intumescence

Figure 52 provides the in-depth heating rate from the baseline analytic model obtained from the Test 1 and 2 conditions. It should be noted that these plots do not consider mechanical erosion and indicate only the contribution of intumescence on in-depth thermal response. As can be seen, the heat-affected depth is approximately 0.16 inches by 6 seconds. The peak heating rate on the surface is 10,000 °F/min. This figure can be used to identify the relative influence of heating rate on intumescence as compared to the effects during the other cases considered. Figure 53 provides the in-depth thermal gradients for the sled test. Predictions indicate relatively steep gradients through the initial 0.015-inch thickness. These curves also indicate the potential positioning of thermocouple instrumentation to obtain sufficient thermal response to minimize uncertainties. Figure 54 provides the char state function and corresponding density as a function of depth from original surface. As can be seen, the char state function “Phi” or “ $\phi$ ” discussed in Section II is generally confined to the initial 0.005 inches representing a very steep density gradient through the material. Again, it should be noted that this does not include mechanical shear that would possibly result in a reduced surface temperature and corresponding smaller temperature gradient.



*Figure 52. Sled Test In-depth Heating Rate Predictions*



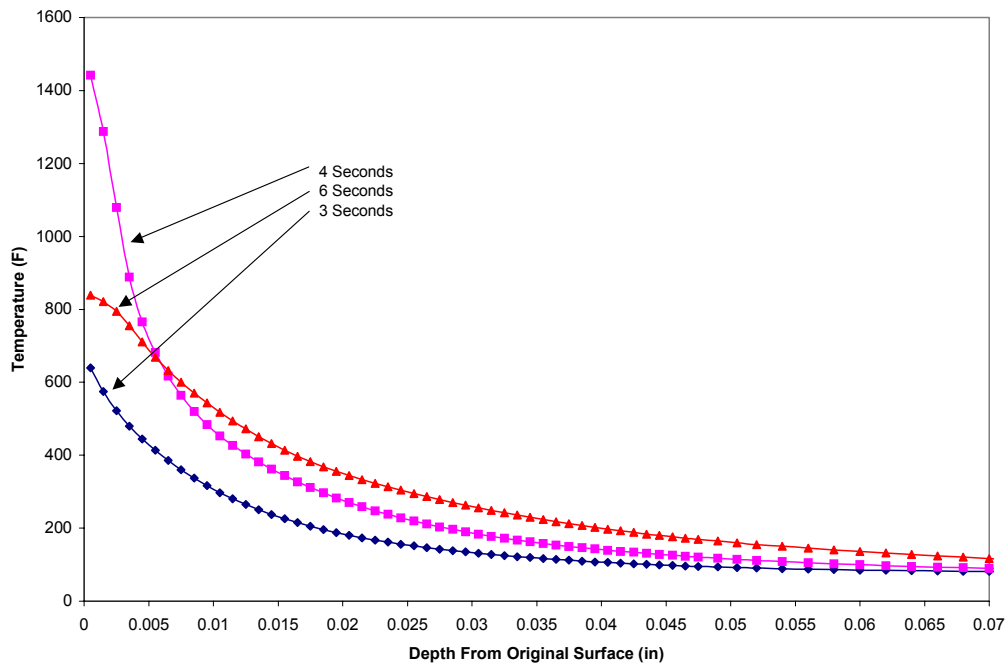


Figure 53. Sled Test In-depth Thermal Response Predictions

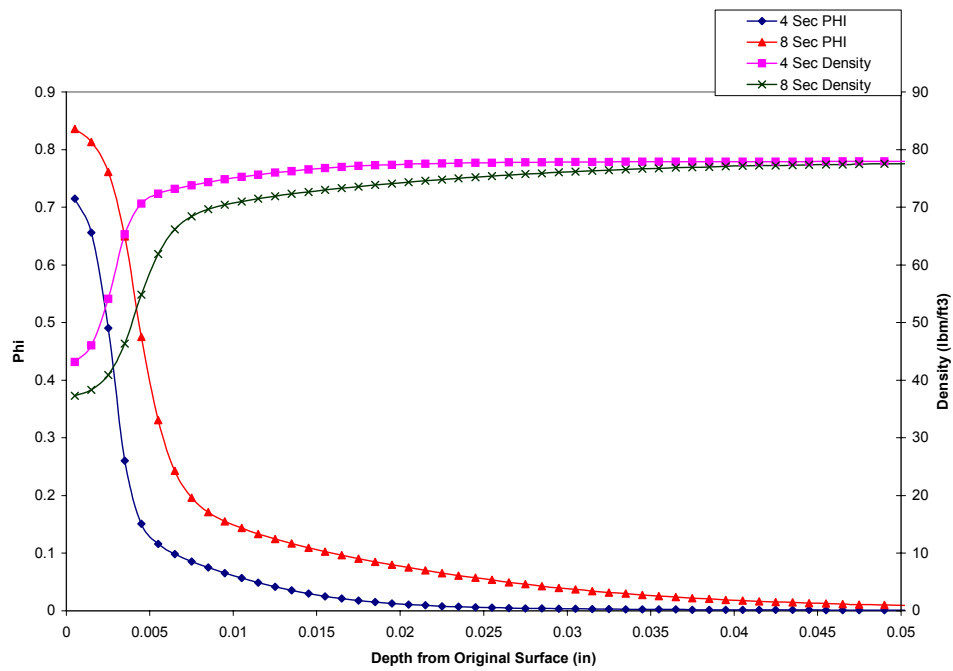


Figure 54. Sled Test Char State Gradient and In-depth Density Predictions

Figure 55 provides the predicted insulation thickness response as compared to the measured data. As can be observed, the analytic predictions provide a reasonable match with surface intumescence. However, in-depth decomposition predictions are not sufficiently accurate as compared to the measured data. The differences in intumescence and in-depth decomposition can easily be attributed to uncertainties in measurement due to the small level of total ablation. Additionally, the in-depth decomposition was derived from qualitative char state measurements. Since real-time radiography is not available for the sled test conditions, the identification of where the pyrolysis zone ends and virgin material begins is subjective. The analytic model predicts excessive in-depth decomposition while slightly under predicting the surface expansion or total intumescence. It is possible with the addition of mechanical shear and associated energy loss, less in-depth decomposition will occur. However, the intumescence must be examined more closely after addition of mechanical shear. Since the measurements and predictions are on the order of 0.01 inch, some level of uncertainty exists in the presumed decomposition data. To more accurately quantify this data, detailed radiography or wafer layer density measurements should be performed. This may indicate a larger depth of slightly decomposed material adding to the overall intumescence since it has been observed that a significant portion of intumescence occurs for the low char states. Figure 56 provides the in-depth thermal response predictions. Since thermocouple data was not obtained during the test program, validation cannot be obtained for the high shear conditions. In-depth thermal response is based solely on the thermal properties used in Tests 1 and 2. As can be seen, it is expected that very little thermal penetration occurs throughout the test. This would suggest that when using embedded thermocouples, efforts should be directed to locate beads very near the surface and test data should be collected for high shear convective environments. The peak surface temperature is approximately 1400 °F. The thermal response at 0.05 inch reaches approximately 190 °F by the end of the test. This is also indicative of the small region of material actually affected by the sled test thermal environment. For materials having a relatively low strength char, the higher shear conditions will remove material through mechanical erosion and reduce the influence of intumescence on conduction. During the peak velocity where highest heating and decomposition rates are experienced, dwell time is limited due to the transient nature of the sled test. As a result, very little mechanical erosion was observed even though a reasonably severe convective environment was subjected to the test sample. Future sled tests having the ability for sustained velocity would provide a significant enhancement in simulating hypersonic shear conditions coupled with convective aerodynamic heating.

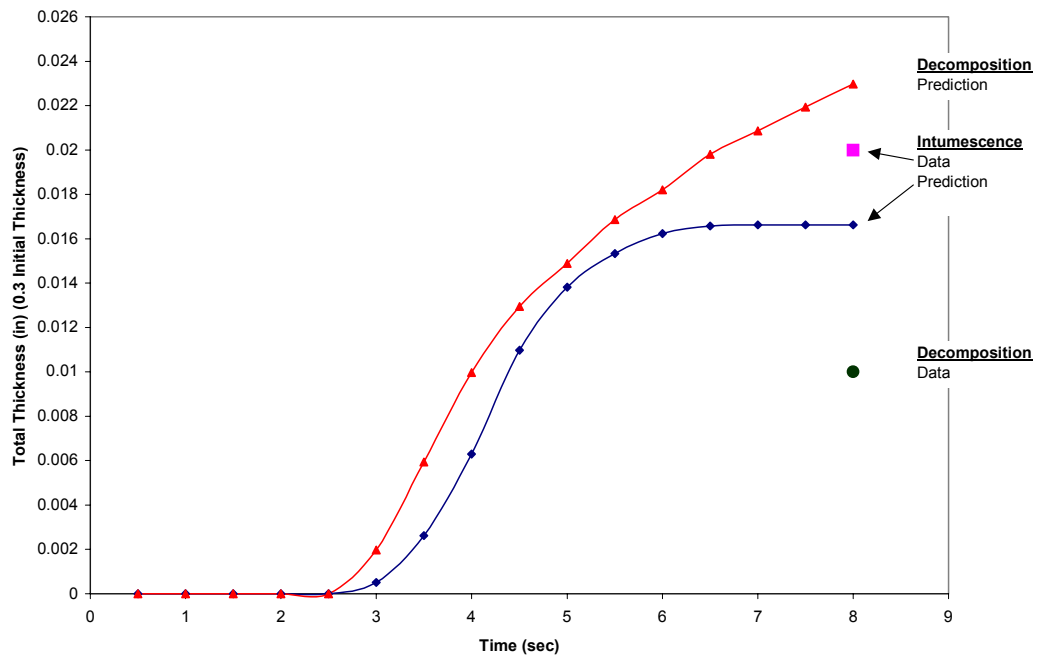


Figure 55. Intumescence and In-depth Decomposition History Predictions

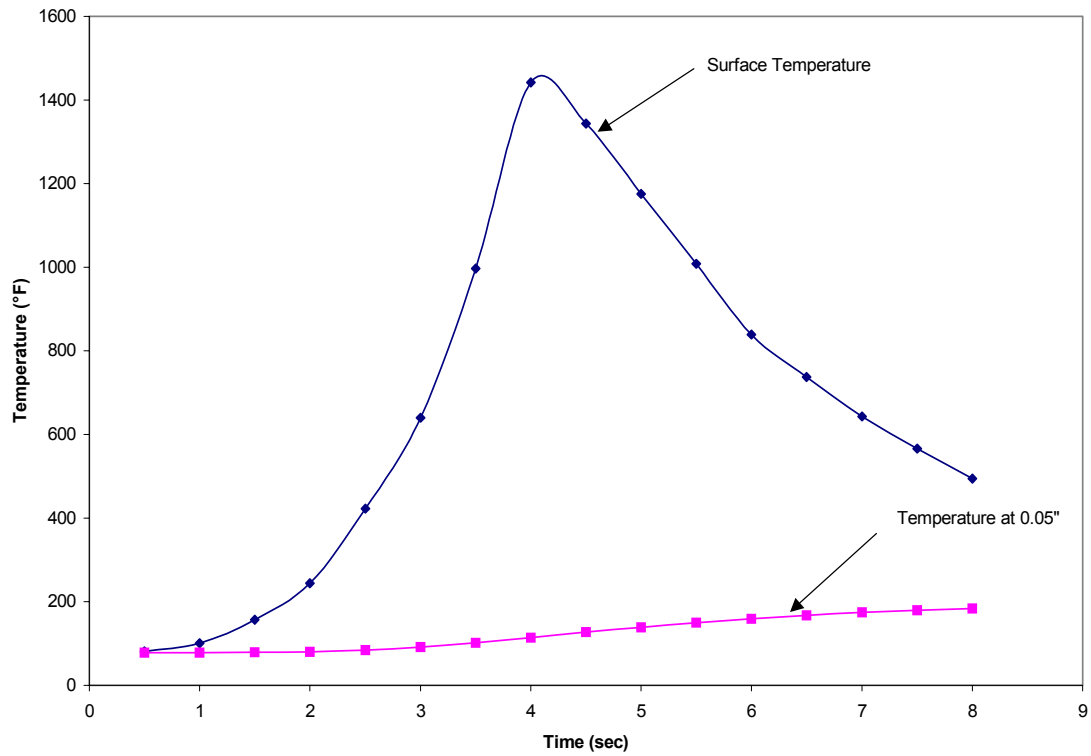


Figure 56. Sled Test Predicted Thermal Response Predictions

## **VI. SUMMARY, CONCLUSIONS, AND RECOMMENDATIONS FOR FUTURE RESEARCH**

In summary, the objective of this research was to initiate the first step of incorporating the effects of intumescence on the in-depth energy balance as defined in the CMA Computer Program. Previous methods to account for this effect on heat transfer in decomposing materials included effective thermal properties and an attempt to correlate a classical thermal expansion model. These approaches were limited because they did not attempt to model the phenomena actually occurring, but instead attempted to “lump” unmodeled phenomenon into a single term. Some of the phenomenon that must be specifically modeled includes pyrolysis gas generation, intumescence, temperature and density dependent thermal properties, and decomposition energies. The addition of modeling intumescence provided a previously unavailable ability to account for material expansion during thermochemical decomposition and its relative effect on in-depth conduction. For external thermal protection systems exposed to extreme thermal environments, a significant level of thermal performance can be attributed to the conduction path growth and resulting reduction in heat transfer to temperature critical substructures.

The intumescence model was initially derived through the use of high enthalpy aerothermal environments minimizing the aerodynamic shear contribution. These conditions induced sufficient intumescence to specifically identify the relative effects on in-depth heat transfer through the use of embedded thermocouples. Real-time radiography provided the method of validating in-depth intumescence as a function of decomposition state and heating rate. The analytic approach included a mathematical model coupled to a material property table of intumescence as a function of char state and heating rate. The resulting model was then successfully applied to a low-shear, hypersonic aerothermal environment in which significant thermal and intumescence data was previously obtained. This environment represented an application to a higher aerodynamic shear condition and provided a means to quantify the analytic model range of application. Intumescence and in-depth thermal response predictions showed very good agreement with measured data and further validated the model application to a hypersonic convective aerothermal environment. Since it was determined the phenomena appeared to be a function of both char state and heating rate, it was of interest to obtain comparisons of predictions with test data for larger aerodynamic shear environments and heating rates. To exercise the model and identify the limitations of application, two additional aerothermal environments were used to predict heatshield thermal and ablative performance. These two environments represented increasingly more severe levels of aerodynamic shear for which the model has not yet been equipped to predict. The resulting predictions did not sufficiently capture the surface erosion phenomena and corresponding in-depth decomposition. As a result of the model application to these environments, the necessity of including mechanical shear in the analytic model was evident.

Conclusions from the research and resulting analytic model development and validation suggest the initial steps toward development of a theoretical model of intumescence have been successfully completed. The analytic model provided very good agreement in both intumescence and in-depth thermal response. This suggests that the analytic model has applicability over a reasonably wide range of low-shear, high-heating environments. The research also identified the necessity to better understand the TGA data over a larger range of

temperatures and heating rates. It was determined through the use of the LHMEEL test facility that the char densities of highly decomposing materials must be characterized until no additional mass loss occurs.

The LHMEEL test conditions produced sufficient heating that the surface temperatures of the char exceeded the temperatures for which the TGA data was collected. This resulted in predictions of final char density approximately two times higher than what actually results for high temperature conditions. The conclusion drawn from this response is that kinetic decomposition coefficients derived from TGA must be developed and validated over a wide range of heating environments. However, for higher shear conditions where decomposing material is removed at lower temperatures, obtaining TGA data for a large range of temperatures is of less importance. Additionally, the research has identified a heatshield model validation process that incorporates material property measurements, test facility selection for specific phenomena, necessity of embedded thermocouples and transient density measurements, and sensitivities to certain environments. Utilization of the LHMEEL provides the fundamental transient thermophysical behavior of decomposing heatshield materials and should be considered for any thermal protection material development program. While the shear rate capability is relatively low, the in-depth thermochemical decomposition and corresponding thermal response can be accurately quantified and decoupled from external aerodynamic conditions much the same way that TGA results are decoupled when using inert gas mediums.

To develop an in-depth thermochemical decomposition model, the primary objective is to quantify the material thermodynamic behavior independent from the boundary layer gas. TGA is typically utilized in an inert medium with the assumption that pyrolysis gas is percolating from in-depth to the surface preventing the boundary layer air flow from entering into the pyrolysing region. Once a reasonable understanding of in-depth thermochemical and intumescent behavior can be developed, then surface phenomena can be incorporated into the ablation model. This surface phenomenon includes mechanical erosion of the charring material as a result of increasing aerodynamic shear. The current research indicated reasonable agreement for the LHMEEL no-shear and the NASA HGTF low-shear conditions. However, for the NAWC T-Range moderate shear and the HHSTT high-shear conditions, significant difference resulted in mass loss predictions. Since thermocouple data was not collected during these tests, in-depth thermal response cannot be verified. However, it is likely that due to the lack of accurately modeling mechanical erosion, predictions of thermal response would be inaccurate.

Current methods used for high-shear heatshield design, such as the SHOA modeling technique, are designed to provide conservative design estimates as long as experimental data is available for the specific flight environments of interest. This experimental requirement also includes time of exposure for the given environment. Through the future addition of mechanical shear modeling to the intumescence model, accurate predictions can be provided for a wide range of aerothermal environments allowing for significant improvements in design optimization.

Following is a list of recommended future research that would add significantly to the analytic modeling capability of heatshield design. The current modifications to CMA of intumescence could be utilized as the foundation for adding these capabilities.

1. Mechanical Shear

It is recommended that the ability to model mechanical shear as a function of char state, heating rate, and char strength be incorporated into the CMA analytic approach. This additional phenomenon would complete the current goal to enhance the CMA code and accommodate much of the heatshield design and optimization requirements for current supersonic and hypersonic thermal protection systems.

2. Intumescence Model Refinement

Additionally, research is recommended to refine the intumescence model. These efforts should be devoted to refining the understanding of intumescence and validating the analytic approach for a wide range of aerothermal environments. These environments should include commercial building insulation designs where a significant benefit in optimization could be realized. The LHMEI test facility should be utilized for a statistically significant number of test samples to better quantify in-depth decomposition, intumescence, and thermal response.

3. Test Facility Measurement Capabilities

- a. Real-Time Radiography

It is also recommended that research be devoted to developing real-time radiography measurement capability that can readily be adapted for use at any aerothermal test facility. This capability coupled to the use of embedded thermocouples could greatly reduce the “over design” methodology and increase system performance through optimization.

- b. Pyrolysis Gas Injection Rates and Species

Methods of quantifying pyrolysis gas injection rates and mechanical erosion rates should be developed and incorporated into aerothermal test facilities. These results could be utilized to validate the transient thermochemical decomposition and corresponding mass loss predictions for various heatshield materials. Of additional interest is the ability to measure the individual mass injection species and injection rates within the boundary layer flow as well as the resulting boundary layer thickness increase. These measurements would greatly enhance the analytic model validation and increase the model application.

- c. Transient Aerodynamic Drag and Hot Wall Effects

Coupled to the measurements and analytic model enhancements suggested above is the ability to measure aerodynamic drag on intumescent and ablating heatshields under aerodynamic heating conditions. While this was specifically addressed during the NASA HGTF aerothermal test program, this capability should be developed for higher shear and enthalpy test facilities such as the NAWC T-Range, Air Force HHSTT, Arnold Engineering Development Center (AEDC), as well as other aerothermal test facilities. This ability would provide the transient hot wall effects and external heatshield influence on the aerodynamic drag models commonly developed in cold flow wind tunnels.

## REFERENCES

1. Reynolds, R. A., Russell, G. W., and Nourse, R. W., "Ablation Performance Characterization of Thermal Protection Materials Using a Mach 4.4 Sled Test." *28th AIAA/SAE/ASME/ASEE Joint Propulsion Conference*, Nashville, TN, Paper 92-3055, 1992.
2. Rohsenow, W. M. and Hartnett, J. P., Handbook of Heat Transfer, McGraw-Hill Book Company, New York, NY, 1973, Section 16-34.
3. Russell, G.W., "Thermal Performance Evaluation of a Fiber-reinforced Epoxy Composite Using Both Simplified and Complex Modeling Techniques," Graduate Thesis, University of Alabama in Huntsville, Huntsville, AL, 1995.
4. Rembert, M., Strobel, F., Jaul, W., and Russell, G., "Thermal Protection System Development for the Navy Hypersonic Weapons Technology Program," *Tri-Service Sponsored Symposium on Advancements in Heatshield Technology*, Redstone Arsenal, AL, 2000.
5. Anon., "Aerotherm Charring Material Thermal Response and Ablation Program (CMA87S)," Acurex Report UM 87-13/ATD, Acurex Corporation, Aerotherm Division, November 1987.
6. Schlichting, Dr. H., Boundary Layer Theory, McGraw-Hill Book Company, New York, NY, 1979.
7. Rohsenow, W. M. and Hartnett, J. P., Handbook of Heat Transfer, McGraw-Hill Book Company, New York, NY, 1973, Section 3-97.
8. Reynolds, R. A., Russell, G. W., and Nourse, R. W., "Ablation Performance Characterization of Thermal Protection Materials Using a Mach 4.4 Sled Test." *28th AIAA/SAE/ASME/ASEE Joint Propulsion Conference*, Nashville, TN, Paper 92-3055, 1992.
9. Doyle, C.D., "Kinetic Analysis of Thermogravimetric Data." Journal of Applied Polymer Science, Vol. V, Issue No. 15, pp. 285-292.
10. Koo, J. H., "Thermal Characteristics Comparison of Two Fire Resistant Materials," Journal of Fire Sciences, Vol. 15, May/June 1997.
11. Shih, Y.C., Cheung, F.B., and Koo, J.H., "Theoretical Modeling of Intumescent Fire- Retardant Materials," Journal of Fire Sciences, Vol. 16, January/February 1998.
12. Chung, T.J., Continuum Mechanics, Prentice Hall, Englewood Cliffs, NJ, 1988, pp. 128-138.
13. Russell, G.W., "Thermal Performance Evaluation of a Fiber-reinforced Epoxy Composite Using Both Simplified and Complex Modeling Techniques," Graduate Thesis, University of Alabama in Huntsville, Huntsville, AL, 1995.
14. Hurwicz, H., Thermal Protection Systems, ML-TDR-64-82 (1965), p.386.
15. Chung, T.J., Continuum Mechanics, Prentice Hall, Englewood Cliffs, NJ, 1988, pp. 128-138.
16. Hurwicz, H., Thermal Protection Systems, ML-TDR-64-82 (1965), p. 387.
17. Katsikas, C.J., Ablation Handbook Entry Materials Data and Design, Technical Report AFML-TR-66-262, Air Force Materials Laboratory, Wright-Patterson AFB, OH, November 1966, pp. 68-69.

## REFERENCES (CONT)

18. Hurwicz, H., Thermal Protection Systems, ML-TDR-64-82 (1965), pp. 392-393.
19. Robert, W., Laub, B., Suchsland, K., Shimizu, A., and Chambers, J., Ramburner Internal Insulation Investigation Task I – Modeling and Computer Program, Final Report AFAPL-TR-75-109, The Marquardt Company, November 1975.
20. Laub, B., Suchsland, and K., and Shimizu, A., Appendix I - Ramburner Internal Insulation Investigation Task I – Analytical Development, Aerotherm Final Report 75-172, October 1975.
21. Anon., "Aerotherm Charring Material Thermal Response and Ablation Program (CMA87S)," Acurex Report UM 87-13/ATD, Acurex Corporation, Aerotherm Division, November 1987.
22. Reynolds, R. A., Russell, G. W., and Nourse, R. W., "Ablation Performance Characterization of Thermal Protection Materials Using a Mach 4.4 Sled Test." *28th AIAA/SAE/ASME/ASEE Joint Propulsion Conference*, Nashville, TN, Paper 92-3055, 1992.
23. Russell, G., "Limitations on the Use of Simplified Heat of Ablation Modeling Techniques," Journal of Spacecraft and Materials, Unpublished.
24. Harms, R.J., Schmidt, C.M., Hanawalt, A.J., and Schmitt, D.A., A Manual for Determining Aerodynamic Heating of High-Speed Aircraft, Volume I, Report Number 7006-3352-001, June 1959, p. 4.
25. Eckert, E. R. G., Survey of Boundary Layer Heat Transfer at High Velocities and High Temperatures, WADC Technical Report 59-624, April 1960.
26. Schlichting, Dr. H., Boundary Layer Theory, McGraw-Hill Book Company, New York, NY, 1979.
27. Goldstein, S., ed. Modern Developments in Fluid Dynamics, Oxford University Press, 1938, pp. 627-631.
28. Colburn, A.P., "A Method of Correlating Forced Convection Heat Transfer Data and a Comparison with Fluid Friction," Trans. of American Chemical Engineering, Vol. 29, 1933, pp. 174-210.
29. Nourse, R.W., "Empirical Determination of Effective Heats of Ablation for Selected Composite Materials Exposed to Hypersonic Flight," Master's Thesis, Mechanical Engineering Department, The University of Alabama at Huntsville, Huntsville, AL, 1991.
30. Murray, A., and Russell, G.W., "Coupled Aerodynamic/Thermal Analysis for Heatshields," *Tri-Service Sponsored Symposium on Advancements in Heatshield Technology Symposium*, May 2000.
31. White, Frank M., Heat Transfer, Addison-Wesley Publishing Company, Inc., Cleveland, OH, 1984.
32. USAMICOM Technical Report RD-ST-98-1, G.W. Russell, D.G. Thomas, "Thermal Environment Definition for the STINGER Block II System," October 1997.
33. Rohsenow, W. M. and Hartnett, J. P., Handbook of Heat Transfer, McGraw-Hill Book Company, New York, NY, 1973, Section 3-97.



## REFERENCES (CONT)

34. Moyer, C.B., and Rindal, R.A., "An Analysis of the Coupled Chemically Reacting Boundary Layer and Charring Ablator, Part II - Finite Difference Solution for the In-Depth Response of Charring Materials Considering Surface and Energy Balances," Aerotherm Report No. 66-7, Part II, ITEK Corporation, Vidya Division, Palo Alto, Ca, prepared for Manned Spacecraft Center Nation Aeronautics and Space Administration. NASA CR-1061, November 1987.
35. Robert, W., Laub, B., Suchsland, K., Shimizu, A., and Chambers, J., Ramburner Internal Insulation Investigation Task I – Modeling and Computer Program, Final Report AFAPL-TR-75-109, The Marquardt Company, November 1975.
36. Laub, B., Suchsland, K., and Shimizu, A., Appendix I - Ramburner Internal Insulation Investigation Task I – Analytical Development, Aerotherm Final Report 75-172, October 1975.
37. The Marquardt Company, "Ramburner Internal Insulation Investigation, Volume 1-Modeling and Computer Programs," Technical Report AFP AFAPL-TR-75-109, Volume 1, December 1975.
38. Moyer, C.B., and Rindal, R.A., "An Analysis of the Coupled Chemically Reacting Boundary Layer and Charring Ablator, Part II - Finite Difference Solution for the In-Depth Response of Charring Materials Considering Surface and Energy Balances," Aerotherm Report No. 66-7, Part II, ITEK Corporation, Vidya Division, Palo Alto, CA, prepared for Manned Spacecraft Center Nation Aeronautics and Space Administration. NASA CR-1061, p 5, November 1987.
39. Rohsenhow, W. M. and Hartnett, J. P., Handbook of Heat Transfer, McGraw-Hill Book Company, New York, NY, 1973, Section 16-39.
40. Moyer, C.B., Rindal, R.A., "An Analysis of the Coupled Chemically Reacting Boundary Layer and Charring Ablator, Part II - Finite Difference Solution for the In-Depth Response of Charring Materials Considering Surface and Energy Balances," Aerotherm Report No. 66-7, Part II, ITEK Corporation, Vidya Division, Palo Alto, CA prepared for Manned Spacecraft Center Nation Aeronautics and Space Administration. NASA CR-1061, p 7, November 1987.
41. Rohsenhow, W. M. and Hartnett, J. P., Handbook of Heat Transfer, McGraw-Hill Book Company, New York, NY, 1973, Section 16-39.
42. Rohsenhow, W. M. and Hartnett, J. P., Handbook of Heat Transfer, McGraw-Hill Book Company, New York, NY, 1973, Section 16-39.
43. Anon., "The Laser Hardened Materials Evaluation Laboratory (LHMEL) USER'S MANUAL, Lawrence Associates, Inc., Dayton, OH, January 1995.
44. Rembert, M., Strobel, F., Jaul, W., and Russell, G., "Thermal Protection System Development for the Navy Hypersonic Weapons Technology Program," *Tri-Service Sponsored Symposium on Advancements in Heatshield Technology*, Redstone Arsenal, AL, 2000.
45. The High Speed Test Track, Facilities and Capabilities," Customer Information Booklet, Munitions System Division, 3246<sup>th</sup> Test Wing, 6585<sup>th</sup> Test Group Test Track Division, Holloman Air Force Base, NM, April 1989.

## REFERENCES (CONT)

46. Perry, D., and Carr, S., Thermal Property Evaluation of Candidate Heatshield Materials, Technical Report RD-ST-92-11, U.S. Army Missile Command, Redstone Arsenal, AL, May 1992.
47. Anon., "Development of a Surface Shear Test Fixture for Intumescent and Ablating Materials," ITT Industries, Aerotherm and Propulsion Structures Directorate, U.S. Army Aviation and Missile Command, Work Performed for Naval Air Warfare Center, China Lake under the Hypersonic Weapons Technology Program, October 26, 2001.
48. Rembert, M., Strobel, F., Jaul, W., and Russell, G., "Thermal Protection System Development for the Navy Hypersonic Weapons Technology Program," *Tri-Service Sponsored Symposium on Advancements in Heatshield Technology*, Redstone Arsenal, AL, 2000.
49. Rembert, M., Strobel, F., Jaul, W., and Russell, G., "Thermal Protection System Development for the Navy Hypersonic Weapons Technology Program," *Tri-Service Sponsored Symposium on Advancements in Heatshield Technology*, Redstone Arsenal, AL, 2000.
50. Reynolds, R. A., Russell, G. W., and Nourse, R. W., "Ablation Performance Characterization of Thermal Protection Materials Using a Mach 4.4 Sled Test." *28th AIAA/SAE/ASME/ASEE Joint Propulsion Conference*, Nashville, TN, Paper 92-3055, 1992.
51. Strobel, F.A., and Kelly, R.D., "Thermal and Ablative Characterization of Duroid 5667M for ERINT Application," Final Report 88-13/ATD, Acurex Corporation, Huntsville, AL, June 1988.
52. Russell, G.W., Thermal Performance Evaluation of a Fiber-reinforced Epoxy Composite Using Both Simplified and Complex Modeling Techniques, Graduate Thesis, University of Alabama in Huntsville, AL, 1995.
53. Murray, A., and Russell, G.W., "Coupled Aeroheating/ Ablation Analysis for Missile Configurations," *32<sup>nd</sup> AIAA Thermophysics Conference and Exhibit*, June 2000.
54. Anon., "Aerotherm Charring Material Thermal Response and Ablation Program (CMA87S)," Acurex Report UM 87-13/ATD, Acurex Corporation, Aerotherm Division, November 1987.
55. Nourse, R.W. and Reynolds, R.A., Aerothermal Ablation Performance of Candidate Materials for Conical Models on Mach 5.6 Sled, Technical Report RD-ST-89-4, U.S. Army Missile Command, Redstone Arsenal, AL, August 1989.
56. Perry, D., and Carr, S., Thermal Property Evaluation of Candidate Heatshield Materials, Technical Report RD-ST-92-11, U.S. Army Missile Command, Redstone Arsenal, AL, May 1992.
57. Perry, D., and Carr, S., Thermal Property Evaluation of Candidate Heatshield Materials, Technical Report RD-ST-92-11, U.S. Army Missile Command, Redstone Arsenal, AL, May 1992.
58. Anon., "Aerotherm Chemical Equilibrium Computer Program (ACE81)," Acurex Report UM 81-11/ATD, Acurex Corporation, Aerotherm Division, August 1981.
59. Doyle, C.D., "Kinetic Analysis of Thermogravimetric Data," Journal of Applied Polymer Science, Vol V, Issue No. 15, pp 285-292.

## REFERENCES (CONCL)

60. Russell, G.W., "Kinetic Decomposition Coefficients for a Thermochemically Decomposing Epoxy Reinforced Heatshield Material," *29<sup>th</sup> AIAA/SAE/ASME/ASEE Joint Propulsion Conference and Exhibit*, Monterey, CA, Paper 93-1856, June 1993.
61. Perry, D., and Carr, S., Thermal Property Evaluation of Candidate Heatshield Materials, Technical Report RD-ST-92-11, U.S. Army Missile Command, Redstone Arsenal, AL, May 1992.
62. Differential Scanning Calorimetry (DSC) 9900 Computer/Thermal Analyzer System, Operator's Manual, E.I. Dupont Denemours & Company, 1986.
63. Laub, B., Suchsland, K., and Shimizu, A., Appendix I - Ramburner Internal Insulation Investigation Task I – Analytical Development, Aerotherm Final Report 75-172, October 1975.
64. Moyer, C.B., and Rindal, R.A., "An Analysis of the Coupled Chemically Reacting Boundary Layer and Charring Ablator, Part II - Finite Difference Solution for the In-Depth Response of Charring Materials Considering Surface and Energy Balances," Aerotherm Report No. 66-7, Part II, ITEK Corporation, Vidya Division, Palo Alto, CA, prepared for Manned Spacecraft Center Nation Aeronautics and Space Administration. NASA CR-1061, p 5, November 1987.
65. Moyer, C.B., and Rindal, R.A., "An Analysis of the Coupled Chemically Reacting Boundary Layer and Charring Ablator, Part II - Finite Difference Solution for the In-Depth Response of Charring Materials Considering Surface and Energy Balances," Aerotherm Report No. 66-7, Part II, ITEK Corporation, Vidya Division, Palo Alto, CA, prepared for Manned Spacecraft Center Nation Aeronautics and Space Administration. NASA CR-1061, p 7, November 1987.

## BIBLIOGRAPHY

1. Eckert, E. R. G., Survey of Boundary Layer Heat Transfer at High Speeds, AFL- 189, December 1961.
2. Wells, P. B., "A Method for Predicting the Thermal Response of Charring Ablation Materials," Boeing Corporation, Document Number D2-23256, June 1964.
3. White, F., M., Heat Transfer, Addison-Wesley Publishing Company, Inc., Cleveland, OH, 1984.
4. Coman, K. P., "Hypervelocity Missile (HVM) Fin and Nose Thermal Test Report," Report HVM-7R0099, LTV, Dallas, TX, June 1987.
5. Cao, CPT J. T., "Supersonic Heat Shield Test 24A-A1," Test Summary Report, 6585th Test Group, Holloman Air Force Base, NM, September 1991.
6. Nourse, R. W., "Empirical Determination of Effective Heats of Ablation for Selected Composite Materials Exposed to Hypersonic Flight," Master's Thesis, Mechanical Engineering Department, The University of Alabama at Huntsville, Huntsville, AL, 1991.
7. Kays, W. M., and Crawford, M. E., Convective Heat and Mass Transfer, Third Edition, McGraw-Hill, Inc, Princeton Road, S-1, Highstown, NJ, 1993.
8. Russell, G. W., "Evaluation of Decomposition Kinetic Coefficients for a Fiber- Reinforced Intumescent Epoxy," *29<sup>th</sup> AIAA/SAE/ASME/ASEE Joint Propulsion Conference*, Monterey, CA, Paper 93-1856, June 1993.
9. Ellis, R., and Gulick, D., Calculus with Analytic Geometry, Fifth Edition, Saunders College Publishing, Harcourt Brace College Publishers, Fort Worth, TX, 1994.
10. Digital Fortran, "Language Reference Manual," Digital Equipment Corporation, Maynard, MA, 1997.

**APPENDIX A**  
**DERIVATIONS OF IN-DEPTH ENERGY AND**  
**THERMOCHEMICAL DECOMPOSITION NUMERICAL MODEL**

## 1. In-depth Energy Differential Equations

As defined by Moyer et al. [64], the differential equation defining the in-depth energy balance is

$$\frac{\partial}{\partial \theta} (\rho h A)_y = \frac{\partial}{\partial y} \left( k A \frac{\partial T}{\partial y} \right)_\theta + \frac{\partial}{\partial y} (\dot{m}_g h_g)_\theta \quad . \quad (\text{A.1})$$

This equation will be the focus of the finite difference formulation and corresponding transformations to analytically model the thermodynamic phenomena occurring in thermochemically decomposing heatshield materials. The left side term represents the storage term with respect to the  $y$  or “global” coordinate. The first term on the right side is the conduction term and is the primary expression effected by the addition of the intumescence model. The actual node thickness is allowed to increase as a function of char state and heating rate thereby increasing conduction path and reducing overall heat flux through the node. The second term on the right side is the decomposition term. This equation is utilized subject to the boundary conditions typically encountered during aerothermal heating.

## 2. Boundary Conditions

The surface boundary conditions defined for the thermochemical decomposition model are shown in Figure A.1. This figure provides each of the terms specifically handled in the numerical scheme. The control volume is allowed to move with the receding surface as ablation/erosion occurs. The energy fluxes entering the control volume include radiation from the boundary layer, char and pyrolysis gas mass flow rate enthalpy, and all diffusive energy fluxes from the gas boundary layer. The exiting energy terms represent the conduction, reradiation, condensed phase material removal, and blowing at the surface.

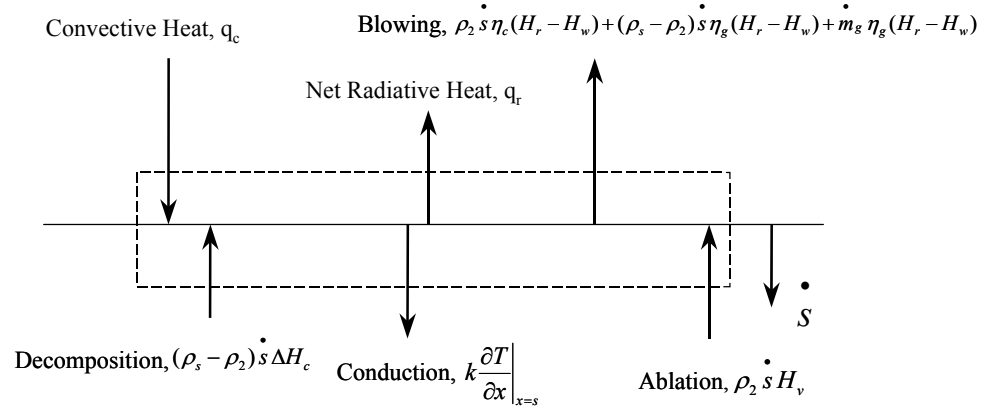


**Figure A.1. Surface Boundary Condition Schematic.**

### 3. Finite Difference Formulation

The existing mathematical model is a finite differencing scheme and requires fixed node sizes. However, for the addition of the intumescence effects, the node thickness are allowed to grow for the evaluation of conduction heat flux. To account for surface removal, nodes are removed from the backside of the ablating material such that the nodal network is “tied” to the receding surface. A transformation of the differential equations is performed from the global to body coordinates. This approach also allows for conservation of energy and mass. The difference form of the energy equation reduces to the conservation of mass equation when temperature and enthalpy are uniform. These finite difference equations are implicit in temperature. However, the decomposition finite difference forms are explicit in temperature. The decomposition nodal network is a refinement of the thermal nodal network to provide better resolution of decomposition gradients. The addition of the effects of intumescence on the in-depth energy balance are accounted for by increasing the node thickness as a function of char state and heating rate. This will specifically be identified in the following finite difference model development.

a. Geometry

The phenomenological schematic of the decomposition and ablation process is provided in Figure 2.1. Each of these parameters is defined in the finite difference equation for in-depth decomposition and surface removal.

b. Coordinate Transformation

The assumed reaction for heatshield materials is the transformation from a plastic through a pyrolysis period reaching the fully charred state due to heating and thermochemical reactions.

The mass conservation equation is

$$\left. \frac{\partial \dot{m}_g}{\partial y} \right|_{\theta} = \frac{\partial}{\partial \theta} (\rho A)_y = A \left( \frac{\partial \rho}{\partial \theta} \right)_y + \rho \left( \frac{\partial A}{\partial \theta} \right)_y . \quad (\text{A.2})$$

This relationship assumes the mass of the solid dominates the system as compared to the mass of the gas and the residence time of the pyrolysis gas in the char region is negligible. In reducing this equation to the necessary form, since  $A$  is only a function of  $y$ ,

$$\left( \rho \frac{\partial A}{\partial \theta} \right)_y = 0 , \quad (\text{A.3})$$

resulting in the expression for mass conservation

$$\left. \frac{\partial \dot{m}_g}{\partial y} \right|_{\theta} = A \left( \frac{\partial \rho}{\partial \theta} \right)_y . \quad (\text{A.4})$$



By taking the integral of Equation (A.4), the resulting relationship for total gas flow rate is

$$\dot{m}_g = - \int_y^{y_h} A \frac{\partial \rho}{\partial \theta} dy \quad . \quad (\text{A.5})$$

The expression for density can be defined in terms of a variety of reacting components combined to form the single material. Thermogravimetric Analysis (TGA) characterizes the weight loss and weight loss rate based on specific reactions occurring in the material while being heated. The general form of the expression is

$$\rho = \Gamma \sum \rho_i + (1 - \Gamma) \sum \rho_j \quad , \quad (\text{A.6})$$

where  $\Gamma$  represents the volume fraction of effective resin to effective reinforcement, the subscripts  $i$  and  $j$  represent the various reactions attributable to the resin and reinforcement densities, respectively. The general approach for using this model is to assume a three-component material where the first two components represent the first two resin reactions and the final component is the reinforcement reaction identified from TGA. However, the more general model allows for multiple components to better match the reactions occurring during decomposition. It is generally assumed that only one reinforcing component exists with multiple resin components. As a result, the last reaction identified on a TGA curve would represent the pyrolysis and charring of the reinforcing material reaching full decomposition.

The material density and density change rate due to decomposition are obtained through differentiating Equation (A.6) with respect to time and constant  $y$ .

$$\left( \frac{\partial \rho}{\partial \theta} \right)_y = \Gamma \left( \sum \frac{\partial \rho_i}{\partial \theta} \right) + (1 - \Gamma) \left( \frac{\partial \rho_j}{\partial \theta} \right)_y \quad . \quad (\text{A.7})$$

Since multiple reactions can occur during resin decomposition, a summation of the decomposition rates is used along with the assumed mass fraction ratios of resin to reinforcement. The use of an Arrhenius type fit has been found to adequately model the decomposition behavior

of thermochemically decomposing materials. The decomposition of each reaction component is given by

$$\left( \frac{\partial \rho_i}{\partial \theta} \right)_y = -k_i e^{\frac{-E_i}{RT}} \rho_{o_i} \left( \frac{\rho_i - \rho_{ir}}{\rho_{o_i}} \right)^{m_i} . \quad (\text{A.8})$$

The coordinate transformation from y to x must be performed for the decomposition. The decomposition can be expressed as a function of position and time. The derivative is then

$$d\rho = \left( \frac{\partial \rho}{\partial y} \right)_\theta dy + \left( \frac{\partial \rho}{\partial \theta} \right)_y d\theta . \quad (\text{A.9})$$

Taking the time derivative at constant x results in

$$\left( \frac{\partial \rho}{\partial \theta} \right)_x = \left( \frac{\partial \rho}{\partial y} \right)_\theta \left( \frac{\partial y}{\partial \theta} \right)_x + \left( \frac{\partial \rho}{\partial \theta} \right)_y . \quad (\text{A.10})$$

The expression relating the x and y coordinates to the surface recession is

$$y = S + x . \quad (\text{A.11})$$

Taking the partial derivative of y with respect to time at constant x gives

$$\left( \frac{\partial y}{\partial \theta} \right)_x = \frac{dS}{d\theta} \equiv \dot{S} . \quad (\text{A.12})$$

Substituting Equation (A.12) into (A.10) results in Equation (A.13), the mass conservation equation transformed from y to x coordinates.

$$\left( \frac{\partial \rho}{\partial \theta} \right)_x = \left( \frac{\partial \rho}{\partial x} \right)_\theta \dot{S} + \left( \frac{\partial \rho}{\partial \theta} \right)_y . \quad (\text{A.13})$$

The transformation of the energy conservation equation is performed with respect to a spatially fixed coordinate system assuming the following relationships:

$$h = h(T, \rho)$$

$$T = T(y, \theta)$$

$$\rho = \rho(y, \theta)$$

$$A = A(y)$$

$$S = S(\theta) \quad ,$$

resulting in the expression for enthalpy as a function of space and time

$$h = h(y, \theta) \quad .$$

The basic in-depth energy balance includes energy storage, net conduction, and convection is shown in Equation (A.1) and repeated here for convenience in Equation (A.14). This equation must be transformed to the moving coordinate system as performed for the conservation of mass equation.

$$\frac{\partial}{\partial \theta}(\rho h A)_y = \frac{\partial}{\partial y} \left( k A \frac{\partial T}{\partial y} \right)_\theta + \frac{\partial}{\partial y} (\dot{m}_g h_g)_\theta \quad . \quad (\text{A.14})$$

The first term represents the in-depth storage, the second identifies the conduction, and the third term quantifies the convection or gas flow. Expanding the first term as a function of space and time

$$\rho h A = \rho h A(y, \theta)$$

and taking the derivative, results in

$$d(\rho h A) = \frac{\partial}{\partial y}(\rho h A)_\theta dy + \frac{\partial}{\partial \theta}(\rho h A)_y d\theta \quad .$$

Taking partial derivatives with respect to time at constant x provides

$$\frac{\partial}{\partial \theta}(\rho h A)_x = \frac{\partial}{\partial y}(\rho h A)_\theta \frac{\partial y}{\partial \theta} \Big|_x + \frac{\partial}{\partial \theta}(\rho h A)_y \quad . \quad (\text{A.15})$$

Substituting Equation (A.12) into Equation (A.15) and moving terms provides

$$\frac{\partial}{\partial \theta}(\rho h A)_y = \frac{\partial}{\partial \theta}(\rho h A)_x - \dot{S} \frac{\partial}{\partial y}(\rho h A)_\theta \quad . \quad (\text{A.16})$$

Substituting Equation (A.16) into Equation (A.14) provides the transformed energy equation

$$\frac{\partial}{\partial \theta}(\rho h A)_x = \frac{\partial}{\partial x} \left( k A \frac{\partial T}{\partial x} \right)_\theta + \dot{S} \frac{\partial}{\partial x} (\rho h A)_\theta + \frac{\partial}{\partial x} \left( \dot{m}_g h_g \right)_\theta . \quad (\text{A.17})$$

Taking the first term and expanding

$$\frac{\partial}{\partial \theta}(\rho h A)_x = \rho h \frac{\partial A}{\partial \theta} + A \frac{\partial}{\partial \theta}(\rho h)_x . \quad (\text{A.18})$$

To express enthalpy change rate as a function of temperature and density change rates, a model for evaluating enthalpy is necessary. It is assumed that the pyrolysis region can be considered a mixture of pure char and pure virgin material. A volume fraction can be defined,  $\varepsilon_p$ , and varies between the undecomposed virgin material ( $\varepsilon_p=1$ ) and fully charred material ( $\varepsilon_p=0$ ). For these expressions,  $p$  represents the non-reacting material and  $c$  represents the fully charred material.

The weighted density is then defined as a function of the virgin and char densities

$$\rho = \varepsilon_p \rho_p + (1 - \varepsilon_p) \rho_c . \quad (\text{A.19})$$

The total enthalpy per unit volume is

$$\rho h = \varepsilon_p \rho_p h_p + (1 - \varepsilon_p) \rho_c h_c , \quad (\text{A.20})$$

where

$$h_p = h_p^\circ + \int_0^T C p_p dT \quad (\text{A.21})$$

and

$$h_c = h_c^\circ + \int_0^T C p_c dT . \quad (\text{A.22})$$

Differentiating Equation (A.20)

$$\frac{\partial}{\partial \theta}(\rho h) = \rho_p h_p \frac{\partial \varepsilon_p}{\partial \theta} + \rho_p \varepsilon_p \frac{\partial h_p}{\partial \theta} + \rho_c \frac{\partial h_c}{\partial \theta} - \rho h_c \frac{\partial \varepsilon_p}{\partial \theta} - \varepsilon_p \rho_c \frac{\partial h_c}{\partial \theta} . \quad (\text{A.23})$$

Differentiating Equations (A.21) and (A.22)

$$\frac{\partial h_p}{\partial \theta} = C_{p_p} \frac{\partial T}{\partial \theta} \quad (\text{A.24})$$

$$\frac{\partial h_c}{\partial \theta} = C_{p_c} \frac{\partial T}{\partial \theta} \quad (\text{A.25})$$

Solving Equation (A.19) for the volume fraction and differentiating provides Equation (A.26).

$$\frac{\partial \varepsilon_p}{\partial \theta} = \frac{1}{\rho_p - \rho_c} \frac{\partial \rho}{\partial \theta} \quad (\text{A.26})$$

Substituting Equations (A.24), (A.25), and (A.26) into Equation (A.23) provides the necessary enthalpy, temperature, and decomposition change rate relationship.

$$\frac{\partial}{\partial \theta} (\rho h)_x = \left( \frac{\rho_p h_p - \rho_c h_c}{\rho_p - \rho_c} \right) \left( \frac{\partial \rho}{\partial \theta} \right)_x + \rho C_p \left( \frac{\partial T}{\partial \theta} \right)_x, \quad (\text{A.27})$$

where

$$\rho C_p^\Delta = \rho_p \varepsilon_p C_{p_p} + (1 - \varepsilon_p) \rho_c C_{p_c} \quad (\text{A.28})$$

The mass weighted average specific heat,  $C_p$ , is used and represents the specific heat in the absence of chemical reactions. The resulting expression for the first term in Equation (A.17) is

$$\frac{\partial}{\partial \theta} (\rho h A)_x = \rho h \left( \frac{\partial A}{\partial \theta} \right)_x + A \left[ \frac{\rho_p h_p - \rho_c h_c}{\rho_p - \rho_c} \left( \frac{\partial \rho}{\partial \theta} \right)_x + \rho C_p \left( \frac{\partial T}{\partial \theta} \right)_x \right] \quad (\text{A.29})$$

The second term in Equation (A.17) does not require additional manipulation. The third term must be modified and transformed. The expanded form is

$$\dot{S} \frac{\partial}{\partial x} (\rho h A)_\theta = \dot{S} \rho h \left( \frac{\partial A}{\partial x} \right)_\theta + \dot{S} A \frac{\partial}{\partial x} (\rho h)_\theta \quad (\text{A.30})$$

Since  $A=A(y)$ ,  $y=x+S$ , and  $S=S(\theta)$ , then  $A=A(x, \theta)$ . Taking the derivative of  $A$

$$dA = \left( \frac{\partial A}{\partial x} \right)_\theta dx + \left( \frac{\partial A}{\partial \theta} \right)_x d\theta \quad (\text{A.31})$$

Taking the partial derivative with respect to time at constant  $y$  results in

$$\left. \frac{\partial A}{\partial \theta} \right)_y = \left. \frac{\partial A}{\partial x} \right)_\theta \left. \frac{\partial x}{\partial \theta} \right)_y + \left. \frac{\partial A}{\partial \theta} \right)_x . \quad (\text{A.32})$$

Since  $A=a(y)$ , then the partial of  $A$  with respect to time at constant  $y$  is zero. And since  $y=x+S$ ,

$$\left. \frac{\partial x}{\partial \theta} \right)_y = -\frac{dS}{d\theta} = -\dot{S} . \quad (\text{A.33})$$

Combining the results in Equations (A.32) and (A.33)

$$\dot{S} \left. \frac{\partial A}{\partial x} \right)_\theta = \left. \frac{\partial A}{\partial \theta} \right)_x . \quad (\text{A.34})$$

Substituting Equation (A.34) into (A.30) provides the desired expression

$$\dot{S} \frac{\partial}{\partial x} (\rho h A)_\theta = \rho h \left. \frac{\partial A}{\partial \theta} \right)_x + \dot{S} A \frac{\partial}{\partial x} (\rho h)_\theta . \quad (\text{A.35})$$

The expanded final term in Equation (A.17) is

$$\frac{\partial}{\partial x} \left( \dot{m}_g h_g \right)_\theta = \dot{m}_g \left. \frac{\partial h_g}{\partial x} \right)_\theta + h_g \left. \frac{\partial \dot{m}}{\partial x} \right)_\theta . \quad (\text{A.36})$$

Substituting Equation (A.4) into Equation (A.36) gives

$$\frac{\partial}{\partial x} \left( \dot{m}_g h_g \right)_\theta = \dot{m}_g \left. \frac{\partial h_g}{\partial x} \right)_\theta + h_g A \left. \frac{\partial \rho}{\partial \theta} \right)_y . \quad (\text{A.37})$$

Taking Equations (A.29), (A.35), and (A.37) and substituting into Equation (A.17) provides

$$\begin{aligned} \rho C_p \left. \frac{\partial T}{\partial \theta} \right)_x &= \frac{1}{A} \frac{\partial}{\partial x} \left( k A \left. \frac{\partial T}{\partial x} \right)_\theta - \bar{h} \left. \frac{\partial \rho}{\partial \theta} \right)_x + \dot{S} \frac{\partial}{\partial x} (\rho h)_\theta \right. \\ &\quad \left. + \frac{\dot{m}}{A} \left. \frac{\partial h_g}{\partial x} \right)_\theta + h_g \left. \frac{\partial \rho}{\partial \theta} \right)_y \right. , \end{aligned} \quad (\text{A.38})$$

where

$$\bar{h} = \frac{\rho_p h_p - \rho_c h_c}{\rho_p - \rho_c} \quad (A.39)$$

Equation (A.38) represents the sensible energy, net conduction, net chemical, and net convection occurring within the charring material.

Further simplifying Equation (A.38) for numerical treatment, the resulting expression is

$$\rho C_p \frac{\partial T}{\partial \theta} \Big|_x = \frac{1}{A} \frac{\partial}{\partial x} \left( kA \frac{\partial T}{\partial x} \right)_{\theta} + (h_g - \bar{h} \frac{\partial \rho}{\partial \theta})_y + \dot{S} \rho C_p \frac{\partial T}{\partial x} \Big|_{\theta} + \frac{\dot{m}}{A} \frac{\partial h_g}{\partial x} \Big|_{\theta} \quad (A.40)$$

### c. Finite Difference Relationships

Moyer et al. [65] provide a detailed discussion of the finite difference equation development. Only the pertinent expressions are provided in the following.

#### 1. Mass Equation

In-depth nodes

Decomposition Nodelet Density Change Rate

$$\frac{\rho'_{n,j} - \rho_{n,j}}{\Delta \theta} = \dot{S} \frac{\rho_{n,j+1} - \rho_{n,1}}{\delta_{n,j}} + \left( \frac{\partial \rho_{n,j}}{\partial \theta} \right)_d \quad (A.41)$$

Thermal Solution for Nodelet Temperatures

$$T_{n,j} = T_{n-1} + \frac{T_n - T_{n-1}}{\frac{1}{2}(A_n \delta_n + A_{n-1} \delta_{n-1})} \left[ \frac{(A_{n-1} \delta_{n-1})}{2} + (j - 0.5) \frac{A_n \delta_n}{J} \right] \text{ for } j \leq J/2 \quad (A.42)$$

$$T_{n,j} = T_n + \frac{T_{n+1} - T_n}{\frac{1}{2}(A_{n+1} \delta_{n+1} + A_n \delta_n)} \left[ \frac{(j - 0.5)}{J} - 0.5 \right] A_n \delta_n \text{ for } j > J/2 \quad (A.43)$$

Nodelet Density Change Rate of Constituent  $i$

$$\left( \frac{\partial \rho_{i,n,j}}{\partial \theta} \right)_D = -k_i e^{\frac{-E_i}{RT_{n,j}}} \rho_{o_i} \left( \frac{\rho_{i,n,j} - \rho_{r_i}}{\rho_{o_i}} \right)^{m_i} \quad (\text{A.44})$$

$$\left( \frac{\partial \rho_{i,n,j}}{\partial \theta} \right)_D = \left( \frac{\rho'_{i,n,j} - \rho_{i,n,j}}{\Delta \theta} \right)_y = \frac{\rho_{r_i} - \rho_{i,n,j} + \left[ (\rho_{i,n,j} - \rho_{r_i})^{(1-m_i)} - \frac{1-m_i}{\rho_{o_i}^{(m_i-1)}} k_i e^{\frac{-E_i}{RT_{n,j}}} \Delta \theta \right]^{\left( \frac{1}{1-m_i} \right)}}{\Delta \theta} \quad \text{for } m_i \neq 1 \quad (\text{A.45})$$

$$\left( \frac{\partial \rho_{i,n,j}}{\partial \theta} \right)_D = \left( \frac{\rho_{i,n,j} - \rho_{r_i}}{\Delta \theta} \right) \left[ \exp \left( -k_i e^{\frac{-E_i}{RT_{n,j}}} \Delta \theta \right) - 1 \right] \quad \text{for } m_i = 1 \quad (\text{A.46})$$

$$\frac{\rho'_n - \rho_n}{\Delta \theta} = \dot{S} \frac{\rho_{n+1,1} - \rho_{n,1}}{\delta_n} + \frac{1}{J} \sum \left( \frac{\partial \rho_{n,j}}{\partial \theta} \right)_d \quad (\text{A.47})$$

Surface Node

The surface node is treated as a half node using the above expressions and assigning half as many nodelets.

Last ablating node

The last ablating node requires special treatment due to the variation of stationary and moving coordinate systems from the front to the back of the node. Remembering that erosion/ablation from the surface is accounted for at the back node, the back surface of the last node is considered stationary and the front of the node is removed. As a result, Equation (A.12) must take the form of



$$\left. \frac{\partial y}{\partial \theta} \right)_{x,j} = \dot{S} \frac{J-j}{J} \quad (1 < j < J) \quad . \quad (\text{A.48})$$

The resulting modified mass balance is

$$\frac{d\rho_{N,j}}{d\theta} = \left( \frac{\partial \rho_{N,j}}{\partial \theta} \right)_d + \frac{\dot{S}}{\delta_{N,j}} \frac{J-j}{J} (\rho_{N,j+1} - \rho_{N,j}) \quad (\text{A.49})$$

$$\frac{d\rho_{N,j}}{d\theta} = \frac{1}{J} \sum_{j=1}^J \left( \frac{\partial \rho_{N,j}}{\partial \theta} \right)_d + \frac{\dot{S}}{J\delta_N} \sum_{j=1}^J (J-j)(\rho_{N,j+1} - \rho_{N,j}) \quad (\text{A.50})$$

$$\frac{d\rho_{N,j}}{d\theta} = \frac{1}{J} \sum_{j=1}^J \left( \frac{\partial \rho_{N,j}}{\partial \theta} \right)_d + \frac{\dot{S}}{\delta_N} (\rho_N - \rho_{N,1}) \quad . \quad (\text{A.51})$$

## 2. Energy Equation

$$\frac{\partial}{\partial \theta} (\rho h)_x = \rho C_p \left( \frac{\partial T}{\partial \theta} \right)_x + \bar{h} \left( \frac{\partial \rho}{\partial \theta} \right)_x = \rho' C_p \frac{\Delta T}{\Delta \theta} + \bar{h} \frac{\Delta \rho}{\Delta \theta} \quad (\text{A.52})$$

Since enthalpy is a function of temperature and density only, it is acceptable to solve Equation (A.52) in two steps. The first step is to solve the density change for a constant temperature followed by solving the temperature field for a constant density. The density change equation is defined as

$$\begin{aligned} (\rho' C_p)_n (T'_n - T_n) = & \frac{\Delta \theta}{\delta_n A_n} \left( \frac{\frac{T_{n-1} - T_n}{\frac{\delta_{n-1}}{2} + \frac{\delta_n}{2}} - \frac{T_n - T_{n+1}}{\frac{\delta_n}{2} + \frac{\delta_{n+1}}{2}}}{\frac{k_{n-1} A_{n-1}}{k_n A_n}} \right) + \\ & \left\{ h_{g_n} \left( \frac{\partial \rho_n}{\partial \theta} \right)_d - \bar{h} \frac{\Delta \rho_n}{\Delta \theta} + \frac{\dot{m}_{g_n}}{A_n} \frac{h_{g_{n+1}} - h_{g_n}}{\delta_n} + \frac{\dot{S}}{\delta_n} [(\rho h)_{T_{n+1}, \rho_{n+1,1}} - (\rho h)_{T_n, \rho_{n,1}}] \right\} \Delta \theta . \end{aligned} \quad (\text{A.53})$$

The intumescence effects are accounted for in the temperature change equations. The approach is to increase the node thickness at each time step based on char state and heating rate dependencies. This modification to the original approach is made in the variability of the  $\delta$  values in the conduction term or first term on right side of Equation (A.54).

$$\begin{aligned}
 (\rho' \bar{C}_p)_n (T'_n - T_n) = & \frac{\Delta \theta}{\delta_n A'_n} \left( \frac{T'_{n-1} - T'_n}{\frac{\delta_{n-1}/2}{k_{n-1} A'_{n-1}} + \frac{\delta_n/2}{k_n A'_n}} - \frac{T'_n - T'_{n+1}}{\frac{\delta_n/2}{k_n A'_n} + \frac{\delta_{n+1}/2}{k_{n+1} A'_{n+1}}} \right) + \\
 & \left\{ \left[ h_{g_n} + \left( \frac{\partial h_g}{\partial T} \right)_n (T'_n - T_n) \right] \left( \frac{\partial \rho_n}{\partial \theta} \right)_d - \bar{h}_n \left( \frac{\Delta \rho}{\Delta \theta} \right)_n + \right. \\
 & \left. \frac{\dot{m}_{g_n}}{A'_n} \left[ \frac{h_{g_{n+1}} + \left( \frac{\partial h_g}{\partial T} \right)_{n+1} (T'_{n+1} - T_{n+1}) - h_{g_n} - \left( \frac{\partial h_g}{\partial T} \right)_n (T'_n - T_n)}{\delta_n} \right] + \right. \\
 & \left. \frac{\dot{S}}{\delta_n} \left[ (\rho h)_{n+1,1} + (\rho C_p)_{n+1,1} (T'_{n+1} - T_{n+1}) - (\rho h)_{n,1} - (\rho C_p)_{n,1} (T'_n - T_n) \right] \right\} \Delta \theta,
 \end{aligned} \tag{A.54}$$

Where primed values are taken at

$$\theta' = \theta + \Delta \theta \quad . \tag{A.55}$$

Surface Node

$$\begin{aligned}
 (\rho' \bar{C}_p)_1 (T'_n - T_1) &= \frac{\Delta \theta}{\delta_1 A'_1} \left( q_{cond} - \frac{T'_1 - T'_2}{\frac{\delta_1}{k_1 A'_1} + \frac{\delta_2}{k_2 A'_2}} \right) + \\
 \Delta \theta &\left\{ \left[ h_{g_1} + \left( \frac{\partial h_g}{\partial T} \right)_1 (T'_1 - T_1) \right] \left( \frac{\partial \rho_1}{\partial \theta} \right)_d - \bar{h}_1 \left( \frac{\Delta \rho}{\Delta \theta} \right)_1 + \right. \\
 \frac{\dot{m}_{g_1}}{A'_1} &\left[ h_{g_2} + \left( \frac{\partial h_g}{\partial T} \right)_2 (T'_2 - T_1) - h_{g_1} - \left( \frac{\partial h_g}{\partial T} \right)_2 (T'_1 - T_1) \right] + \\
 \frac{\dot{S}}{\delta_1} &\left[ (\rho h)_{2,1} + (\rho C_p)_{2,1} (T'_2 - T_2) - (\rho h)_1 - (\rho C_p)_1 (T'_1 - T_1) \right] \Big\}
 \end{aligned} \tag{A.58}$$

Last Ablating Node

$$\begin{aligned}
 (\rho' \bar{C}_p)_n (T'_n - T_n) &= \frac{2 \Delta \theta}{\delta_n A'_n} \left( \frac{T'_{n-1} - T'_n}{\frac{\delta_{n-1}}{k_{n-1} A'_{n-1}} + \frac{\delta_n}{k_n A'_n}} - \frac{T'_n - T'_{n+1}}{\frac{\delta_n}{k_n A'_n} + \frac{\delta_{n+1}}{k_{n+1} A'_{n+1}}} \right) + \\
 \Delta \theta &\left\{ \left[ h_{g_n} + \left( \frac{\partial h_g}{\partial T} \right)_n (T'_n - T_n) \right] \left( \frac{\partial \rho_n}{\partial \theta} \right)_d \right\} - \bar{h}_n (\Delta \rho)_n + \\
 \frac{S \dot{\Delta} \theta}{\delta_n} &\left[ (\rho h)_n + (\rho C_p)_n (T'_n - T_n) - (\rho h)_{n,1} - (\rho C_p)_{n,1} (T'_n - T_n) \right]
 \end{aligned} \tag{A.56}$$

**APPENDIX B**  
**EXAMPLE CMA INPUT DECK**

3 Check case for expansion model to compare in depth conduction  
 using semi-infinite insulator conductor 0.4" thickness  
 using properties derived from shear and phase 1 tests  
 BCs and low conductivity metal 75 w/cm2

# MISCELLANEOUS FLAGS AND CONSTANTS

0	0	0	0						icntr,ivac,ncon,nfis,ipgprs
1	0	0	0	1	0	0			nn,ieffp,ihtcf,itga,nopt1,nr,nst
0.0	45.	1.							thzro,thfin,dthb
-2451.0	-1781.0		0.000		536.400				HTS OF FORM,TZ
0.00000	0.000		536.0						BACKWALL HCONV,EPSW,TRES
0.000200	0.0		0.00000						DELM,RA(1),RA(2)
0.150000	0.850000		0.00000		0.00000				CHCRI,PYCRI,BREX,SWELL
0.0	1.0	0.4	0.0						cmhs,vfz,brp,crtdden
10	3	0	0	0					JF,NO,NI,NFFUNC,NDBU
0.05	0.15	0.25	.50000		10.0000				TIMESTEPS
-5.00000		45.0000							TIMESTEPS

# KINETIC DATA

2

4

.9	77.16	85.56							
.1997	0.001	46.1717		2.4		7104.537	530.0		'RX 1'
.1278	0.001	26798.3		4.5		9059.131	530.0		'RX 2'
.1574	0.001	6.9798e+12		4.3		40765.202	530.0		'RX 3'
.5151	0.295	3.7482e+10		3.0		28535.486	530.0		'RX 4'

# NODAL DATA

1	538.3	0.0	.0005	0.0	0.001	in thick
1	538.3	0.0	.001	0.0	0.0015	in thick
1	538.3	0.0	.001	0.0	0.0025	in thick
1	538.3	0.0	.001	0.0	0.0035	in thick
1	538.3	0.0	.001	0.0	0.0045	in thick
1	538.3	0.0	.001	0.0	0.0055	in thick
1	538.3	0.0	.001	0.0	0.0065	in thick
1	538.3	0.0	.001	0.0	0.0075	in thick
1	538.3	0.0	.001	0.0	0.0085	in thick
1	538.3	0.0	.0015	0.0	0.010	in thick
1	538.3	0.0	.002	0.0	0.012	in thick
1	538.3	0.0	.002	0.0	0.014	in thick
1	538.3	0.0	.002	0.0	0.016	in thick
1	538.3	0.0	.002	0.0	0.018	in thick
1	538.3	0.0	.002	0.0	0.020	in thick
1	538.3	0.0	.002	0.0	0.022	in thick
1	538.3	0.0	.002	0.0	0.024	in thick
1	538.3	0.0	.002	0.0	0.026	in thick
1	538.3	0.0	.002	0.0	0.028	in thick
1	538.3	0.0	.002	0.0	0.030	in thick
1	538.3	0.0	.002	0.0	0.032	in thick
1	538.3	0.0	.002	0.0	0.034	in thick
1	538.3	0.0	.002	0.0	0.036	in thick
1	538.3	0.0	.002	0.0	0.038	in thick
1	538.3	0.0	.002	0.0	0.040	in thick
1	538.3	0.0	.002	0.0	0.042	in thick
1	538.3	0.0	.002	0.0	0.044	in thick
1	538.3	0.0	.002	0.0	0.046	in thick
1	538.3	0.0	.002	0.0	0.048	in thick
1	538.3	0.0	.002	0.0	0.050	in thick
1	538.3	0.0	.002	0.0	0.052	in thick
1	538.3	0.0	.002	0.0	0.054	in thick
1	538.3	0.0	.002	0.0	0.056	in thick
1	538.3	0.0	.002	0.0	0.058	in thick
1	538.3	0.0	.002	0.0	0.060	in thick

1	538.3	0.0	.005	0.0	0.065	in thick
1	538.3	0.0	.005	0.0	0.070	in thick
1	538.3	0.0	.005	0.0	0.075	in thick
1	538.3	0.0	.005	0.0	0.080	in thick
1	538.3	0.0	.005	0.0	0.085	in thick
1	538.3	0.0	.005	0.0	0.090	in thick
1	538.3	0.0	.005	0.0	0.095	in thick
1	538.3	0.0	.005	0.0	0.100	in thick
1	538.3	0.0	.005	0.0	0.105	in thick
1	538.3	0.0	.005	0.0	0.110	in thick
1	538.3	0.0	.005	0.0	0.115	in thick
1	538.3	0.0	.005	0.0	0.120	in thick
1	538.3	0.0	.005	0.0	0.125	in thick
1	538.3	0.0	.005	0.0	0.130	in thick
1	538.3	0.0	.005	0.0	0.135	in thick
1	538.3	0.0	.005	0.0	0.140	in thick
1	538.3	0.0	.005	0.0	0.145	in thick
1	538.3	0.0	.005	0.0	0.150	in thick
1	538.3	0.0	.005	0.0	0.155	in thick
1	538.3	0.0	.005	0.0	0.160	in thick
1	538.3	0.0	.005	0.0	0.165	in thick
1	538.3	0.0	.005	0.0	0.170	in thick
1	538.3	0.0	.005	0.0	0.175	in thick
1	538.3	0.0	.005	0.0	0.180	in thick
1	538.3	0.0	.005	0.0	0.185	in thick
1	538.3	0.0	.005	0.0	0.190	in thick
1	538.3	0.0	.005	0.0	0.195	in thick
1	538.3	0.0	.005	0.0	0.200	in thick
1	538.3	0.0	.005	0.0	0.205	in thick
1	538.3	0.0	.005	0.0	0.210	in thick
1	538.3	0.0	.005	0.0	0.215	in thick
1	538.3	0.0	.005	0.0	0.220	in thick
1	538.3	0.0	.005	0.0	0.225	in thick
1	538.3	0.0	.005	0.0	0.230	in thick
1	538.3	0.0	.005	0.0	0.235	in thick
1	538.3	0.0	.005	0.0	0.240	in thick
1	538.3	0.0	.005	0.0	0.245	in thick
1	538.3	0.0	.005	0.0	0.250	in thick
1	538.3	0.0	.010	0.0	0.260	in thick
1	538.3	0.0	.010	0.0	0.270	in thick
1	538.3	0.0	.010	0.0	0.280	in thick
1	538.3	0.0	.010	0.0	0.290	in thick
1	538.3	0.0	.010	0.0	0.300	in thick
1	538.3	0.0	.010	0.0	0.310	in thick
1	538.3	0.0	.010	0.0	0.320	in thick
1	538.3	0.0	.010	0.0	0.330	in thick
1	538.3	0.0	.010	0.0	0.340	in thick
1	538.3	0.0	.010	0.0	0.350	in thick
1	538.3	0.0	.010	0.0	0.360	in thick
1	538.3	0.0	.010	0.0	0.370	in thick
1	538.3	0.0	.010	0.0	0.380	in thick
1	538.3	0.0	.010	0.0	0.390	in thick
-1	538.3	0.0	.010	0.0	0.400	in thick

MATERIAL TABLES

530.0	0.36	5.28E-05	0.9	0.9
546.0	0.36	5.28E-05	0.9	0.9
555.0	0.36	5.28E-05	0.9	0.9
564.0	0.36	5.28E-05	0.9	0.9
573.0	0.36	5.28E-05	0.9	0.9
580.0	0.36	5.28E-05	0.9	0.9

591.0	0.36	5.28E-05	0.9	0.9
600.0	0.36	5.28E-05	0.9	0.9
610.0	0.36	5.00E-05	0.9	0.9
620.0	0.36	4.72E-05	0.9	0.9
635.0	0.36	4.44E-05	0.9	0.9
672.0	0.38	3.89E-05	0.9	0.9
760.0	0.38	3.33E-05	0.9	0.9
1060.0	0.38	2.50E-05	0.9	0.9
1360.0	0.39	2.22E-05	0.9	0.9
1460.0	0.4	1.67E-05	0.9	0.9
1960.0	0.41	1.67E-05	0.9	0.9
2460.0	0.42	1.94E-05	0.9	0.9
2960.0	0.44	2.50E-05	0.9	0.9
-3460.0	0.48	2.50E-05	0.9	0.9
512.0	0.318	2.78E-05	0.9	0.9
592.0	0.263	2.78E-05	0.9	0.9
672.0	0.287	2.78E-05	0.9	0.9
762.0	0.295	2.78E-05	0.9	0.9
852.0	0.31	2.78E-05	0.9	0.9
1032.0	0.311	3.33E-05	0.9	0.9
1122.0	0.318	3.33E-05	0.9	0.9
1212.0	0.326	3.61E-05	0.9	0.9
1302.0	0.335	3.61E-05	0.9	0.9
1392.0	0.35	3.89E-05	0.9	0.9
1572.0	0.36	3.89E-05	0.9	0.9
1752.0	0.38	4.44E-05	0.9	0.9
1932.0	0.4	4.44E-05	0.9	0.9
2292.0	0.47	5.00E-05	0.9	0.9
-3460.0	0.48	5.00E-05	0.9	0.9

# PYROLYSIS GAS ENTHALPY TABLES

2 0.03 1.0

460.0	-2850.	-2850.
560.0	-2800.	-2800.
743.0	-2003.	-2003.
1355.0	-1159.	-1159.
1555.0	-1040.	-1040.
-2000.0	-1040.	-1040.

# BOUNDARY CONDITIONS

0.000	1.0	66.0	0.0	1.0	0.0
45.000	1.0	66.0	0.0	1.0	0.0
46.00	1.0	0.0	0.0	1.0	0.0
-100.00	1.0	0.0	0.0	1.0	0.0

# SURFACE THERMOCHEMISTRY TABLES

1.00000	0.00010	0.200011166.66670.000	229.556	229.556	1	RX2390
1.00000	0.00010	0.100011083.33340.000	206.038	206.038	1	RX2390
1.00000	0.00010	0.000011055.55550.000	198.244	198.244	0	CHAR
1.00000	0.00010	0.000011000.00000.000	182.740	182.740	0	CHAR
1.00000	0.00010	0.00001 944.44450.000	167.354	167.354	0	CHAR
1.00000	0.00010	0.00001 888.88890.000	152.088	152.088	0	CHAR
1.00000	0.00010	0.00001 833.33340.000	136.953	136.953	0	CHAR
1.00000	0.00010	0.00001 777.77780.000	121.966	121.966	0	CHAR
1.00000	0.00010	0.00001 722.22220.000	107.260	107.260	0	CHAR
1.00000	0.00010	0.00001 666.66670.000	92.746	92.746	0	CHAR
1.00000	0.00010	0.00001 611.11110.000	78.232	78.232	0	CHAR
1.00000	0.00010	0.00001 555.55550.000	64.297	64.297	0	CHAR
1.00000	0.00010	0.00001 416.66670.000	29.629	29.629	0	CHAR
1.00000	0.00010	0.00001 297.77780.000	-0.156	-0.156	0	CHAR
1.00000	0.00040	0.200011166.66670.000	229.314	229.314	1	RX2390
1.00000	0.00040	0.100011083.33340.000	205.803	205.803	1	RX2390
1.00000	0.00040	0.000011055.55550.000	198.011	198.011	0	CHAR

1.00000	0.00040	0.00001	1000.00000.000	182.512	182.512	0	CHAR
1.00000	0.00040	0.00001	944.44450.000	167.131	167.131	0	CHAR
1.00000	0.00040	0.00001	888.88890.000	151.869	151.869	0	CHAR
1.00000	0.00040	0.00001	833.33340.000	136.735	136.735	0	CHAR
1.00000	0.00040	0.00001	777.77780.000	121.741	121.741	0	CHAR
1.00000	0.00040	0.00001	722.22220.000	107.022	107.022	0	CHAR
1.00000	0.00040	0.00001	666.66670.000	92.489	92.489	0	CHAR
1.00000	0.00040	0.00001	611.11110.000	77.957	77.957	0	CHAR
1.00000	0.00040	0.00001	555.55550.000	64.003	64.003	0	CHAR
1.00000	0.00040	0.00001	416.66670.000	29.252	29.252	0	CHAR
1.00000	0.00040	0.00001	297.77780.000	-0.625	-0.625	0	CHAR
1.00000	0.00100	0.20001	1166.66670.000	228.830	228.830	1	RX2390
1.00000	0.00100	0.10001	1083.33340.000	205.334	205.334	1	RX2390
1.00000	0.00100	0.00001	1055.55550.000	197.546	197.546	0	CHAR
1.00000	0.00100	0.00001	1000.00000.000	182.056	182.056	0	CHAR
1.00000	0.00100	0.00001	944.44450.000	166.684	166.684	0	CHAR
1.00000	0.00100	0.00001	888.88890.000	151.432	151.432	0	CHAR
1.00000	0.00100	0.00001	833.33340.000	136.299	136.299	0	CHAR
1.00000	0.00100	0.00001	777.77780.000	121.290	121.290	0	CHAR
1.00000	0.00100	0.00001	722.22220.000	106.546	106.546	0	CHAR
1.00000	0.00100	0.00001	666.66670.000	91.977	91.977	0	CHAR
1.00000	0.00100	0.00001	611.11110.000	77.407	77.407	0	CHAR
1.00000	0.00100	0.00001	555.55550.000	63.416	63.416	0	CHAR
1.00000	0.00100	0.00001	416.66670.000	28.499	28.499	0	CHAR
1.00000	0.00100	0.00001	297.77780.000	-1.561	-1.561	0	CHAR
1.00000	0.00400	0.20001	1166.66670.000	226.420	226.420	1	RX2390
1.00000	0.00400	0.10001	1083.33340.000	202.994	202.994	1	RX2390
1.00000	0.00400	0.00001	1055.55550.000	195.230	195.230	0	CHAR
1.00000	0.00400	0.00001	1000.00000.000	179.786	179.786	0	CHAR
1.00000	0.00400	0.00001	944.44450.000	164.460	164.460	0	CHAR
1.00000	0.00400	0.00001	888.88890.000	149.253	149.253	0	CHAR
1.00000	0.00400	0.00001	833.33340.000	134.128	134.128	0	CHAR
1.00000	0.00400	0.00001	777.77780.000	119.045	119.045	0	CHAR
1.00000	0.00400	0.00001	722.22220.000	104.178	104.178	0	CHAR
1.00000	0.00400	0.00001	666.66670.000	89.423	89.423	0	CHAR
1.00000	0.00400	0.00001	611.11110.000	74.668	74.668	0	CHAR
1.00000	0.00400	0.00001	555.55550.000	60.489	60.489	0	CHAR
1.00000	0.00400	0.00001	416.66670.000	24.746	24.746	0	CHAR
1.00000	0.00400	0.00001	297.77780.000	-6.224	-6.224	0	CHAR
1.00000	0.00600	0.20001	1166.66670.000	224.821	224.821	1	RX2390
1.00000	0.00600	0.10001	1083.33340.000	201.442	201.442	1	RX2390
1.00000	0.00600	0.00001	1055.55550.000	193.693	193.693	0	CHAR
1.00000	0.00600	0.00001	1000.00000.000	178.280	178.280	0	CHAR
1.00000	0.00600	0.00001	944.44450.000	162.984	162.984	0	CHAR
1.00000	0.00600	0.00001	888.88890.000	147.808	147.808	0	CHAR
1.00000	0.00600	0.00001	833.33340.000	132.687	132.687	0	CHAR
1.00000	0.00600	0.00001	777.77780.000	117.556	117.556	0	CHAR
1.00000	0.00600	0.00001	722.22220.000	102.607	102.607	0	CHAR
1.00000	0.00600	0.00001	666.66670.000	87.729	87.729	0	CHAR
1.00000	0.00600	0.00001	611.11110.000	72.851	72.851	0	CHAR
1.00000	0.00600	0.00001	555.55550.000	58.548	58.548	0	CHAR
1.00000	0.00600	0.00001	416.66670.000	22.257	22.257	0	CHAR
1.00000	0.00600	0.00001	297.77780.000	-9.317	-9.317	0	CHAR
1.00000	0.00800	0.20001	1166.66670.000	223.229	223.229	1	RX2390
1.00000	0.00800	0.10001	1083.33340.000	199.895	199.895	1	RX2390
1.00000	0.00800	0.00001	1055.55550.000	192.162	192.162	0	CHAR
1.00000	0.00800	0.00001	1000.00000.000	176.780	176.780	0	CHAR
1.00000	0.00800	0.00001	944.44450.000	161.514	161.514	0	CHAR
1.00000	0.00800	0.00001	888.88890.000	146.368	146.368	0	CHAR
1.00000	0.00800	0.00001	833.33340.000	131.252	131.252	0	CHAR



1.00000	0.00800	0.00001	777.77780.000	116.073	116.073	0	CHAR
1.00000	0.00800	0.00001	722.22220.000	101.042	101.042	0	CHAR
1.00000	0.00800	0.00001	666.66670.000	86.042	86.042	0	CHAR
1.00000	0.00800	0.00001	611.11110.000	71.041	71.041	0	CHAR
1.00000	0.00800	0.00001	555.55550.000	56.615	56.615	0	CHAR
1.00000	0.00800	0.00001	416.66670.000	19.778	19.778	0	CHAR
1.00000	0.00800	0.00001	297.77780.000	-12.399	-12.399	0	CHAR
1.00000	0.02000	0.20001	1166.66670.000	213.805	213.805	1	RX2390
1.00000	0.02000	0.10001	1083.33340.000	190.746	190.746	1	RX2390
1.00000	0.02000	0.00001	1055.55550.000	183.104	183.104	0	CHAR
1.00000	0.02000	0.00001	1000.00000.000	167.903	167.903	0	CHAR
1.00000	0.02000	0.00001	944.44450.000	152.817	152.817	0	CHAR
1.00000	0.02000	0.00001	888.88890.000	137.849	137.849	0	CHAR
1.00000	0.02000	0.00001	833.33340.000	122.762	122.762	0	CHAR
1.00000	0.02000	0.00001	777.77780.000	107.296	107.296	0	CHAR
1.00000	0.02000	0.00001	722.22220.000	91.783	91.783	0	CHAR
1.00000	0.02000	0.00001	666.66670.000	76.057	76.057	0	CHAR
1.00000	0.02000	0.00001	611.11110.000	60.332	60.332	0	CHAR
1.00000	0.02000	0.00001	555.55550.000	45.174	45.174	0	CHAR
1.00000	0.02000	0.00001	416.66670.000	5.107	5.107	0	CHAR
1.00000	0.02000	0.00001	297.77780.000	-30.632	-30.632	0	CHAR
1.00000	0.04000	0.20001	1166.66670.000	198.582	198.582	1	RX2390
1.00000	0.04000	0.10001	1083.33340.000	175.967	175.967	1	RX2390
1.00000	0.04000	0.00001	1055.55550.000	168.472	168.472	0	CHAR
1.00000	0.04000	0.00001	1000.00000.000	153.563	153.563	0	CHAR
1.00000	0.04000	0.00001	944.44450.000	138.767	138.767	0	CHAR
1.00000	0.04000	0.00001	888.88890.000	124.087	124.087	0	CHAR
1.00000	0.04000	0.00001	833.33340.000	109.046	109.046	0	CHAR
1.00000	0.04000	0.00001	777.77780.000	93.117	93.117	0	CHAR
1.00000	0.04000	0.00001	722.22220.000	76.825	76.825	0	CHAR
1.00000	0.04000	0.00001	666.66670.000	59.928	59.928	0	CHAR
1.00000	0.04000	0.00001	611.11110.000	43.032	43.032	0	CHAR
1.00000	0.04000	0.00001	555.55550.000	26.692	26.692	0	CHAR
1.00000	0.04000	0.00001	416.66670.000	-18.593	-18.593	0	CHAR
1.00000	0.04000	0.00001	297.77780.000	-60.085	-60.085	0	CHAR
1.00000	0.05000	0.20001	1166.66670.000	191.188	191.188	1	RX2390
1.00000	0.05000	0.10001	1083.33340.000	168.789	168.789	1	RX2390
1.00000	0.05000	0.00001	1055.55550.000	161.365	161.365	0	CHAR
1.00000	0.05000	0.00001	1000.00000.000	146.597	146.597	0	CHAR
1.00000	0.05000	0.00001	944.44450.000	131.943	131.943	0	CHAR
1.00000	0.05000	0.00001	888.88890.000	117.402	117.402	0	CHAR
1.00000	0.05000	0.00001	833.33340.000	102.384	102.384	0	CHAR
1.00000	0.05000	0.00001	777.77780.000	86.230	86.230	0	CHAR
1.00000	0.05000	0.00001	722.22220.000	69.560	69.560	0	CHAR
1.00000	0.05000	0.00001	666.66670.000	52.094	52.094	0	CHAR
1.00000	0.05000	0.00001	611.11110.000	34.629	34.629	0	CHAR
1.00000	0.05000	0.00001	555.55550.000	17.715	17.715	0	CHAR
1.00000	0.05000	0.00001	416.66670.000	-30.104	-30.104	0	CHAR
1.00000	0.05000	0.00001	297.77780.000	-74.392	-74.392	0	CHAR
1.00000	0.10000	0.20001	1166.66670.000	156.235	156.235	1	RX2390
1.00000	0.10000	0.10001	1083.33340.000	134.854	134.854	1	RX2390
1.00000	0.10000	0.00001	1055.55550.000	127.767	127.767	0	CHAR
1.00000	0.10000	0.00001	1000.00000.000	113.671	113.671	0	CHAR
1.00000	0.10000	0.00001	944.44450.000	99.683	99.683	0	CHAR
1.00000	0.10000	0.00001	888.88890.000	85.803	85.803	0	CHAR
1.00000	0.10000	0.00001	833.33340.000	70.892	70.892	0	CHAR
1.00000	0.10000	0.00001	777.77780.000	53.675	53.675	0	CHAR
1.00000	0.10000	0.00001	722.22220.000	35.215	35.215	0	CHAR
1.00000	0.10000	0.00001	666.66670.000	15.061	15.061	0	CHAR
1.00000	0.10000	0.00001	611.11110.000	-5.093	-5.093	0	CHAR

1.00000	0.10000	0.00001	555.55550.000	-24.721	-24.721	0	CHAR
1.00000	0.10000	0.00001	416.66670.000	-84.520	-84.520	0	CHAR
1.00000	0.10000	0.00001	297.77780.000	-142.020	-142.020	0	CHAR
1.00000	0.20000	0.20001	1166.66670.000	95.068	95.068	1	RX2390
1.00000	0.20000	0.10001	11083.33340.000	75.468	75.468	1	RX2390
1.00000	0.20000	0.00001	1055.55550.000	68.972	68.972	0	CHAR
1.00000	0.20000	0.00001	1000.00000.000	56.050	56.050	0	CHAR
1.00000	0.20000	0.00001	944.44450.000	43.228	43.228	0	CHAR
1.00000	0.20000	0.00001	888.88890.000	30.505	30.505	0	CHAR
1.00000	0.20000	0.00001	833.33340.000	15.780	15.780	0	CHAR
1.00000	0.20000	0.00001	777.77780.000	-3.296	-3.296	0	CHAR
1.00000	0.20000	0.00001	722.22220.000	-24.889	-24.889	0	CHAR
1.00000	0.20000	0.00001	666.66670.000	-49.748	-49.748	0	CHAR
1.00000	0.20000	0.00001	611.11110.000	-74.607	-74.607	0	CHAR
1.00000	0.20000	0.00001	555.55550.000	-98.983	-98.983	0	CHAR
1.00000	0.20000	0.00001	416.66670.000	-179.749	-179.749	0	CHAR
1.00000	0.20000	0.00001	297.77780.000	-260.370	-260.370	0	CHAR
1.00000	0.40000	0.20001	1166.66670.000	-1.053	-1.053	1	RX2390
1.00000	0.40000	0.10001	11083.33340.000	-17.853	-17.853	1	RX2390
1.00000	0.40000	0.00001	1055.55550.000	-23.421	-23.421	0	CHAR
1.00000	0.40000	0.00001	1000.00000.000	-34.496	-34.496	0	CHAR
1.00000	0.40000	0.00001	944.44450.000	-45.487	-45.487	0	CHAR
1.00000	0.40000	0.00001	888.88890.000	-56.393	-56.393	0	CHAR
1.00000	0.40000	0.00001	833.33340.000	-70.824	-70.824	0	CHAR
1.00000	0.40000	0.00001	777.77780.000	-92.823	-92.823	0	CHAR
1.00000	0.40000	0.00001	722.22220.000	-119.338	-119.338	0	CHAR
1.00000	0.40000	0.00001	666.66670.000	-151.590	-151.590	0	CHAR
1.00000	0.40000	0.00001	611.11110.000	-183.843	-183.843	0	CHAR
1.00000	0.40000	0.00001	555.55550.000	-215.682	-215.682	0	CHAR
1.00000	0.40000	0.00001	416.66670.000	-329.395	-329.395	0	CHAR
1.00000	0.40000	0.00001	297.77780.000	-446.349	-446.349	0	CHAR
1.00000	0.60000	0.20001	1166.66670.000	-73.144	-73.144	1	RX2390
1.00000	0.60000	0.10001	11083.33340.000	-87.844	-87.844	1	RX2390
1.00000	0.60000	0.00001	1055.55550.000	-92.716	-92.716	0	CHAR
1.00000	0.60000	0.00001	1000.00000.000	-102.407	-102.407	0	CHAR
1.00000	0.60000	0.00001	944.44450.000	-112.024	-112.024	0	CHAR
1.00000	0.60000	0.00001	888.88890.000	-121.566	-121.566	0	CHAR
1.00000	0.60000	0.00001	833.33340.000	-135.778	-135.778	0	CHAR
1.00000	0.60000	0.00001	777.77780.000	-159.968	-159.968	0	CHAR
1.00000	0.60000	0.00001	722.22220.000	-190.174	-190.174	0	CHAR
1.00000	0.60000	0.00001	666.66670.000	-227.972	-227.972	0	CHAR
1.00000	0.60000	0.00001	611.11110.000	-265.770	-265.770	0	CHAR
1.00000	0.60000	0.00001	555.55550.000	-303.206	-303.206	0	CHAR
1.00000	0.60000	0.00001	416.66670.000	-441.629	-441.629	0	CHAR
1.00000	0.60000	0.00001	297.77780.000	-585.833	-585.833	0	CHAR
1.00000	1.00000	0.20001	1166.66670.000	-174.071	-174.071	1	RX2390
1.00000	1.00000	0.10001	11083.33340.000	-185.830	-185.830	1	RX2390
1.00000	1.00000	0.00001	1055.55550.000	-189.728	-189.728	0	CHAR
1.00000	1.00000	0.00001	1000.00000.000	-197.481	-197.481	0	CHAR
1.00000	1.00000	0.00001	944.44450.000	-205.175	-205.175	0	CHAR
1.00000	1.00000	0.00001	888.88890.000	-212.808	-212.808	0	CHAR
1.00000	1.00000	0.00001	833.33340.000	-226.712	-226.712	0	CHAR
1.00000	1.00000	0.00001	777.77780.000	-253.972	-253.972	0	CHAR
1.00000	1.00000	0.00001	722.22220.000	-289.345	-289.345	0	CHAR
1.00000	1.00000	0.00001	666.66670.000	-334.907	-334.907	0	CHAR
1.00000	1.00000	0.00001	611.11110.000	-380.468	-380.468	0	CHAR
1.00000	1.00000	0.00001	555.55550.000	-425.740	-425.740	0	CHAR
1.00000	1.00000	0.00001	416.66670.000	-598.757	-598.757	0	CHAR
1.00000	1.00000	0.00001	297.77780.000	-781.111	-781.111	0	CHAR
1.00000	1.50000	0.20001	1166.66670.000	-254.812	-254.812	1	RX2390

1.00000	1.50000	0.100011083.33340.000	-264.220	-264.220	1	RX2390
1.00000	1.50000	0.000011055.55550.000	-267.338	-267.338	0	CHAR
1.00000	1.50000	0.000011000.00000.000	-273.540	-273.540	0	CHAR
1.00000	1.50000	0.00001 944.44450.000	-279.695	-279.695	0	CHAR
1.00000	1.50000	0.00001 888.88890.000	-285.802	-285.802	0	CHAR
1.00000	1.50000	0.00001 833.33340.000	-299.460	-299.460	0	CHAR
1.00000	1.50000	0.00001 777.77780.000	-329.174	-329.174	0	CHAR
1.00000	1.50000	0.00001 722.22220.000	-368.682	-368.682	0	CHAR
1.00000	1.50000	0.00001 666.66670.000	-420.454	-420.454	0	CHAR
1.00000	1.50000	0.00001 611.11110.000	-472.227	-472.227	0	CHAR
1.00000	1.50000	0.00001 555.55550.000	-523.767	-523.767	0	CHAR
1.00000	1.50000	0.00001 416.66670.000	-724.460	-724.460	0	CHAR
1.00000	1.50000	0.00001 297.77780.000	-937.333	-937.333	0	CHAR

**APPENDIX C**  
**EXAMPLE CMA OUTPUT DECK**

AEROTHERM CHARRING MATERIAL THERMAL RESPONSE AND' ABLATION PROGRAM \*\* CMA92FLO 1.0  
 Check case for expansion model to compare in depth conduction PG. 1  
 using semi-infinite insulator conductor 0.4" thickness  
 using properties derived from shear and phase 1 tests  
 BCs and low conductivity metal 75 w/cm2

---REACTION KINETIC EQUATION---

$$DW/Dt = (-B(1)*EXP(-E(1)/T)W_o(1)((W(1)-W_c(1))/W_o(1))^{**PSI(1)}) \\
 + (-B(2)*EXP(-E(2)/T)W_o(2)((W(2)-W_c(2))/W_o(2))^{**PSI(2)}) \\
 + (-B(3)*EXP(-E(3)/T)W_o(3)((W(3)-W_c(3))/W_o(3))^{**PSI(3)}) \\
 + (-B(4)*EXP(-E(4)/T)W_o(4)((W(4)-W_c(4))/W_o(4))^{**PSI(4)})$$

---REACTION KINETIC CONSTANTS---

REACTION	W <sub>o</sub> (1/SEC)	W <sub>c</sub>	B (DEG R)	PSI (DEG R)	E (DEG R)	T REAC
1	0.20	0.00	0.4617D+02	2.40	0.7105D+04	530. RX 1
2	0.13	0.00	0.2680D+05	4.50	0.9059D+04	530. RX 2
3	0.16	0.00	0.6980D+13	4.30	0.4077D+05	530. RX 3
4	0.52	0.29	0.3748D+11	3.00	0.2854D+05	530. RX 4

RESIN VOLUME FRACTION, GAMMA = 0.900(MASS FRACTION = 0.006)

---TIME INCREMENT INFORMATION---

INITIAL TIME (SEC) 0.0000 FINAL TIME (SEC) 45.0000

OUTPUT INTERVAL = 0.5000 SEC FROM INITIAL TIME UNTIL 10.0000 SEC  
 OUTPUT INTERVAL = 5.0000 SEC FROM 10.0000 SEC UNTIL FINAL TIME

MAXIMUM TIME STEP = 1.0000 SECONDS

AEROTHERM CHARRING MATERIAL THERMAL RESPONSE AND' ABLATION PROGRAM \*\* CMA92FLO 1.0  
 Check case for expansion model to compare in depth conduction PG. 2

---NODAL DATA---

NODE NO.	MATL NO.	TEMPERATURE (DEG.RANKINE)	RELATIVE THICKNESS AREA (INCHES)	NODALDEPTH (INCHES)	CONT.RESISTANCE (SQFT-S-DEG/BTU)
1	1	538.30	0.1000D+01	0.00100	0.000000*
2	1	538.30	0.1000D+01	0.00100	0.001500
3	1	538.30	0.1000D+01	0.00100	0.002500
4	1	538.30	0.1000D+01	0.00100	0.003500
5	1	538.30	0.1000D+01	0.00100	0.004500
6	1	538.30	0.1000D+01	0.00100	0.005500
7	1	538.30	0.1000D+01	0.00100	0.006500
8	1	538.30	0.1000D+01	0.00100	0.007500
9	1	538.30	0.1000D+01	0.00100	0.008500
10	1	538.30	0.1000D+01	0.00100	0.009500
11	1	538.30	0.1000D+01	0.00200	0.011000
12	1	538.30	0.1000D+01	0.00200	0.013000
13	1	538.30	0.1000D+01	0.00200	0.015000
14	1	538.30	0.1000D+01	0.00200	0.017000
15	1	538.30	0.1000D+01	0.00200	0.019000
16	1	538.30	0.1000D+01	0.00200	0.021000
17	1	538.30	0.1000D+01	0.00200	0.023000
18	1	538.30	0.1000D+01	0.00200	0.025000
19	1	538.30	0.1000D+01	0.00200	0.027000
20	1	538.30	0.1000D+01	0.00200	0.029000
21	1	538.30	0.1000D+01	0.00200	0.031000
22	1	538.30	0.1000D+01	0.00200	0.033000
23	1	538.30	0.1000D+01	0.00200	0.035000
24	1	538.30	0.1000D+01	0.00200	0.037000
25	1	538.30	0.1000D+01	0.00200	0.039000
26	1	538.30	0.1000D+01	0.00200	0.041000
27	1	538.30	0.1000D+01	0.00200	0.043000
28	1	538.30	0.1000D+01	0.00200	0.045000

29	1	538.30	0.1000D+01	0.00200	0.047000	0.0000D+00
30	1	538.30	0.1000D+01	0.00200	0.049000	0.0000D+00
31	1	538.30	0.1000D+01	0.00200	0.051000	0.0000D+00
32	1	538.30	0.1000D+01	0.00200	0.053000	0.0000D+00
33	1	538.30	0.1000D+01	0.00200	0.055000	0.0000D+00
34	1	538.30	0.1000D+01	0.00200	0.057000	0.0000D+00
35	1	538.30	0.1000D+01	0.00200	0.059000	0.0000D+00
36	1	538.30	0.1000D+01	0.00500	0.062500	0.0000D+00
37	1	538.30	0.1000D+01	0.00500	0.067500	0.0000D+00
38	1	538.30	0.1000D+01	0.00500	0.072500	0.0000D+00
39	1	538.30	0.1000D+01	0.00500	0.077500	0.0000D+00
40	1	538.30	0.1000D+01	0.00500	0.082500	0.0000D+00
41	1	538.30	0.1000D+01	0.00500	0.087500	0.0000D+00
42	1	538.30	0.1000D+01	0.00500	0.092500	0.0000D+00
43	1	538.30	0.1000D+01	0.00500	0.097500	0.0000D+00
44	1	538.30	0.1000D+01	0.00500	0.102500	0.0000D+00
45	1	538.30	0.1000D+01	0.00500	0.107500	0.0000D+00
46	1	538.30	0.1000D+01	0.00500	0.112500	0.0000D+00
47	1	538.30	0.1000D+01	0.00500	0.117500	0.0000D+00
48	1	538.30	0.1000D+01	0.00500	0.122500	0.0000D+00
49	1	538.30	0.1000D+01	0.00500	0.127500	0.0000D+00
50	1	538.30	0.1000D+01	0.00500	0.132500	0.0000D+00
51	1	538.30	0.1000D+01	0.00500	0.137500	0.0000D+00
52	1	538.30	0.1000D+01	0.00500	0.142500	0.0000D+00
53	1	538.30	0.1000D+01	0.00500	0.147500	0.0000D+00
54	1	538.30	0.1000D+01	0.00500	0.152500	0.0000D+00
55	1	538.30	0.1000D+01	0.00500	0.157500	0.0000D+00
56	1	538.30	0.1000D+01	0.00500	0.162500	0.0000D+00
57	1	538.30	0.1000D+01	0.00500	0.167500	0.0000D+00
58	1	538.30	0.1000D+01	0.00500	0.172500	0.0000D+00
59	1	538.30	0.1000D+01	0.00500	0.177500	0.0000D+00
60	1	538.30	0.1000D+01	0.00500	0.182500	0.0000D+00
61	1	538.30	0.1000D+01	0.00500	0.187500	0.0000D+00
62	1	538.30	0.1000D+01	0.00500	0.192500	0.0000D+00
63	1	538.30	0.1000D+01	0.00500	0.197500	0.0000D+00
64	1	538.30	0.1000D+01	0.00500	0.202500	0.0000D+00
65	1	538.30	0.1000D+01	0.00500	0.207500	0.0000D+00
66	1	538.30	0.1000D+01	0.00500	0.212500	0.0000D+00
67	1	538.30	0.1000D+01	0.00500	0.217500	0.0000D+00
68	1	538.30	0.1000D+01	0.00500	0.222500	0.0000D+00
69	1	538.30	0.1000D+01	0.00500	0.227500	0.0000D+00
70	1	538.30	0.1000D+01	0.00500	0.232500	0.0000D+00
71	1	538.30	0.1000D+01	0.00500	0.237500	0.0000D+00
72	1	538.30	0.1000D+01	0.00500	0.242500	0.0000D+00
73	1	538.30	0.1000D+01	0.00500	0.247500	0.0000D+00
74	1	538.30	0.1000D+01	0.01000	0.255000	0.0000D+00
75	1	538.30	0.1000D+01	0.01000	0.265000	0.0000D+00
76	1	538.30	0.1000D+01	0.01000	0.275000	0.0000D+00
77	1	538.30	0.1000D+01	0.01000	0.285000	0.0000D+00
78	1	538.30	0.1000D+01	0.01000	0.295000	0.0000D+00
79	1	538.30	0.1000D+01	0.01000	0.305000	0.0000D+00
80	1	538.30	0.1000D+01	0.01000	0.315000	0.0000D+00
81	1	538.30	0.1000D+01	0.01000	0.325000	0.0000D+00
82	1	538.30	0.1000D+01	0.01000	0.335000	0.0000D+00
83	1	538.30	0.1000D+01	0.01000	0.345000	0.0000D+00
84	1	538.30	0.1000D+01	0.01000	0.355000	0.0000D+00
85	1	538.30	0.1000D+01	0.01000	0.365000	0.0000D+00
86	1	538.30	0.1000D+01	0.01000	0.375000	0.0000D+00
87	1	538.30	0.1000D+01	0.01000	0.385000	0.0000D+00
88	1	538.30	0.1000D+01	0.01000	0.395000	0.0000D+00

\*PLANAR SURFACE

MINIMUM THICKNESS OF LAST ABLATOR NODE 0.02 (% OF NODELET THICKNESS)

THERE ARE 10 NODELETS ASSIGNED TO EACH ABLATING NODE

AEROTHERM CHARRING MATERIAL THERMAL RESPONSE AND' ABLATION PROGRAM \*\* CMA92FLO 1.0

Check case for expansion model to compare in depth conduction PG. 3

BACK WALL CONVECTION BACK WALL RESERVOIR

COEF BTU/FTSQ-SEC-DEG R	EMISSIVITY	TEMPERATURE
0.0000	0.000	536.00

---HEAT OF FORMATION OF MATERIAL CONSTITUENTS---  
(BTU/LB)

PLASTIC	CHAR	GAS
-2451.00	-1781.00	0.00

ENTHALPY DATUM TEMPERATURE = 536.400 DEG RANKINE

---MATERIAL THERMAL PROPERTY DATA---

MATERIAL NO. 1	MATERIAL NO. 2	MATERIAL NOS. 3 THROUGH 10
VIRGIN PLASTIC	CHAR	BACK-UP

DECOMPOSING BACK-UP VIRGIN MATERIALS 22,24,26,28,30  
CHAR MATERIALS 23,25,27,29,31

MATERIAL NO. 1	DENSITY = 78.000 LB/CU FT				
TEMPERATURE	SPECIFIC HEAT	CONDUCTIVITY	SENSIBLE	TOTAL	SPECT
	ENTHALPY	EMISS	ABSORP		
(DEG R)	(BTU/LB-DEG)	(BTU/FT-SEC-DEG)	(BTU/LB)		
530.00	0.3600	0.0000528	-2.30	0.9000	0.9000
546.00	0.3600	0.0000528	3.46	0.9000	0.9000
555.00	0.3600	0.0000528	6.70	0.9000	0.9000
564.00	0.3600	0.0000528	9.94	0.9000	0.9000
573.00	0.3600	0.0000528	13.18	0.9000	0.9000
580.00	0.3600	0.0000528	15.70	0.9000	0.9000
591.00	0.3600	0.0000528	19.66	0.9000	0.9000
600.00	0.3600	0.0000528	22.90	0.9000	0.9000
610.00	0.3600	0.0000500	26.50	0.9000	0.9000
620.00	0.3600	0.0000472	30.10	0.9000	0.9000
635.00	0.3600	0.0000417	35.50	0.9000	0.9000
672.00	0.3700	0.0000389	49.00	0.9000	0.9000
760.00	0.3800	0.0000389	82.00	0.9000	0.9000
1060.00	0.3800	0.0000278	196.00	0.9000	0.9000
1360.00	0.3900	0.0000222	311.50	0.9000	0.9000
1460.00	0.3900	0.0000167	350.50	0.9000	0.9000
1960.00	0.4100	0.0000111	550.50	0.9000	0.9000
2460.00	0.4200	0.0000111	758.00	0.9000	0.9000
2960.00	0.4400	0.0000111	973.00	0.9000	0.9000
3460.00	0.4800	0.0000056	1203.00	0.9000	0.9000

AEROTHERM CHARRING MATERIAL THERMAL RESPONSE AND' ABLATION PROGRAM \*\* CMA92FLO 1.0  
Check case for expansion model to compare in depth conduction PG. 4

MATERIAL NO. 2	DENSITY = 29.250 LB/CU FT				
TEMPERATURE	SPECIFIC HEAT	CONDUCTIVITY	SENSIBLE	TOTAL	SPECT
	ENTHALPY	EMISS	ABSORP		
(DEG R)	(BTU/LB-DEG)	(BTU/FT-SEC-DEG)	(BTU/LB)		
512.00	0.3179	0.0000278	-7.09	0.9000	0.9000
592.00	0.2629	0.0000278	16.15	0.9000	0.9000
672.00	0.2870	0.0000278	38.14	0.9000	0.9000
762.00	0.2950	0.0000278	64.33	0.9000	0.9000
852.00	0.3100	0.0000264	91.56	0.9000	0.9000
1032.00	0.3107	0.0000250	147.42	0.9000	0.9000
1122.00	0.3179	0.0000236	175.71	0.9000	0.9000
1212.00	0.3262	0.0000222	204.69	0.9000	0.9000
1302.00	0.3346	0.0000208	234.43	0.9000	0.9000
1392.00	0.4000	0.0000194	267.48	0.9000	0.9000
1572.00	0.4400	0.0000181	343.08	0.9000	0.9000
1752.00	0.4500	0.0000167	423.18	0.9000	0.9000
1932.00	0.4600	0.0000153	505.08	0.9000	0.9000
2292.00	0.4700	0.0000139	672.48	0.9000	0.9000
3460.00	0.4800	0.0000125	1227.28	0.9000	0.9000

# RESIN PYROLYSIS GAS SENSIBLE ENTHALPY (BTU/LBM)

TEMPERATURE(R)	PRESSURE(ATM)		
	P= 0.03	P= 1.00	P= 0.00
460.00	-2850.00	-2850.00	
560.00	-2800.00	-2800.00	
743.00	-2003.00	-2003.00	
1355.00	-1159.00	-1159.00	
1555.00	-1040.00	-1040.00	
2000.00	-1040.00	-1040.00	

---TIME DEPENDENT BOUNDARY CONDITIONS---

## OPTION 3

TIME (SEC)	VIEW FACTOR	RADIATION HEAT RATE (BTU/SQ FT- SECOND)	PRESSURE (ATM)
0.00	1.000	66.000	1.0000
45.00	1.000	66.000	1.0000
46.00	1.000	0.000	1.0000
100.00	1.000	0.000	1.0000

CH/CHO = (LN(1.+PHI)) / PHI WHERE PHI = 2.\*BRP\*MDOT/CH. BRP IN TABLE

AEROTHERM CHARRING MATERIAL THERMAL RESPONSE AND' ABLATION PROGRAM \*\* CMA92FLO 1.0  
Check case for expansion model to compare in depth conduction PG. 5

---SURFACE EQUILIBRIUM DATA---

EQUAL MASS AND HEAT TRANSFER COEFFICIENTS AND EQUAL DIFFUSION COEFFICIENTS  
NOMINAL SURFACE VIEW FACTOR = 1.000  
FISSURE MODEL NOT USED FOR GAS TERMS  
NO RADIUS CORRECTION ON CH  
NO CHAR SWELL CORRECTION ON SURFACE RECESSION

M-DOT-GAS/CM = 0.1000E-03 PRESSURE = 1.0000 ATM

TEMP (DEG R)	M-DOT- CHAR/CM	ENTH1 (BTU/LB)	ENTH2 (BTU/LB)	TCHEM (BTU/LB)	M-DOT- FAIL/CM	SURFACE SPECIES
536.00	0.1000E-04	-0.28	-0.28	-0.02	0.0000E+00	
750.00	0.1000E-04	53.33	53.33	-53.55	0.0000E+00	
1000.00	0.1000E-04	115.73	115.73	-115.93	0.0000E+00	
1100.00	0.1000E-04	140.82	140.82	-141.00	0.0000E+00	
1200.00	0.1000E-04	166.94	166.94	-167.11	0.0000E+00	
1300.00	0.1000E-04	193.07	193.07	-193.23	0.0000E+00	
1400.00	0.1000E-04	219.54	219.54	-219.69	0.0000E+00	
1500.00	0.1000E-04	246.52	246.52	-246.66	0.0000E+00	
1600.00	0.1000E-04	273.76	273.76	-273.91	0.0000E+00	
1700.00	0.1000E-04	301.24	301.24	-301.39	0.0000E+00	
1800.00	0.1000E-04	328.93	328.93	-329.09	0.0000E+00	
1900.00	0.1000E-04	356.84	356.84	-357.00	0.0000E+00	
1950.00	0.1000E+00	370.87	370.87	-534.87	0.0000E+00	RX23
2100.00	0.2000E+00	413.20	413.20	-735.56	0.0000E+00	RX23

M-DOT-GAS/CM = 0.4000E-03 PRESSURE = 1.0000 ATM

TEMP (DEG R)	M-DOT- CHAR/CM	ENTH1 (BTU/LB)	ENTH2 (BTU/LB)	TCHEM (BTU/LB)	M-DOT- FAIL/CM	SURFACE SPECIES
-----------------	-------------------	-------------------	-------------------	-------------------	-------------------	--------------------



536.00	0.1000E-04	-1.12	-1.12	-0.02	0.0000E+00	
750.00	0.1000E-04	52.65	52.65	-53.49	0.0000E+00	
1000.00	0.1000E-04	115.21	115.21	-115.93	0.0000E+00	
1100.00	0.1000E-04	140.32	140.32	-141.00	0.0000E+00	
1200.00	0.1000E-04	166.48	166.48	-167.11	0.0000E+00	
1300.00	0.1000E-04	192.64	192.64	-193.23	0.0000E+00	
1400.00	0.1000E-04	219.13	219.13	-219.69	0.0000E+00	
1500.00	0.1000E-04	246.12	246.12	-246.67	0.0000E+00	
1600.00	0.1000E-04	273.36	273.36	-273.91	0.0000E+00	
1700.00	0.1000E-04	300.84	300.84	-301.39	0.0000E+00	
1800.00	0.1000E-04	328.52	328.52	-329.09	0.0000E+00	
1900.00	0.1000E-04	356.42	356.42	-356.99	0.0000E+00	
1950.00	0.1000E+00	370.45	370.45	-534.83	0.0000E+00	RX23
2100.00	0.2000E+00	412.77	412.77	-735.47	0.0000E+00	RX23

AEROTHERM CHARRING MATERIAL THERMAL RESPONSE AND' ABLATION PROGRAM \*\* CMA92FLO 1.0  
Check case for expansion model to compare in depth conduction PG. 6

M-DOT-GAS/CM = 0.1000E-02 PRESSURE = 1.0000 ATM

TEMP (DEG R)	M-DOT- CHAR/CM	ENTH1 (BTU/LB)	ENTH2 (BTU/LB)	TCHEM (BTU/LB)	M-DOT- FAIL/CM	SURFACE SPECIES
536.00	0.1000E-04	-2.81	-2.81	-0.02	0.0000E+00	
750.00	0.1000E-04	51.30	51.30	-53.36	0.0000E+00	
1000.00	0.1000E-04	114.15	114.15	-115.93	0.0000E+00	
1100.00	0.1000E-04	139.33	139.33	-141.00	0.0000E+00	
1200.00	0.1000E-04	165.56	165.56	-167.11	0.0000E+00	
1300.00	0.1000E-04	191.78	191.78	-193.23	0.0000E+00	
1400.00	0.1000E-04	218.32	218.32	-219.69	0.0000E+00	
1500.00	0.1000E-04	245.34	245.34	-246.67	0.0000E+00	
1600.00	0.1000E-04	272.58	272.58	-273.91	0.0000E+00	
1700.00	0.1000E-04	300.03	300.03	-301.39	0.0000E+00	
1800.00	0.1000E-04	327.70	327.70	-329.09	0.0000E+00	
1900.00	0.1000E-04	355.58	355.58	-356.99	0.0000E+00	
1950.00	0.1000E+00	369.60	369.60	-534.74	0.0000E+00	RX23
2100.00	0.2000E+00	411.89	411.89	-735.30	0.0000E+00	RX23

M-DOT-GAS/CM = 0.4000E-02 PRESSURE = 1.0000 ATM

TEMP (DEG R)	M-DOT- CHAR/CM	ENTH1 (BTU/LB)	ENTH2 (BTU/LB)	TCHEM (BTU/LB)	M-DOT- FAIL/CM	SURFACE SPECIES
536.00	0.1000E-04	-11.20	-11.20	-0.02	0.0000E+00	
750.00	0.1000E-04	44.54	44.54	-52.71	0.0000E+00	
1000.00	0.1000E-04	108.88	108.88	-115.93	0.0000E+00	
1100.00	0.1000E-04	134.40	134.40	-141.00	0.0000E+00	
1200.00	0.1000E-04	160.96	160.96	-167.11	0.0000E+00	
1300.00	0.1000E-04	187.52	187.52	-193.23	0.0000E+00	
1400.00	0.1000E-04	214.28	214.28	-219.68	0.0000E+00	
1500.00	0.1000E-04	241.43	241.43	-246.70	0.0000E+00	
1600.00	0.1000E-04	268.66	268.66	-273.91	0.0000E+00	
1700.00	0.1000E-04	296.03	296.03	-301.39	0.0000E+00	
1800.00	0.1000E-04	323.61	323.61	-329.09	0.0000E+00	
1900.00	0.1000E-04	351.41	351.41	-357.00	0.0000E+00	
1950.00	0.1000E+00	365.39	365.39	-534.32	0.0000E+00	RX23
2100.00	0.2000E+00	407.56	407.56	-734.43	0.0000E+00	RX23

AEROTHERM CHARRING MATERIAL THERMAL RESPONSE AND' ABLATION PROGRAM \*\* CMA92FLO 1.0  
Check case for expansion model to compare in depth conduction PG. 7

M-DOT-GAS/CM = 0.6000E-02 PRESSURE = 1.0000 ATM

TEMP (DEG R)	M-DOT- CHAR/CM	ENTH1 (BTU/LB)	ENTH2 (BTU/LB)	TCHEM (BTU/LB)	M-DOT- FAIL/CM	SURFACE SPECIES
536.00	0.1000E-04	-16.77	-16.77	-0.02	0.0000E+00	
750.00	0.1000E-04	40.06	40.06	-52.28	0.0000E+00	
1000.00	0.1000E-04	105.39	105.39	-115.93	0.0000E+00	

1100.00	0.1000E-04	131.13	131.13	-141.00	0.0000E+00	
1200.00	0.1000E-04	157.91	157.91	-167.11	0.0000E+00	
1300.00	0.1000E-04	184.69	184.69	-193.23	0.0000E+00	
1400.00	0.1000E-04	211.60	211.60	-219.68	0.0000E+00	
1500.00	0.1000E-04	238.84	238.84	-246.72	0.0000E+00	
1600.00	0.1000E-04	266.05	266.05	-273.91	0.0000E+00	
1700.00	0.1000E-04	293.37	293.37	-301.39	0.0000E+00	
1800.00	0.1000E-04	320.90	320.90	-329.09	0.0000E+00	
1900.00	0.1000E-04	348.65	348.65	-357.00	0.0000E+00	
1950.00	0.1000E+00	362.60	362.60	-534.04	0.0000E+00	RX23
2100.00	0.2000E+00	404.68	404.68	-733.86	0.0000E+00	RX23

M-DOT-GAS/CM = 0.8000E-02                      PRESSURE = 1.0000 ATM

TEMP (DEG R)	M-DOT- CHAR/CM	ENTH1 (BTU/LB)	ENTH2 (BTU/LB)	TCHEM (BTU/LB)	M-DOT- FAIL/CM	SURFACE SPECIES
536.00	0.1000E-04	-22.32	-22.32	-0.02	0.0000E+00	
750.00	0.1000E-04	35.60	35.60	-51.85	0.0000E+00	
1000.00	0.1000E-04	101.91	101.91	-115.93	0.0000E+00	
1100.00	0.1000E-04	127.87	127.87	-141.00	0.0000E+00	
1200.00	0.1000E-04	154.88	154.88	-167.11	0.0000E+00	
1300.00	0.1000E-04	181.88	181.88	-193.23	0.0000E+00	
1400.00	0.1000E-04	208.93	208.93	-219.68	0.0000E+00	
1500.00	0.1000E-04	236.25	236.25	-246.74	0.0000E+00	
1600.00	0.1000E-04	263.46	263.46	-273.91	0.0000E+00	
1700.00	0.1000E-04	290.73	290.73	-301.39	0.0000E+00	
1800.00	0.1000E-04	318.20	318.20	-329.09	0.0000E+00	
1900.00	0.1000E-04	345.89	345.89	-357.00	0.0000E+00	
1950.00	0.1000E+00	359.81	359.81	-533.76	0.0000E+00	RX23
2100.00	0.2000E+00	401.81	401.81	-733.28	0.0000E+00	RX23

AEROTHERM CHARRING MATERIAL THERMAL RESPONSE AND' ABLATION PROGRAM \*\* CMA92FLO 1.0  
Check case for expansion model to compare in depth conduction                      PG. 8

M-DOT-GAS/CM = 0.2000E-01                      PRESSURE = 1.0000 ATM

TEMP (DEG R)	M-DOT- CHAR/CM	ENTH1 (BTU/LB)	ENTH2 (BTU/LB)	TCHEM (BTU/LB)	M-DOT- FAIL/CM	SURFACE SPECIES
536.00	0.1000E-04	-55.14	-55.14	-0.02	0.0000E+00	
750.00	0.1000E-04	9.19	9.19	-49.26	0.0000E+00	
1000.00	0.1000E-04	81.31	81.31	-115.93	0.0000E+00	
1100.00	0.1000E-04	108.60	108.60	-141.00	0.0000E+00	
1200.00	0.1000E-04	136.90	136.90	-167.11	0.0000E+00	
1300.00	0.1000E-04	165.21	165.21	-193.23	0.0000E+00	
1400.00	0.1000E-04	193.13	193.13	-219.66	0.0000E+00	
1500.00	0.1000E-04	220.97	220.97	-246.86	0.0000E+00	
1600.00	0.1000E-04	248.13	248.13	-273.91	0.0000E+00	
1700.00	0.1000E-04	275.07	275.07	-301.39	0.0000E+00	
1800.00	0.1000E-04	302.23	302.23	-329.09	0.0000E+00	
1900.00	0.1000E-04	329.59	329.59	-357.00	0.0000E+00	
1950.00	0.1000E+00	343.34	343.34	-532.11	0.0000E+00	RX23
2100.00	0.2000E+00	384.85	384.85	-729.89	0.0000E+00	RX23

M-DOT-GAS/CM = 0.4000E-01                      PRESSURE = 1.0000 ATM

TEMP (DEG R)	M-DOT- CHAR/CM	ENTH1 (BTU/LB)	ENTH2 (BTU/LB)	TCHEM (BTU/LB)	M-DOT- FAIL/CM	SURFACE SPECIES
536.00	0.1000E-04	-108.15	-108.15	-0.02	0.0000E+00	
750.00	0.1000E-04	-33.47	-33.47	-44.94	0.0000E+00	
1000.00	0.1000E-04	48.05	48.05	-115.93	0.0000E+00	
1100.00	0.1000E-04	77.46	77.46	-141.00	0.0000E+00	
1200.00	0.1000E-04	107.87	107.87	-167.11	0.0000E+00	
1300.00	0.1000E-04	138.28	138.28	-193.23	0.0000E+00	
1400.00	0.1000E-04	167.61	167.61	-219.62	0.0000E+00	
1500.00	0.1000E-04	196.28	196.28	-247.06	0.0000E+00	
1600.00	0.1000E-04	223.36	223.36	-273.91	0.0000E+00	
1700.00	0.1000E-04	249.78	249.78	-301.39	0.0000E+00	
1800.00	0.1000E-04	276.41	276.41	-329.09	0.0000E+00	

1900.00	0.1000E-04	303.25	303.25	-357.00	0.0000E+00	
1950.00	0.1000E+00	316.74	316.74	-529.45	0.0000E+00	RX23
2100.00	0.2000E+00	357.45	357.45	-724.41	0.0000E+00	RX23

AEROTHERM CHARRING MATERIAL THERMAL RESPONSE AND' ABLATION PROGRAM \*\* CMA92FLO 1.0  
Check case for expansion model to compare in depth conduction PG. 9

M-DOT-GAS/CM = 0.5000E-01 PRESSURE = 1.0000 ATM

TEMP (DEG R)	M-DOT- CHAR/CM	ENTH1 (BTU/LB)	ENTH2 (BTU/LB)	TCHEM (BTU/LB)	M-DOT- FAIL/CM	SURFACE SPECIES
536.00	0.1000E-04	-133.91	-133.91	-0.02	0.0000E+00	
750.00	0.1000E-04	-54.19	-54.19	-42.79	0.0000E+00	
1000.00	0.1000E-04	31.89	31.89	-115.93	0.0000E+00	
1100.00	0.1000E-04	62.33	62.33	-141.00	0.0000E+00	
1200.00	0.1000E-04	93.77	93.77	-167.11	0.0000E+00	
1300.00	0.1000E-04	125.21	125.21	-193.23	0.0000E+00	
1400.00	0.1000E-04	155.21	155.21	-219.60	0.0000E+00	
1500.00	0.1000E-04	184.29	184.29	-247.16	0.0000E+00	
1600.00	0.1000E-04	211.32	211.32	-273.91	0.0000E+00	
1700.00	0.1000E-04	237.50	237.50	-301.39	0.0000E+00	
1800.00	0.1000E-04	263.87	263.87	-329.08	0.0000E+00	
1900.00	0.1000E-04	290.46	290.46	-357.00	0.0000E+00	
1950.00	0.1000E+00	303.82	303.82	-528.16	0.0000E+00	RX23
2100.00	0.2000E+00	344.14	344.14	-721.75	0.0000E+00	RX23

M-DOT-GAS/CM = 0.1000E+00 PRESSURE = 1.0000 ATM

TEMP (DEG R)	M-DOT- CHAR/CM	ENTH1 (BTU/LB)	ENTH2 (BTU/LB)	TCHEM (BTU/LB)	M-DOT- FAIL/CM	SURFACE SPECIES
536.00	0.1000E-04	-255.64	-255.64	-0.02	0.0000E+00	
750.00	0.1000E-04	-152.14	-152.14	-32.00	0.0000E+00	
1000.00	0.1000E-04	-44.50	-44.50	-115.93	0.0000E+00	
1100.00	0.1000E-04	-9.17	-9.17	-141.00	0.0000E+00	
1200.00	0.1000E-04	27.11	27.11	-167.11	0.0000E+00	
1300.00	0.1000E-04	63.39	63.39	-193.23	0.0000E+00	
1400.00	0.1000E-04	96.61	96.61	-219.52	0.0000E+00	
1500.00	0.1000E-04	127.61	127.61	-247.65	0.0000E+00	
1600.00	0.1000E-04	154.45	154.45	-273.91	0.0000E+00	
1700.00	0.1000E-04	179.43	179.43	-301.39	0.0000E+00	
1800.00	0.1000E-04	204.61	204.61	-329.08	0.0000E+00	
1900.00	0.1000E-04	229.98	229.98	-356.99	0.0000E+00	
1950.00	0.1000E+00	242.74	242.74	-522.05	0.0000E+00	RX23
2100.00	0.2000E+00	281.22	281.22	-709.16	0.0000E+00	RX23

AEROTHERM CHARRING MATERIAL THERMAL RESPONSE AND' ABLATION PROGRAM \*\* CMA92FLO 1.0  
Check case for expansion model to compare in depth conduction PG. 10

M-DOT-GAS/CM = 0.2000E+00 PRESSURE = 1.0000 ATM

TEMP (DEG R)	M-DOT- CHAR/CM	ENTH1 (BTU/LB)	ENTH2 (BTU/LB)	TCHEM (BTU/LB)	M-DOT- FAIL/CM	SURFACE SPECIES
536.00	0.1000E-04	-468.67	-468.67	-0.01	0.0000E+00	
750.00	0.1000E-04	-323.55	-323.55	-10.43	0.0000E+00	
1000.00	0.1000E-04	-178.17	-178.17	-115.93	0.0000E+00	
1100.00	0.1000E-04	-134.29	-134.29	-141.00	0.0000E+00	
1200.00	0.1000E-04	-89.55	-89.55	-167.11	0.0000E+00	
1300.00	0.1000E-04	-44.80	-44.80	-193.22	0.0000E+00	
1400.00	0.1000E-04	-5.93	-5.93	-219.34	0.0000E+00	
1500.00	0.1000E-04	28.40	28.40	-248.64	0.0000E+00	
1600.00	0.1000E-04	54.91	54.91	-273.91	0.0000E+00	
1700.00	0.1000E-04	77.81	77.81	-301.39	0.0000E+00	
1800.00	0.1000E-04	100.89	100.89	-329.08	0.0000E+00	
1900.00	0.1000E-04	124.15	124.15	-356.99	0.0000E+00	
1950.00	0.1000E+00	135.84	135.84	-511.36	0.0000E+00	RX23
2100.00	0.2000E+00	171.12	171.12	-687.14	0.0000E+00	RX23

M-DOT-GAS/CM = 0.4000E+00

PRESSURE = 1.0000 ATM

TEMP (DEG R)	M-DOT- CHAR/CM	ENTH1 (BTU/LB)	ENTH2 (BTU/LB)	TCHEM (BTU/LB)	M-DOT- FAIL/CM	SURFACE SPECIES
536.00	0.1000E-04	-803.43	-803.43	-0.01	0.0000E+00	
750.00	0.1000E-04	-592.91	-592.91	32.73	0.0000E+00	
1000.00	0.1000E-04	-388.23	-388.23	-115.92	0.0000E+00	
1100.00	0.1000E-04	-330.92	-330.92	-141.00	0.0000E+00	
1200.00	0.1000E-04	-272.86	-272.86	-167.11	0.0000E+00	
1300.00	0.1000E-04	-214.81	-214.81	-193.22	0.0000E+00	
1400.00	0.1000E-04	-167.08	-167.08	-218.99	0.0000E+00	
1500.00	0.1000E-04	-127.48	-127.48	-250.63	0.0000E+00	
1600.00	0.1000E-04	-101.51	-101.51	-273.90	0.0000E+00	
1700.00	0.1000E-04	-81.88	-81.88	-301.39	0.0000E+00	
1800.00	0.1000E-04	-62.09	-62.09	-329.08	0.0000E+00	
1900.00	0.1000E-04	-42.16	-42.16	-356.99	0.0000E+00	
1950.00	0.1000E+00	-32.14	-32.14	-494.56	0.0000E+00	RX23
2100.00	0.2000E+00	-1.90	-1.90	-652.54	0.0000E+00	RX23

AEROTHERM CHARRING MATERIAL THERMAL RESPONSE AND' ABLATION PROGRAM \*\* CMA92FLO 1.0

Check case for expansion model to compare in depth conduction PG. 11

M-DOT-GAS/CM = 0.6000E+00

PRESSURE = 1.0000 ATM

TEMP (DEG R)	M-DOT- CHAR/CM	ENTH1 (BTU/LB)	ENTH2 (BTU/LB)	TCHEM (BTU/LB)	M-DOT- FAIL/CM	SURFACE SPECIES
536.00	0.1000E-04	-1054.50	-1054.50	-0.01	0.0000E+00	
750.00	0.1000E-04	-794.93	-794.93	75.87	0.0000E+00	
1000.00	0.1000E-04	-545.77	-545.77	-115.92	0.0000E+00	
1100.00	0.1000E-04	-478.39	-478.39	-140.99	0.0000E+00	
1200.00	0.1000E-04	-410.35	-410.35	-167.11	0.0000E+00	
1300.00	0.1000E-04	-342.31	-342.31	-193.22	0.0000E+00	
1400.00	0.1000E-04	-287.94	-287.94	-218.64	0.0000E+00	
1500.00	0.1000E-04	-244.40	-244.40	-252.61	0.0000E+00	
1600.00	0.1000E-04	-218.82	-218.82	-273.90	0.0000E+00	
1700.00	0.1000E-04	-201.64	-201.64	-301.38	0.0000E+00	
1800.00	0.1000E-04	-184.33	-184.33	-329.08	0.0000E+00	
1900.00	0.1000E-04	-166.89	-166.89	-356.99	0.0000E+00	
1950.00	0.1000E+00	-158.12	-158.12	-481.96	0.0000E+00	RX23
2100.00	0.2000E+00	-131.66	-131.66	-626.58	0.0000E+00	RX23

M-DOT-GAS/CM = 0.1000E+01

PRESSURE = 1.0000 ATM

TEMP (DEG R)	M-DOT- CHAR/CM	ENTH1 (BTU/LB)	ENTH2 (BTU/LB)	TCHEM (BTU/LB)	M-DOT- FAIL/CM	SURFACE SPECIES
536.00	0.1000E-04	-1406.00	-1406.00	0.00	0.0000E+00	
750.00	0.1000E-04	-1077.76	-1077.76	162.17	0.0000E+00	
1000.00	0.1000E-04	-766.33	-766.33	-115.92	0.0000E+00	
1100.00	0.1000E-04	-684.84	-684.84	-140.99	0.0000E+00	
1200.00	0.1000E-04	-602.83	-602.83	-167.10	0.0000E+00	
1300.00	0.1000E-04	-520.82	-520.82	-193.22	0.0000E+00	
1400.00	0.1000E-04	-457.15	-457.15	-217.94	0.0000E+00	
1500.00	0.1000E-04	-408.08	-408.08	-256.57	0.0000E+00	
1600.00	0.1000E-04	-383.05	-383.05	-273.90	0.0000E+00	
1700.00	0.1000E-04	-369.31	-369.31	-301.38	0.0000E+00	
1800.00	0.1000E-04	-355.47	-355.47	-329.08	0.0000E+00	
1900.00	0.1000E-04	-341.51	-341.51	-356.99	0.0000E+00	
1950.00	0.1000E+00	-334.49	-334.49	-464.33	0.0000E+00	RX23
2100.00	0.2000E+00	-313.33	-313.33	-590.25	0.0000E+00	RX23

AEROTHERM CHARRING MATERIAL THERMAL RESPONSE AND' ABLATION PROGRAM \*\* CMA92FLO 1.0

Check case for expansion model to compare in depth conduction PG. 12

M-DOT-GAS/CM = 0.1500E+01

PRESSURE = 1.0000 ATM

TEMP (DEG R)	M-DOT- CHAR/CM	ENTH1 (BTU/LB)	ENTH2 (BTU/LB)	TCHEM (BTU/LB)	M-DOT- FAIL/CM	SURFACE SPECIES
-----------------	-------------------	-------------------	-------------------	-------------------	-------------------	--------------------

536.00	0.1000E-04	-1687.20	-1687.20	0.00	0.0000E+00	
750.00	0.1000E-04	-1304.03	-1304.03	270.05	0.0000E+00	
1000.00	0.1000E-04	-942.78	-942.78	-115.92	0.0000E+00	
1100.00	0.1000E-04	-850.01	-850.01	-140.99	0.0000E+00	
1200.00	0.1000E-04	-756.82	-756.82	-167.10	0.0000E+00	
1300.00	0.1000E-04	-663.63	-663.63	-193.21	0.0000E+00	
1400.00	0.1000E-04	-592.51	-592.51	-217.06	0.0000E+00	
1500.00	0.1000E-04	-539.03	-539.03	-261.53	0.0000E+00	
1600.00	0.1000E-04	-514.44	-514.44	-273.90	0.0000E+00	
1700.00	0.1000E-04	-503.45	-503.45	-301.38	0.0000E+00	
1800.00	0.1000E-04	-492.37	-492.37	-329.08	0.0000E+00	
1900.00	0.1000E-04	-481.21	-481.21	-356.99	0.0000E+00	
1950.00	0.1000E+00	-475.60	-475.60	-450.21	0.0000E+00	RX23
2100.00	0.2000E+00	-458.66	-458.66	-561.18	0.0000E+00	RX23

AEROTHERM CHARRING MATERIAL THERMAL RESPONSE AND' ABLATION PROGRAM \*\* CMA92FLO 1.0  
Check case for expansion model to compare in depth conduction PG. 13

----OUTPUT----

AEROTHERM CHARRING MATERIAL THERMAL RESPONSE AND' ABLATION PROGRAM \*\* CMA92FLO 1.0  
Check case for expansion model to compare in depth conduction PG. 14

----- 0.0000 SECONDS -----  
TIME SURF PROB SURFACE SURFACE H WALL H EDGE HEAT COEFF CH/CHO  
STEP ITER OPTN TEMP(R) RAD (IN) (BTU/LB) (BTU/LB) (LB/SQ FT-S)  
1 0 3 538.30 0.0000 0.00 0.00 0.00000 0.00000

---ABLATION RATES---  
B PRIME B PRIME G M DOT CHAR M DOT GAS M CHAR M GAS  
(LB/SQ FT-SEC) (LB/ORIG SQ FT)  
0.0000E+00 0.0000E+00 0.0000E+00 0.0000E+00 0.0000E+00 0.0000E+00

---RECESSIONS/RECESSION RATES---  
(IN) / (IN/SEC)  
SURFACE CHAR (0.15) PYROLYSIS (0.85)  
0.0000000/0.0000000 0.0000000/0.0000000 0.0000000/0.0000000

---SURFACE ENERGY FLUX TERMS---  
CURRENT RATES (BTU/SQ FT SURFACE-SEC)  
AND INTEGRATED VALUES (BTU/ORIG SQ FT)  
CONVECTED RADIATED RADIATED CHEMICAL CONDUCTION  
IN IN OUT GENERATION AWAY  
RATE 0.000E+00 0.000E+00 0.000E+00 0.000E+00 0.000E+00  
TOTAL 0.000E+00 0.000E+00 0.000E+00 0.000E+00 0.000E+00

---INTERIOR ENERGY TERMS---  
CURRENT RATES (BTU/SQ FT SURFACE-SEC)  
AND INTEGRATED VALUES (BTU/ORIG SQ FT)  
PYROL GAS DECOMP CONVECTION STORAGE LOSS AT  
PICK UP ABSORPTION WITH SOLIDS IN SOLID REAR FACE  
RATE 0.000E+00 0.000E+00 0.000E+00 0.000E+00 -0.230E-07  
TOTAL 0.000E+00 0.000E+00 0.000E+00 0.000E+00 -0.230E-09

NODE MAT		TEMP	DENSITY	ENTHALPY	NODE MAT		TEMP	DENSITY	ENTHALPY
		(DEG R)	(LB/CU FT)	(BTU/LB)			(DEG R)	(LB/CU FT)	(BTU/LB)
1	1	538.30	78.000	-2450.32	45	1	538.30	78.000	-2450.32
2	1	538.30	78.000	-2450.32	46	1	538.30	78.000	-2450.32
3	1	538.30	78.000	-2450.32	47	1	538.30	78.000	-2450.32
4	1	538.30	78.000	-2450.32	48	1	538.30	78.000	-2450.32
5	1	538.30	78.000	-2450.32	49	1	538.30	78.000	-2450.32
6	1	538.30	78.000	-2450.32	50	1	538.30	78.000	-2450.32
7	1	538.30	78.000	-2450.32	51	1	538.30	78.000	-2450.32
8	1	538.30	78.000	-2450.32	52	1	538.30	78.000	-2450.32
9	1	538.30	78.000	-2450.32	53	1	538.30	78.000	-2450.32
10	1	538.30	78.000	-2450.32	54	1	538.30	78.000	-2450.32

11	1	538.30	78.000	-2450.32	55	1	538.30	78.000	-2450.32
12	1	538.30	78.000	-2450.32	56	1	538.30	78.000	-2450.32
13	1	538.30	78.000	-2450.32	57	1	538.30	78.000	-2450.32
14	1	538.30	78.000	-2450.32	58	1	538.30	78.000	-2450.32
15	1	538.30	78.000	-2450.32	59	1	538.30	78.000	-2450.32
16	1	538.30	78.000	-2450.32	60	1	538.30	78.000	-2450.32
17	1	538.30	78.000	-2450.32	61	1	538.30	78.000	-2450.32
18	1	538.30	78.000	-2450.32	62	1	538.30	78.000	-2450.32
19	1	538.30	78.000	-2450.32	63	1	538.30	78.000	-2450.32
20	1	538.30	78.000	-2450.32	64	1	538.30	78.000	-2450.32
21	1	538.30	78.000	-2450.32	65	1	538.30	78.000	-2450.32
22	1	538.30	78.000	-2450.32	66	1	538.30	78.000	-2450.32
23	1	538.30	78.000	-2450.32	67	1	538.30	78.000	-2450.32
24	1	538.30	78.000	-2450.32	68	1	538.30	78.000	-2450.32
25	1	538.30	78.000	-2450.32	69	1	538.30	78.000	-2450.32
26	1	538.30	78.000	-2450.32	70	1	538.30	78.000	-2450.32
27	1	538.30	78.000	-2450.32	71	1	538.30	78.000	-2450.32
28	1	538.30	78.000	-2450.32	72	1	538.30	78.000	-2450.32
29	1	538.30	78.000	-2450.32	73	1	538.30	78.000	-2450.32
30	1	538.30	78.000	-2450.32	74	1	538.30	78.000	-2450.32
31	1	538.30	78.000	-2450.32	75	1	538.30	78.000	-2450.32
32	1	538.30	78.000	-2450.32	76	1	538.30	78.000	-2450.32
33	1	538.30	78.000	-2450.32	77	1	538.30	78.000	-2450.32
34	1	538.30	78.000	-2450.32	78	1	538.30	78.000	-2450.32
35	1	538.30	78.000	-2450.32	79	1	538.30	78.000	-2450.32
36	1	538.30	78.000	-2450.32	80	1	538.30	78.000	-2450.32
37	1	538.30	78.000	-2450.32	81	1	538.30	78.000	-2450.32
38	1	538.30	78.000	-2450.32	82	1	538.30	78.000	-2450.32
39	1	538.30	78.000	-2450.32	83	1	538.30	78.000	-2450.32
40	1	538.30	78.000	-2450.32	84	1	538.30	78.000	-2450.32
41	1	538.30	78.000	-2450.32	85	1	538.30	78.000	-2450.32
42	1	538.30	78.000	-2450.32	86	1	538.30	78.000	-2450.32
43	1	538.30	78.000	-2450.32	87	1	538.30	78.000	-2450.32
44	1	538.30	78.000	-2450.32	88	1	538.30	78.000	-2450.32

AEROTHERM CHARRING MATERIAL THERMAL RESPONSE AND' ABLATION PROGRAM \*\* CMA92FLO 1.0  
Check case for expansion model to compare in depth conduction PG. 24

----- 5.0000 SECONDS -----  
TIME SURF PROB SURFACE SURFACE H WALL H EDGE HEAT COEFF CH/CHO  
STEP ITER OPTN TEMP(R) RAD (IN) (BTU/LB) (BTU/LB) (LB/SQ FT-S)  
323 2 3 3237.40 0.0000 0.00 0.00 0.00000 0.00000

---ABLATION RATES---  
B PRIME B PRIME G M DOT CHAR M DOT GAS M CHAR M GAS  
(LB/SQ FT-SEC) (LB/ORIG SQ FT)  
0.0000E+00 0.0000E+00 0.0000E+00 0.4711E-02 0.0000E+00 0.3480E-01

---RECESSIONS/RECESSION RATES---  
(IN) / (IN/SEC)  
SURFACE CHAR (0.15) PYROLYSIS (0.85)  
0.0000000/0.0000000 0.0034496/0.0005193 0.0111342/0.0017937

---SURFACE ENERGY FLUX TERMS---  
CURRENT RATES (BTU/SQ FT SURFACE-SEC)  
AND INTEGRATED VALUES (BTU/ORIG SQ FT)  
CONVECTED RADIATED RADIATED CHEMICAL CONDUCTION  
IN IN OUT GENERATION AWAY  
RATE 0.000E+00 0.594E+02 -0.476E+02 0.000E+00 -0.118E+02  
TOTAL 0.000E+00 0.297E+03 -0.189E+03 0.000E+00 -0.108E+03

---INTERIOR ENERGY TERMS---  
CURRENT RATES (BTU/SQ FT SURFACE-SEC)  
AND INTEGRATED VALUES (BTU/ORIG SQ FT)  
PYROL GAS DECOMP CONVECTION STORAGE LOSS AT  
PICK UP ABSORPTION WITH SOLIDS IN SOLID REAR FACE

RATE 0.296E+01 0.448E+01 0.000E+00 0.448E+01 -0.221E-07  
TOTAL 0.168E+02 0.359E+02 0.000E+00 0.555E+02 -0.113E-06

NODE MAT TEMP DENSITY ENTHALPY				NODE MAT TEMP DENSITY ENTHALPY					
(DEG R) (LB/CU FT) (BTU/LB)				(DEG R) (LB/CU FT) (BTU/LB)					
1	0	3237.40	31.262	-730.60	45	0	550.62	77.932	-2445.53
2	0	2614.12	32.202	-1053.96	46	0	548.06	77.934	-2446.46
3	0	2228.68	33.838	-1279.17	47	0	545.96	77.935	-2447.22
4	0	1873.59	36.780	-1509.70	48	0	544.26	77.936	-2447.84
5	0	1575.03	42.504	-1744.86	49	0	542.90	77.937	-2448.34
6	0	1373.89	52.244	-1952.49	50	0	541.81	77.937	-2448.73
7	0	1258.33	60.576	-2072.04	51	0	540.95	77.938	-2449.04
8	0	1184.95	65.408	-2135.06	52	0	540.28	77.938	-2449.28
9	0	1132.09	67.989	-2172.01	53	0	539.76	77.938	-2449.47
10	0	1090.39	69.390	-2196.54	54	0	539.36	77.938	-2449.62
11	0	1040.05	70.568	-2222.67	55	0	539.06	77.938	-2449.73
12	0	985.51	71.622	-2249.36	56	0	538.83	77.938	-2449.81
13	0	941.49	72.422	-2270.53	57	0	538.66	77.939	-2449.87
14	0	904.79	73.097	-2288.18	58	0	538.53	77.939	-2449.92
15	0	873.60	73.693	-2303.28	59	0	538.44	77.939	-2449.95
16	0	846.71	74.229	-2316.39	60	0	538.37	77.939	-2449.97
17	0	823.27	74.715	-2327.89	61	0	538.32	77.939	-2449.99
18	0	802.66	75.157	-2338.07	62	0	538.29	77.939	-2450.00
19	0	784.34	75.556	-2347.14	63	0	538.26	77.939	-2450.01
20	0	767.85	75.915	-2355.28	64	0	538.25	77.939	-2450.02
21	0	752.69	76.233	-2362.67	65	0	538.24	77.939	-2450.02
22	0	738.53	76.512	-2369.42	66	0	538.23	77.939	-2450.03
23	0	725.27	76.752	-2375.64	67	0	538.22	77.939	-2450.03
24	0	712.80	76.957	-2381.37	68	0	538.22	77.939	-2450.03
25	0	701.04	77.128	-2386.65	69	0	538.21	77.939	-2450.03
26	0	689.95	77.269	-2391.54	70	0	538.21	77.939	-2450.03
27	0	679.47	77.385	-2396.06	71	0	538.21	77.939	-2450.03
28	0	669.59	77.480	-2400.22	72	0	538.21	77.939	-2450.03
29	0	660.35	77.557	-2403.99	73	0	538.21	77.939	-2450.03
30	0	651.74	77.619	-2407.45	74	0	538.21	77.939	-2450.03
31	0	643.71	77.670	-2410.64	75	0	538.21	77.939	-2450.03
32	0	636.21	77.711	-2413.58	76	0	538.21	77.939	-2450.03
33	0	629.32	77.744	-2416.24	77	0	538.21	77.939	-2450.03
34	0	623.10	77.772	-2418.62	78	0	538.21	77.939	-2450.03
35	0	617.45	77.794	-2420.77	79	0	538.21	77.939	-2450.03
36	0	608.55	77.826	-2424.13	80	0	538.21	77.939	-2450.03
37	0	597.70	77.859	-2428.21	81	0	538.21	77.939	-2450.03
38	0	588.36	77.881	-2431.69	82	0	538.21	77.939	-2450.03
39	0	580.19	77.897	-2434.71	83	0	538.21	77.939	-2450.03
40	0	573.10	77.908	-2437.32	84	0	538.21	77.939	-2450.03
41	0	567.01	77.917	-2439.55	85	0	538.21	77.939	-2450.03
42	0	561.83	77.922	-2441.45	86	0	538.21	77.939	-2450.03
43	0	557.43	77.927	-2443.05	87	0	538.21	77.939	-2450.03
44	0	553.72	77.930	-2444.40	88	0	538.21	77.939	-2450.03

AEROTHERM CHARRING MATERIAL THERMAL RESPONSE AND' ABLATION PROGRAM \*\* CMA92FLO 1.0  
Check case for expansion model to compare in depth conduction PG. 34

----- 10.0000 SECONDS -----  
TIME SURF PROB SURFACE SURFACE H WALL H EDGE HEAT COEFF CH/CHO  
STEP ITER OPTN TEMP(R) RAD (IN) (BTU/LB) (BTU/LB) (LB/SQ FT-S)  
633 1 3 3292.93 0.0000 0.00 0.00 0.00000 0.00000

---ABLATION RATES---  
B PRIME B PRIME G M DOT CHAR M DOT GAS M CHAR M GAS  
(LB/SQ FT-SEC) (LB/ORIG SQ FT)  
0.0000E+00 0.0000E+00 0.0000E+00 0.3584E-02 0.0000E+00 0.5506E-01

---RECESSIONS/RECESSION RATES---  
(IN) / (IN/SEC)  
SURFACE CHAR (0.15) PYROLYSIS (0.85)  
0.0000000/0.0000000 0.0058372/0.0004338 0.0182317/0.0012431

---SURFACE ENERGY FLUX TERMS---  
 CURRENT RATES (BTU/SQ FT SURFACE-SEC)  
 AND INTEGRATED VALUES (BTU/ORIG SQ FT)  
 CONVECTED RADIATED RADIATED CHEMICAL CONDUCTION  
 IN IN OUT GENERATION AWAY  
 RATE 0.000E+00 0.594E+02 -0.509E+02 0.000E+00 -0.844E+01  
 TOTAL 0.000E+00 0.594E+03 -0.437E+03 0.000E+00 -0.157E+03

---INTERIOR ENERGY TERMS---  
 CURRENT RATES (BTU/SQ FT SURFACE-SEC)  
 AND INTEGRATED VALUES (BTU/ORIG SQ FT)  
 PYROL GAS DECOMP CONVECTION STORAGE LOSS AT  
 PICK UP ABSORPTION WITH SOLIDS IN SOLID REAR FACE  
 RATE 0.260E+01 0.316E+01 0.000E+00 0.278E+01 -0.212E-07  
 TOTAL 0.306E+02 0.544E+02 0.000E+00 0.728E+02 -0.221E-06

NODE MAT		TEMP	DENSITY	ENTHALPY	NODE MAT		TEMP	DENSITY	ENTHALPY
		(DEG R)	(LB/CU FT)	(BTU/LB)			(DEG R)	(LB/CU FT)	(BTU/LB)
1	0	3292.93	30.480	-677.72	45	0	577.79	77.802	-2435.08
2	0	2846.32	30.831	-901.15	46	0	573.06	77.817	-2436.86
3	0	2563.48	31.350	-1051.26	47	0	568.79	77.829	-2438.46
4	0	2288.37	32.155	-1204.72	48	0	564.95	77.839	-2439.89
5	0	2025.84	33.450	-1361.02	49	0	561.53	77.846	-2441.16
6	0	1786.17	35.618	-1521.83	50	0	558.46	77.853	-2442.30
7	0	1576.43	39.477	-1692.09	51	0	555.72	77.858	-2443.31
8	0	1411.56	46.028	-1863.44	52	0	553.29	77.862	-2444.21
9	0	1298.66	53.507	-1994.08	53	0	551.14	77.865	-2445.00
10	0	1223.44	59.110	-2073.28	54	0	549.25	77.868	-2445.69
11	0	1146.67	64.174	-2140.93	55	0	547.59	77.870	-2446.30
12	0	1073.88	67.602	-2191.58	56	0	546.14	77.872	-2446.83
13	0	1020.28	69.189	-2221.74	57	0	544.89	77.873	-2447.29
14	0	977.56	70.192	-2243.89	58	0	543.81	77.874	-2447.68
15	0	941.89	70.964	-2261.90	59	0	542.88	77.875	-2448.02
16	0	911.32	71.609	-2277.20	60	0	542.08	77.876	-2448.31
17	0	884.68	72.171	-2290.49	61	0	541.41	77.877	-2448.56
18	0	861.17	72.672	-2302.22	62	0	540.84	77.877	-2448.77
19	0	840.26	73.126	-2312.69	63	0	540.36	77.877	-2448.94
20	0	821.50	73.543	-2322.11	64	0	539.95	77.878	-2449.09
21	0	804.58	73.929	-2330.64	65	0	539.61	77.878	-2449.21
22	0	789.23	74.288	-2338.42	66	0	539.33	77.878	-2449.32
23	0	775.24	74.621	-2345.54	67	0	539.10	77.878	-2449.40
24	0	762.43	74.932	-2352.07	68	0	538.91	77.879	-2449.47
25	0	750.60	75.221	-2358.06	69	0	538.76	77.879	-2449.53
26	0	739.63	75.489	-2363.59	70	0	538.63	77.879	-2449.57
27	0	729.48	75.735	-2368.71	71	0	538.52	77.879	-2449.61
28	0	720.00	75.962	-2373.45	72	0	538.44	77.879	-2449.64
29	0	711.09	76.169	-2377.88	73	0	538.37	77.879	-2449.66
30	0	702.64	76.357	-2382.03	74	0	538.29	77.879	-2449.69
31	0	694.61	76.527	-2385.93	75	0	538.23	77.879	-2449.72
32	0	686.94	76.679	-2389.60	76	0	538.18	77.879	-2449.73
33	0	679.60	76.815	-2393.05	77	0	538.16	77.879	-2449.74
34	0	672.58	76.935	-2396.31	78	0	538.14	77.879	-2449.75
35	0	665.90	77.041	-2399.30	79	0	538.13	77.879	-2449.75
36	0	654.91	77.194	-2404.10	80	0	538.13	77.879	-2449.75
37	0	640.97	77.363	-2410.05	81	0	538.13	77.879	-2449.75
38	0	628.85	77.484	-2415.07	82	0	538.12	77.879	-2449.76
39	0	618.55	77.573	-2419.23	83	0	538.12	77.879	-2449.76
40	0	609.72	77.639	-2422.75	84	0	538.12	77.879	-2449.76
41	0	601.98	77.689	-2425.79	85	0	538.12	77.879	-2449.76
42	0	595.07	77.728	-2428.48	86	0	538.12	77.879	-2449.76
43	0	588.77	77.759	-2430.91	87	0	538.12	77.879	-2449.76
44	0	583.02	77.783	-2433.10	88	0	538.12	77.879	-2449.76

AEROTHERM CHARRING MATERIAL THERMAL RESPONSE AND' ABLATION PROGRAM \*\* CMA92FLO 1.0  
 Check case for expansion model to compare in depth conduction PG. 35

----- 20.0000 SECONDS -----  
 TIME SURF PROB SURFACE SURFACE H WALL H EDGE HEAT COEFF CH/CHO



STEP ITER OPTN TEMP(R) RAD (IN) (BTU/LB) (BTU/LB) (LB/SQ FT-S)  
1235 1 3 3331.13 0.0000 0.00 0.00 0.00000 0.00000

---ABLATION RATES---

B PRIME B PRIME G M DOT CHAR M DOT GAS M CHAR M GAS  
(LB/SQ FT-SEC) (LB/ORIG SQ FT)  
0.0000E+00 0.0000E+00 0.0000E+00 0.2698E-02 0.0000E+00 0.8585E-01

---RECESSIONS/RECESSION RATES---

(IN) / (IN/SEC)  
SURFACE CHAR (0.15) PYROLYSIS (0.85)  
0.0000000/0.0000000 0.0092031/0.0002720 0.0290449/0.0009473

---SURFACE ENERGY FLUX TERMS---

CURRENT RATES (BTU/SQ FT SURFACE-SEC)  
AND INTEGRATED VALUES (BTU/ORIG SQ FT)  
CONVECTED RADIATED RADIATED CHEMICAL CONDUCTION  
IN IN OUT GENERATION AWAY  
RATE 0.000E+00 0.594E+02 -0.533E+02 0.000E+00 -0.605E+01  
TOTAL 0.000E+00 0.119E+04 -0.960E+03 0.000E+00 -0.227E+03

---INTERIOR ENERGY TERMS---

CURRENT RATES (BTU/SQ FT SURFACE-SEC)  
AND INTEGRATED VALUES (BTU/ORIG SQ FT)  
PYROL GAS DECOMP CONVECTION STORAGE LOSS AT  
PICK UP ABSORPTION WITH SOLIDS IN SOLID REAR FACE  
RATE 0.222E+01 0.219E+01 0.000E+00 0.174E+01 -0.203E-07  
TOTAL 0.546E+02 0.804E+02 0.000E+00 0.945E+02 -0.426E-06

NODE MAT TEMP DENSITY ENTHALPY NODE MAT TEMP DENSITY ENTHALPY  
(DEG R) (LB/CU FT) (BTU/LB) (DEG R) (LB/CU FT) (BTU/LB)

1	0	3331.13	30.044	-644.20	45	0	609.60	77.291	-2420.99
2	0	3010.23	30.186	-801.47	46	0	604.17	77.360	-2423.30
3	0	2803.98	30.371	-905.45	47	0	599.20	77.418	-2425.39
4	0	2602.05	30.618	-1009.18	48	0	594.58	77.467	-2427.31
5	0	2404.07	30.960	-1113.67	49	0	590.23	77.510	-2429.09
6	0	2211.22	31.444	-1218.66	50	0	586.16	77.545	-2430.74
7	0	2026.00	32.150	-1324.68	51	0	582.33	77.576	-2432.28
8	0	1851.65	33.210	-1432.91	52	0	578.75	77.602	-2433.70
9	0	1691.32	34.869	-1545.47	53	0	575.41	77.624	-2435.02
10	0	1545.99	37.544	-1667.01	54	0	572.28	77.644	-2436.24
11	0	1375.72	44.244	-1852.35	55	0	569.37	77.660	-2437.38
12	0	1228.58	54.431	-2029.21	56	0	566.67	77.674	-2438.42
13	0	1138.95	61.247	-2122.07	57	0	564.16	77.687	-2439.39
14	0	1077.06	64.887	-2172.16	58	0	561.83	77.697	-2440.28
15	0	1029.54	66.749	-2202.64	59	0	559.68	77.706	-2441.10
16	0	990.88	67.912	-2224.68	60	0	557.68	77.714	-2441.86
17	0	958.29	68.786	-2242.43	61	0	555.83	77.721	-2442.57
18	0	930.16	69.506	-2257.47	62	0	554.11	77.727	-2443.21
19	0	905.47	70.125	-2270.54	63	0	552.53	77.732	-2443.81
20	0	883.52	70.671	-2282.09	64	0	551.08	77.736	-2444.35
21	0	863.82	71.158	-2292.41	65	0	549.75	77.740	-2444.85
22	0	845.99	71.598	-2301.71	66	0	548.53	77.744	-2445.31
23	0	829.76	72.000	-2310.17	67	0	547.42	77.747	-2445.73
24	0	814.90	72.370	-2317.91	68	0	546.40	77.749	-2446.10
25	0	801.23	72.713	-2325.04	69	0	545.48	77.751	-2446.45
26	0	788.61	73.033	-2331.62	70	0	544.65	77.753	-2446.76
27	0	776.92	73.333	-2337.73	71	0	543.89	77.755	-2447.04
28	0	766.05	73.615	-2343.43	72	0	543.21	77.756	-2447.29
29	0	755.89	73.881	-2348.73	73	0	542.60	77.757	-2447.51
30	0	746.34	74.133	-2353.68	74	0	541.78	77.759	-2447.82
31	0	737.41	74.369	-2358.32	75	0	540.90	77.760	-2448.14
32	0	729.08	74.592	-2362.66	76	0	540.20	77.761	-2448.40
33	0	721.28	74.803	-2366.72	77	0	539.66	77.762	-2448.60
34	0	713.97	75.001	-2370.53	78	0	539.23	77.763	-2448.76
35	0	707.10	75.188	-2374.11	79	0	538.90	77.763	-2448.88
36	0	695.94	75.487	-2379.90	80	0	538.66	77.764	-2448.97
37	0	681.73	75.864	-2387.23	81	0	538.47	77.764	-2449.04

38	0	669.05	76.182	-2393.64	82	0	538.33	77.764	-2449.09
39	0	657.65	76.448	-2399.19	83	0	538.23	77.764	-2449.12
40	0	647.36	76.667	-2404.09	84	0	538.15	77.764	-2449.15
41	0	638.00	76.846	-2408.44	85	0	538.10	77.764	-2449.17
42	0	629.58	76.992	-2412.25	86	0	538.06	77.764	-2449.18
43	0	622.16	77.111	-2415.54	87	0	538.04	77.764	-2449.19
44	0	615.56	77.209	-2418.42	88	0	538.03	77.764	-2449.20

AEROTHERM CHARRING MATERIAL THERMAL RESPONSE AND' ABLATION PROGRAM \*\* CMA92FLO 1.0  
Check case for expansion model to compare in depth conduction PG. 41

----- 45.0000 SECONDS -----  
TIME SURF PROB SURFACE SURFACE H WALL H EDGE HEAT COEFF CH/CHO  
STEP ITER OPTN TEMP(R) RAD (IN) (BTU/LB) (BTU/LB) (LB/SQ FT-S)  
2740 1 3 3360.41 0.0000 0.00 0.00 0.00000 0.00000

---ABLATION RATES---  
B PRIME B PRIME G M DOT CHAR M DOT GAS M CHAR M GAS  
(LB/SQ FT-SEC) (LB/ORIG SQ FT)  
0.0000E+00 0.0000E+00 0.0000E+00 0.1889E-02 0.0000E+00 0.1412E+00

---RECESSIONS/RECESSION RATES---  
(IN) / (IN/SEC)  
SURFACE CHAR (0.15) PYROLYSIS (0.85)  
0.0000000/0.0000000 0.0148421/0.0001699 0.0486267/0.0006537

---SURFACE ENERGY FLUX TERMS---  
CURRENT RATES (BTU/SQ FT SURFACE-SEC)  
AND INTEGRATED VALUES (BTU/ORIG SQ FT)  
CONVECTED RADIATED RADIATED CHEMICAL CONDUCTION  
IN IN OUT GENERATION AWAY  
RATE 0.000E+00 0.594E+02 -0.552E+02 0.000E+00 -0.414E+01  
TOTAL 0.000E+00 0.267E+04 -0.232E+04 0.000E+00 -0.350E+03

---INTERIOR ENERGY TERMS---  
CURRENT RATES (BTU/SQ FT SURFACE-SEC)  
AND INTEGRATED VALUES (BTU/ORIG SQ FT)  
PYROL GAS DECOMP CONVECTION STORAGE LOSS AT  
PICK UP ABSORPTION WITH SOLIDS IN SOLID REAR FACE  
RATE 0.177E+01 0.137E+01 0.000E+00 0.101E+01 -0.642E-07  
TOTAL 0.104E+03 0.123E+03 0.000E+00 0.127E+03 -0.130E-05

NODE MAT		TEMP	DENSITY	ENTHALPY	NODE MAT		TEMP	DENSITY	ENTHALPY
		(DEG R)	(LB/CU FT)	(BTU/LB)			(DEG R)	(LB/CU FT)	(BTU/LB)
1	0	3360.41	29.754	-619.78	45	0	644.03	75.629	-2399.76
2	0	3140.23	29.808	-726.25	46	0	637.63	75.811	-2403.07
3	0	2996.86	29.872	-796.59	47	0	631.78	75.973	-2406.05
4	0	2855.81	29.948	-866.15	48	0	626.47	76.116	-2408.73
5	0	2716.76	30.042	-935.25	49	0	621.66	76.245	-2411.14
6	0	2579.56	30.157	-1004.16	50	0	617.24	76.360	-2413.34
7	0	2444.19	30.303	-1073.09	51	0	613.14	76.463	-2415.36
8	0	2310.65	30.489	-1142.24	52	0	609.32	76.557	-2417.23
9	0	2180.19	30.729	-1210.46	53	0	605.73	76.642	-2418.97
10	0	2054.03	31.046	-1278.60	54	0	602.36	76.719	-2420.59
11	0	1875.29	31.748	-1381.37	55	0	599.18	76.789	-2422.10
12	0	1656.10	33.442	-1525.14	56	0	596.15	76.852	-2423.52
13	0	1466.23	37.010	-1688.88	57	0	593.25	76.910	-2424.87
14	0	1319.27	43.600	-1864.06	58	0	590.47	76.963	-2426.15
15	0	1218.03	50.884	-1995.97	59	0	587.81	77.011	-2427.36
16	0	1145.94	56.465	-2079.04	60	0	585.26	77.055	-2428.50
17	0	1092.20	60.427	-2133.03	61	0	582.81	77.094	-2429.59
18	0	1049.64	62.872	-2167.85	62	0	580.48	77.130	-2430.62
19	0	1014.24	64.380	-2192.00	63	0	578.24	77.163	-2431.60
20	0	983.85	65.435	-2210.72	64	0	576.10	77.193	-2432.52
21	0	957.18	66.271	-2226.39	65	0	574.05	77.220	-2433.40
22	0	933.47	66.985	-2240.04	66	0	572.10	77.245	-2434.24
23	0	912.20	67.619	-2252.17	67	0	570.23	77.268	-2435.03
24	0	892.99	68.190	-2263.07	68	0	568.45	77.288	-2435.77

25	0	875.56	68.711	-2272.93	69	0	566.75	77.307	-2436.48
26	0	859.63	69.187	-2281.91	70	0	565.13	77.324	-2437.16
27	0	845.01	69.625	-2290.13	71	0	563.58	77.340	-2437.79
28	0	831.52	70.029	-2297.69	72	0	562.11	77.354	-2438.40
29	0	819.01	70.402	-2304.67	73	0	560.72	77.367	-2438.97
30	0	807.37	70.749	-2311.15	74	0	558.72	77.385	-2439.78
31	0	796.51	71.073	-2317.18	75	0	556.30	77.405	-2440.75
32	0	786.33	71.375	-2322.81	76	0	554.11	77.421	-2441.62
33	0	776.77	71.658	-2328.09	77	0	552.15	77.435	-2442.40
34	0	767.76	71.925	-2333.05	78	0	550.40	77.446	-2443.09
35	0	759.26	72.176	-2337.72	79	0	548.85	77.456	-2443.70
36	0	745.37	72.580	-2345.23	80	0	547.49	77.464	-2444.23
37	0	727.88	73.098	-2354.71	81	0	546.31	77.470	-2444.68
38	0	712.65	73.555	-2362.98	82	0	545.30	77.475	-2445.07
39	0	699.26	73.962	-2370.26	83	0	544.46	77.479	-2445.40
40	0	687.38	74.325	-2376.71	84	0	543.77	77.483	-2445.67
41	0	676.76	74.649	-2382.47	85	0	543.22	77.485	-2445.87
42	0	667.23	74.938	-2387.57	86	0	542.82	77.487	-2446.03
43	0	658.69	75.195	-2392.08	87	0	542.55	77.488	-2446.13
44	0	651.01	75.425	-2396.12	88	0	542.42	77.489	-2446.18

# AEROTHERM CHARRING MATERIAL THERMAL RESPONSE AND' ABLATION PROGRAM \*\* CMA92FLO 1.0

Check case for expansion model to compare in depth conduction PG. 42

OPTIONAL OUTPUT OF THERMOCOUPLE TEMPERATURES AND/OR ISOTHERM DEPTHS

DEPTHS MEASURED FROM ORIGINAL SURFACE

TEMPERATURES IN DEGREES RANKINE

EACH OUTPUT BLOCK SHOWS THE TIME IN SECONDS, THE CURRENT SURFACE TEMPERATURE, THE TEMPERATURES OF 3 THERMOCOUPLES, AND THE DEPTHS IN INCHES OF 0 ISOTHERMS WITHIN THE MAIN ABLATING MATERIAL.

THE FIRST BLOCK SHOWS A SAMPLE TIME AND SURFACE TEMPERATURE, THE SPECIFIED DEPTHS OF THE THERMOCOUPLES (IF ANY) AND THE ISOTHERM TEMPERATURES. THE ARRANGEMENT OF THIS BLOCK CORRESPONDS TO THE ARRANGEMENT OF THE OUTPUT DATA.

45.0000 3360.4108 0.0500 0.1500 0.2500

## OUTPUT DATA

0.0000	538.3000	538.3000	538.3000	538.3000
0.5000	2580.8093	539.1847	538.2908	538.2908
1.0000	2943.0094	549.3729	538.2817	538.2817
1.5000	3063.2385	565.7198	538.2727	538.2726
2.0000	3115.4463	581.9962	538.2664	538.2635
2.5000	3152.9661	596.2869	538.2746	538.2544
3.0000	3180.0293	608.5971	538.3238	538.2454
3.5000	3198.4174	619.6508	538.4487	538.2364
4.0000	3213.9320	629.7921	538.6814	538.2275
4.5000	3226.9884	639.1847	539.0442	538.2187
5.0000	3237.3976	647.6598	539.5473	538.2103
5.5000	3246.5521	655.2149	540.1902	538.2026
6.0000	3254.6201	662.0210	540.9651	538.1964
6.5000	3261.1377	668.1682	541.8588	538.1926
7.0000	3267.0792	673.7608	542.8562	538.1923
7.5000	3272.3316	678.8650	543.9410	538.1969
8.0000	3277.5159	683.5161	545.0974	538.2079
8.5000	3282.0566	687.7499	546.3104	538.2268
9.0000	3286.2178	691.6457	547.5666	538.2550
9.5000	3289.5838	695.2495	548.8540	538.2939
10.0000	3292.9285	698.5806	550.1623	538.3448
15.0000	3317.0415	723.4384	562.9774	539.6508
20.0000	3331.1253	741.8004	573.8175	542.3105
25.0000	3340.7049	757.0299	582.5320	545.7616
30.0000	3347.0318	770.1160	589.5343	549.4897
35.0000	3352.5673	781.7155	595.2475	553.1923
40.0000	3356.8880	792.2528	599.9872	556.7250
45.0000	3360.4108	801.8478	604.0173	560.0344

**APPENDIX D**  
**EXAMPLE SWELL MODEL OUTPUT DECK**

TIME	NODE	DEL (I)	DEL SWL(I)	RATIO SWELL	SUM DEL	SUM DSW	SUM RATIO	NODE TEMP	NODE DENSITY	PHI
15.0	1	.0005	.00098	1.96	0.0005	0.00098	1.96	1353	32.36	0.9362
15.0	2	.001	.0029	2.95	0.0015	0.0039	2.62	1321	32.62	0.9309
15.0	3	.001	.0036	3.62	0.0025	0.0075	3.02	1278	33.11	0.9208
15.0	4	.001	.0041	4.08	0.0035	0.0116	3.32	1226	33.83	0.9060
15.0	5	.001	.0042	4.24	0.0045	0.0158	3.52	1167	34.86	0.8849
15.0	6	.001	.0042	4.29	0.0055	0.0201	3.66	1102	36.33	0.8548
15.0	7	.001	.0043	4.33	0.0065	0.0245	3.77	1035	38.43	0.8117
15.0	8	.001	.0044	4.40	0.0075	0.0289	3.85	966	41.49	0.7489
15.0	9	.001	.0044	4.47	0.0085	0.0333	3.92	898	45.79	0.6607
15.0	10	.001	.0042	4.25	0.0095	0.0376	3.96	833	50.87	0.5565

TIME	:	Time (sec)
NODE	:	Node number in finite difference mesh
DEL(I)	:	Nonintumesced node thickness (inch)
DEL SWL(I)	:	Intumesced node thickness (inch)
RATIO SWELL	:	Ratio of DELSWL(I)/DEL(I)
SUM DEL	:	Summed thickness for nonintumesced nodes (inch)
SUM DSW	:	Summed thickness for intumesced nodes (inch)
SUM RATIO	:	Ratio of SUM DSW/SUM DEL
NODE TEMP	:	Node Temperature (°F)
NODE DENSITY	:	Node density (lbm/ft <sup>3</sup> )
PHI	:	Char state

## INITIAL DISTRIBUTION LIST

	<u>Copies</u>
Weapon Systems Technology Information Analysis Center ATTN: Ms. Vakare Valaitis 1901 N. Beauregard Street, Suite 400 Alexandria, VA 22311-1720	1
Defense Technical Information Center 8725 John J. Kingman Rd., Suite 0944 Ft. Belvoir, VA 22060-6218	1
Mr. Donald M. Curry M/S ES32 NASA Johnson Space Center 2101 NASA Road 1 Houston, Texas 77058-3696	1
Mr. Forrest Strobel	1
Dr. Al Murray	1
ITT Industries 6767 Old Madison Pike, Ste. 310 Huntsville, AL 35806	
AMSRD-AMR, (Electronically)	
AMSRD-AMR-AS-I-RSIC	2
AMSRD-AMR-PS-PI, Dr. Gerald Russell	1
AMSRD-L-G-I, Mr. Dayn Beam	1